Novel adherend laminate designs for composite bonded joints

Kupski, J.A.

DOI
10.4233/uuid:67b8a7e6-2a10-49c1-8ec6-c922259ef5d9

Publication date
2020

Document Version
Final published version

Citation (APA)
Kupski, J. A. (2020). *Novel adherend laminate designs for composite bonded joints*. [Dissertation (TU Delft), Delft University of Technology]. https://doi.org/10.4233/uuid:67b8a7e6-2a10-49c1-8ec6-c922259ef5d9

NOVEL ADHEREND LAMINATE DESIGNS FOR COMPOSITE BONDED JOINTS

DISSERTATION

for the purpose of obtaining the degree of doctor
at Delft University of Technology,
oby the authority of the Rector Magnificus Prof. dr. ir. T.H.J.J. van der Hagen,
chair of the Board of Doctorates,
to be defended publicly on 13 November 2020

by

JULIAN ALEXANDER KUPSKI

Master of Science in Mechanical Engineering
RWTH Aachen University
born in Werther, Germany

This dissertation has been approved by the promotors.

Composition of the doctoral committee:

Rector Magnificus	Technische Universiteit Delft, chairman
Prof. dr. ir. R. Benedictus	Technische Universiteit Delft, promotor
Dr. S. Teixeira de Freitas	Technische Universiteit Delft, co-promotor

Independent members:

Prof. dr. ir. C. Kassapoglou	Delft University of Technology
Prof. dr. R. Adams	University of Bristol
Prof. dr. N. Carrere	École Nationale Supérieure de Techniques Avancées Bretagne
Dr. G. Catalanotti	Queen's University Belfast
Prof. dr. A. Herrmann	Faserinstitut Bremen e.V.

Significant work on the model design as well as on the preparation of this dissertation has been contributed by the group of Prof. dr. P. Camanho, from Departamento de Engenharia Mecânica of Faculdade de Engenharia da Universidade do Porto

Keywords: CFRP, Composite bonded joints, Layup variation, Thin plies, Finger joints

Printed by: Ipskamp Printing (www.ipskampprinting.nl)
Front and back: Beautiful cover art that captures the entire content of this thesis in a single illustration.

This work has been funded by the Netherlands Organisation for Scientific Research (NWO), project number 14366.
ISBN 000-00-0000-000-0

An electronic version of this dissertation is available at
http://repository.tudelft.nl/.

SUMMARY

Adhesive bonding is one of the most suitable joining technologies in terms of weight and mechanical performance for current carbon fiber reinforced polymer aircraft fuselage structures. However, traditional joint topologies such as single overlap joints induce high peel stresses, resulting in sudden failure and low joint strength when compared to metal adherends. This drawback in using carbon fiber reinforced polymer is hindering their performance and efficiency in full-scale structures where joints are essential.

In this thesis, novel design concepts are proposed to tackle the challenge of poor out-of-plane properties of composite adherends that limit the performance of composite single lap bonded joints, by making use of the three design parameters: stacking sequence, ply thickness and overlap stacking.

Design parameters of carbon fiber reinforced polymer bonded joints can be classified in three categories: Global topology relates to the global geometry of the joint, for example whether it is a single or a double overlap joint topology. Local topology refers to features that affect only a local region of the entire bond line, for example a certain spew fillet geometry or a tapered edge of the adherend. The third category describes any design parameters which are related to the specific materials of the adhesive and the adherends. The adherends themselves consist of laminated plies, which can be tailored, for example in terms of ply thickness or stacking sequence. These laminate specific design parameters are the core of this work.

For all adherend laminate designs studied in the context of this thesis, the following approach is chosen: Single lap bonded joints were manufactured varying the design features (stacking sequence, ply thickness and/or overlap stacking). The experimental campaign consisted of quasi-static tensile tests using Acoustic Emission and Digital Image Correlation to monitor the damage and strain evolution of the overlap area during testing. 3D *post-mortem* failure analysis of the fracture surfaces was conducted using a 3D profiling microscope. Parallel to the experiments, a Finite Element Analysis is performed up to damage initiation, taking into account non-linear geometry and elasto-plastic behaviour of the adhesive. Damage initiation loads and strain fields are numerically predicted and validated with experimental data.

Stacking sequence: Single overlap bonded joints with four different composite adherend stacking sequences are tested and numerically simulated, in order to evaluate the effect of the layups on the quasi-static tensile failure of the bonded joints. The results show that increasing the adherend bending stiffness postpones the damage initiation in the joint. However, this is no longer valid for final failure. The ultimate load is influenced by how the damage progresses from crack initiation up to final failure. For similar bending stiffness, a layup that leads to the crack propagating from the adhesive towards the inside layers of the composite increases the ultimate load. The failure mode is highly influenced by the orientation of the interface lamina in contact with the adhesive, such that, a 0° interface ply causes failure within the bond line, while a 90° interface ply causes failure inside the composite adherend.

Ply thickness: Another way to improve the out-of-plain properties of the laminate is to decrease their ply thickness. Single lap bonded joints with three different ply thicknesses of 200μm,

100μm and 50μm are tested. Experimental results show an increase of 16% in the lap shear strength and an increase of 21% in the strain energy when using the 50μm instead of 200μm ply thicknesses. Acoustic Emission measurements show that the damage initiation is postponed up to a 47% higher load when using 50μm instead of 200μm ply thicknesses. Moreover, the total amount of acoustic energy released from initiation up to final failure is significantly less with thin plies. A failure analysis of the numerical results up to damage initiation indicates that with decreasing ply thickness, the damage onset inside the composite is postponed to higher loads and moves away from the adhesive interface towards the mid-thickness of the adherend.

Overlap stacking: In a third approach a change of global joint topology is achieved with multiple stacked overlaps, also referred as finger joints, by using the *ply interleaving technique*. The quasi-static tensile behavior of single lap joints with two overlap lengths 12.7mm and 25.4mm are compared to finger joints with 1 and 2 stacked overlaps through the thickness with a constant 12.7mm overlap length. Two composite adherend stacking sequences, $[(0/90)_s]_4$ and $[(90/0)_s]_4$, are tested for each topology. A difference in peak shear and peel stress at the tip of the bonded region can be observed: (i) the peak peel stress in the 1-finger joint is higher than in the single lap joint configurations because the beneficial effect of avoiding eccentricity in the finger joint is outperformed by the detrimental effect of reducing to half the adherend stiffness at the overlap; (ii) for 2 fingers, the stress field changes significantly with a doubled bonding area and leads to a 23% decrease in peak shear and 33% in peak peel stress, compared to the single lap joint topologies.

It is concluded that a quasi-isotropic layup may not be the best choice in terms of tensile joint strength. In order to improve tensile strength up to damage initiation, the layup should be optimized for bending stiffness, while up to final failure, a stacking sequence that yields to a complex crack path inside the composite can lead to higher ultimate loads. Decreasing the single ply thickness of laminated composite adherends in a single overlap bonded joint increases the maximum load and delays damage initiation of the joint. However, the damage progression till final failure is more sudden. Comparing single overlap with finger joint topologies, different trends at damage initiation and at maximum load are believed to result from how the damage propagates inside the joint. A topology with 2 fingers and layup $[(90/0)_s]_4$, which fails entirely inside the adherend, provides the lowest peak shear and peel stress and the highest load at damage initiation. It is however outperformed in maximum load by a single lap joint topology with layup $[(0/90)_s]_4$, with mostly cohesive failure. It is found that, unlike in single overlap topologies, the most dominant stress component for damage initiation inside the finger joints is the in-plane tensile stress, at the butt joint resin pockets, rather than peel stresses at the overlap region. If weight efficiency is the main requirement, a finger joint design can effectively replace a single overlap joint design. However, for absolute maximum joint strength, the single overlap joint is a better choice than the finger joint. In total, all three approaches lead to an increase in joint strength, either till damage initiation (**Chapter 3, 4, 5**) or till final failure (**Chapter 3**).

SAMENVATTING

Lijmen is een van de meest geschikte verbindingstechnologieën wat betreft gewicht en mechanische prestaties voor koolstofvezel versterkte polymere rompstructuren van vliegtuigen. Traditionele topologieën van verbindingen, zoals enkelvoudige overlappende verbindingen, veroorzaken echter hoge afpelspanningen in het composiet, wat kan lijden tot het plotseling falen van de verbinding en een lagere verbindingssterkte in vergelijking met metaal verbindingen. Deze nadelen in het gebruik van met koolstofvezel versterkt polymeren belemmert hun prestaties en efficiëntie in grotere structuren waar verbindingen essentieel zijn. In dit proefschrift worden nieuwe ontwerpconcepten voorgesteld om de slechte uit-het-vlak eigenschappen van composietverbindingen aan te pakken die de prestaties van enkelvoudige overlappende verbindingen beperken door gebruik te maken van drie ontwerpparameters: stapelvolgorde, laagdikte en overlappende stapels.

Ontwerpparameters van koolstofvezel versterkte polymeren kunnen in drie categorieën worden ingedeeld: Globale topologie heeft betrekking op de globale geometrie van de voeg, bijvoorbeeld of het een enkele of dubbele overlappende voegtopologie is. Lokale topologie verwijst naar kenmerken die alleen een lokaal gebied van de gehele verbindingslijn beïnvloeden, bijvoorbeeld een bepaalde lijm overloop overgangsgeometrie of een taps toelopende rand van de verlijmde onderdelen. De derde categorie beschrijft alle ontwerpparameters die verband houden met de specifieke eigenschappen van de lijm en de te verbinden materialen. De materialen zelf bestaan uit gelamineerde lagen die kunnen worden aangepast, bijvoorbeeld door aanpassing van de laagdikte of de stapelvolgorde. Deze laminaatspecifieke ontwerpparameters vormen de kern van dit werk. Voor alle laminaatontwerpen van de te verbinden proefstukken die in het kader van dit proefschrift zijn bestudeerd, wordt de volgende benadering gekozen: Een eindige elementenanalyse wordt uitgevoerd tot aan de schade-initiatie, terwijl er rekening wordt gehouden met de niet-lineaire geometrie en elasto-plastische eigenschappen van de lijm. Quasi-statische trektesten worden uitgevoerd voor experimentele validatie. Akoestische emissie en digitale beeldcorrelatie werden daarbij gebruikt om de schade en spanningsevolutie van het overlappingsgebied te volgen tijdens het testen. Na het falen van de verbinding werd een 3D *post-mortem* analyse van de breukoppervlakken uitgevoerd met behulp van een 3D microscoop voor oppervlakte analyse.

Stapelvolgorde: Enkelvoudige overlappende verbindingen met vier verschillende stapelvolgorden voor de te verbinden materialen zijn getest en numeriek gesimuleerd om het effect van de stapelvolgorde op de quasi-statische treksterkte van de lijmverbindingen te onderzoeken. De resultaten laten zien dat het verhogen van de buigstijfheid van het materiaal de schade-inititatie uitstelt. Dit heeft echter niet dezelfde invloed op het uiteindelijke falen van de verbinding. De uiteindelijke sterkte wordt beïnvloed door hoe de schade zich ontwikkelt van scheurinitiatie tot het uiteindelijke falen van de verbinding. Voor vergelijkbare buigstijfheden kan de uiteindelijke sterkte worden verhoogd door gebruik te maken van een stapelvolgorde die ervoor zorgt dat een scheur zich voortplant van de lijmlaag naar de binnenlagen van het composiet. De manier van falen wordt sterk beïnvloed door de vezeloriëntatie van de binnenste

laminaatlaag die in contact staat met de lijm. Dit leidt ertoe dat een 0° laag resulteert in het falen van de lijmverbinding, terwijl een 90° laag leidt tot het falen van het verbonden materiaal.
Laagdikte: Een andere manier om de uit-het-vlak eigenschappen van het laminaat te verbeteren, is door de laagdikte te verminderen. Verbindingen met een enkele overlap met drie verschillende laagdiktes van 200µm, 100µm en 50µm zijn getest. Experimentele resultaten tonen een toename van 16% in de scheursterkte en een toename van 21% in de vervormingsenergie bij gebruik van de 50µm in plaats van de 200µm laagdiktes. Uit metingen van de akoestische emissie blijkt echter dat de schade-initiatie wordt uitgesteld tot een 47% hogere belasting bij gebruik van de 50µm in plaats van de 200µm laagdiktes. Bovendien is de totale hoeveelheid akoestische energie die vrijkomt van het moment van schade-initiatie tot het uiteindelijke falen aanzienlijk minder bij het gebruik van dunnere lagen. Een schade-analyse van de numerieke resultaten tot het moment van de schade-initiatie laat zien dat met een afnemende laagdikte, het begin van de schade in het composiet wordt uitgesteld tot hogere belastingen en dat de locatie van de schade zich verplaatst van de lijmverbinding naar het midden van het verbonden materiaal.
Overlap stapeling: In een derde benadering wordt een verandering van de globale verbindingstopologie bereikt door gebruik te maken van meerdere gestapelde overlappingen, ook wel 'vinger'-verbindingen genoemd, met behulp van de *ply interleaving technique*. Het quasi-statische trekgedrag van enkelvoudige overlappende verbindingen van twee overlappende lengtes van 12.7mm en 25.4mm wordt vergeleken met vingerverbindingen van 1 en 2 gestapelde overlappingen door de dikte met een gelijke overlappingslengte van 12.7mm. Twee stapelvolgordes, $[(0/90)_s]_4$ en $[(90/0)_s]_4$, worden getest voor elke topologie. Een verschil in de piekafschuif- en piekafpelspanning aan het uiteinde van het gebonden gebied kan worden waargenomen: (i) de piekafpelspanning in de 1-vingerverbinding is hoger dan in de configuraties met enkelvoudige overlappende verbindingen omdat het gunstige effect van het vermijden van excentriciteit in de vingerverbinding teniet wordt gedaan door het schadelijke effect van het halveren van de materiaalstijfheid ter hoogte van de overlapping; (ii) voor 2-vingerverbindingen verandert het spanningsveld aanzienlijk door een verdubbeld verbindingsgebied en leidt het tot een afname van 23% in de piekafschuiving en 33% in de piekafpelspanning vergeleken met de topologieën van enkelvoudige overlappende verbindingen.
Het wordt geconcludeerd dat een quasi-isotrope stapelvolgorde mogelijk niet de beste keuze is wat betreft de treksterkte van de verbindingen. Om de treksterkte tot aan de initiatie van de schade te verbeteren, moet de stapelvolgorde worden geoptimaliseerd voor buigstijfheid, terwijl voor een hogere uiteindelijke belasting een stapelvolgorde moet worden gebruiken die leidt tot een complex scheurgroeipad in het composiet. Het verminderen van de laagdikte van gelamineerde composiete materialen in een enkele overlappende gelijmde verbinding verhoogt de maximale belasting en vertraagt het initiëren van de schade in de verbinding, maar de schade-ontwikkeling tot het uiteindelijke falen meer onverwacht. Wanneer een enkele overlapping wordt vergeleken met de topologieën van vingerverbindingen, wordt aangenomen dat verschillende trends bij het initiëren van schade en bij de maximale belasting het gevolg zijn van hoe de schade zich in de verbinding ontwikkelt. Een topologie met 2 vingers en een stapelvolgorde van $[(90/0)_s]_4$ die volledig binnen het verbonden materiaal faalt, biedt de laagste

piekschuif- en piekafpelspanning en de hoogste belasting voor de initiatie van schade. Het wordt echter overtroffen voor de maximale belasting door een topologie met een enkele overlapping met stapelvolgorde $[(0/90)_s]_4$, welke vooral faalt in de cohesie. Het is gebleken dat, in tegenstelling tot topologieën met enkele overlap, de meest dominante spanningscomponent voor het ontstaan van schade binnen de vingerverbindingen de trekkracht in het vlak bij de stompe gewrichtsharszakken is, in plaats van spanningen op het overlappingsgebied af te pellen. Als gewichtsefficiëntie de belangrijkste vereiste is, kan een vingerlasontwerp effectief een enkel overlappend voegontwerp vervangen. Voor absolute maximale gewrichtskracht is het enkelvoudig overlappingsverbinding echter een betere keuze dan het vingerverbinding.
In totaal leiden alle drie de benaderingen tot een toename van de verbindingssterkte, hetzij tot aan de schade-initiatie (**Hoofdstuk 3, 4, 5**) of tot aan het uiteindelijke falen (**Hoofdstuk 3**).

NOMENCLATURE

ACRONYMS

2D	Two dimensional
3D	Three dimensional
AE	Acoustic emission
AFP	Automated fiber placement
ASTM	American Society for Testing and Materials
CAI	Compression after impact test
CFRP	Carbon fiber reinforced polymer
CLT	Classical laminate theory
CZM	Cohesive zone model
CT	Computer tomography [scan]
DCB	Double cantilever beam test
DIC	Digital image correlation
DLJ	Double lap joint
DoF	Degrees of Freedom
DSC	Differential Scanning Calorimetry
FEA	Finite element analysis
FEM	Finite element model
FJ	Finger joint
GFRP	Glass fiber reinforced polymer
ILSS	Interlaminar shear strength
LSS	Average lap shear strength
NHC	No hole compression test
OHC	Open hole compression test
OL	Overlap length
PDA	Progressive damage analysis
PPS	Polyphenylenesulfide [fibers]
Prepreg	Pre-impregnated Fibers
PTFE	Polytetrafluoroethylene
PVDF	Physical vapour deposition film
QI	Quasi-isotropic
QIQH	Quasi-isotropic and quasi-homogeneous [laminate]
SEM	Scanning electron microscope
SLJ	Single lap joint
SLS	Single lap shear test
TDS	Technical data sheet
TG	Tongue & groove joint
UD	Unidirectional
UV	Ultraviolet

WWFE	World-wide failure exercise	
XFEM	Extended finite element method	
XWB	Extra wide body	

GREEK SYMBOLS

ν_a	Adhesive Poisson ratio	[-]
ν_{xy}	In-plane Poisson ratio	[-]
ν_{xz}	Transverse Poisson ratio	[-]
ν_{yz}		
σ_{init}	Average shear stress at damage initiation	[MPa]
σ_{LSS}	Average lap shear strength	[MPa]
σ_{yy}	Peel stress	[MPa]
$\sigma_{yy,max}$	Peak peel stress	[MPa]
τ_{xy}	Shear stress	[MPa]
$\tau_{xy,max}$	Peak shear stress	[MPa]

LATIN SYMBOLS

A_f^{coh}	Cohesive final fracture surface	[mm^2]
A_f^{comp}	Composite final fracture surface	[mm^2]
A_f^{total}	Total final fracture surface	[mm^2]
A_{OL}	Initial overlap area	[mm^2]
BLL	Bond line length	[mm]
D	Damage resistance	[-]
D_{11}^*	First row/first column entry of inverse of the bending stiffness matrix	
E_a	Adhesive Young's modulus	[MPa]
$E_a(x)$	Acoustic emission energy	[J]
E^{AE}_i	Acoustic emission energy per hit	[10^{-12} J]
$E_s(x)$	Strain energy	[J]
E_x^f	Flexural engineering constant	[MPa]
E_{xxT}	In-plane longitudinal tensile modulus	[MPa]
E_{yyT} =	In-plane transverse tensile modulus	[MPa]
E_{zzT}	Out-of-plane tensile modulus	[MPa]
F_{init}	Load at damage initiation	[kN]
F_{max}	Maximum load	[kN]
G_{Ic}	Fracture toughness, mode I	[N/mm]
G_{xy}	In-plane shear modulus	[MPa]
G_{xz}	Transverse shear modulus	[MPa]
G_{yz}		
OL	Overlap length	[mm]
OT	Overlap thickness	[mm]

P_{max}	Maximum load	[kN]
S_L	In-plane shear strength	[MPa]
S_T	Transverse shear strength	[MPa]
W	Strain energy	[10^6 J]
t_{ad}	Adhesive thickness	[μm]
t_{UD}	Ply thickness per UD-layer	[mm]
W	Specimen width	[mm]
X_a	Adhesive tensile strength	[MPa]
X_C	In-plane longitudinal compressive strength	[MPa]
X_T	In-plane longitudinal tensile strength	[MPa]
Y_T	In-plane transverse tensile strength	[MPa]
Y_{BT}	Transverse biaxial tensile strength	[MPa]
Y_C	In-plane transverse compressive strength	[MPa]

SUBSCRIPTS

AE	Acoustic emission results
BLL	Bond line length
EXP	Experimental results
NUM	Numerical results
LSS	(Average) lap shear strength
OL	Overlap length
BLT	Bond line thickness

LIST OF FIGURES

LIST OF TABLES

1 INTRODUCTION

1.1 PROBLEM STATEMENT

With the increasing pressure to meet unprecedented levels of eco-efficiency, the aircraft industry constantly aims for lightweight structures. Towards this aim, polymer composites are replacing the conventional Aluminium as the number one material used in aircraft. With the launch of the *BOEING 787 Dreamliner* in October 2011 and the *AIRBUS A350-XWB* in January 2015, airplane fuselage structures made out of Carbon Fibre Reinforced Plastic (CFRP) were consequently introduced in civil aviation.

However, the joining design of those fuselage structures is not following this transition. Currently, composites are being joined using bolts and rivets, a joint design mainly developed for metals. This may lead to an increase in structural weight, since the areas where holes cut through the fibres and disturb the load path have thicker laminates. The mismatch between the use of new materials and traditional "metal-joining" techniques, results in inefficient composite structures and gives ample room for improvement. A suitable joining method is therefore the missing puzzle piece to efficiently use composites in full-scale aircraft structures. One of the most promising joining methods in terms of weight and performance is thereby adhesive bonding [1-1]. A well-designed bonded joint has the potential to be as strong in terms of tensile loading as the base laminate itself.

Yet the lack of acceptance of adhesive bonding by the aviation authorities is currently limiting its application in primary aircraft structures. So far, fasteners are always included along with the bonded systems (so called *chicken-rivets*), as back-up in case the bond fails. There are two main reasons for this lack of acceptance: On the one hand interface failures due to weak bonds are currently impossible to be detected by non-destructive testing [1-2]. On the other hand, the CFRP often comes with low elastic modulus and strength in the in-plane transverse and out-of-plane direction [1-2 - 1-4]. In a joint topology that induces high peel stresses in the thickness direction, using CFRP adherends may result in lower ultimate joint strength than using metal adherends, since the inter- and intra-laminar strength of composites is often lower than a cohesive peel strength of an adhesive [1-4, 1-5].

Nonetheless, by changing the laminate design, composite properties can be tailored to the external loading and research in this field of composites shows that certain stacking sequences can retard delamination [1-6 - 1-8]. Therefore, making use of the anisotropy of the composite material could potentially counteract their poor out-of-plane strength, which can have a positive impact on the performance of composite adhesively bonded joints subjected to peel stresses. Nevertheless, CFRP layups that are used in state-of-the-art aerospace structures are still designed as quasi-isotropic [1-9]. This choice is mainly tied to the easiness of manufacturing and to composite design rules used by the industry (e.g. *10 %-rule*) [1-10], while it may not be the optimum design for a laminated adherend in the vicinity of a multi-axial load hot spot, like in a bonded joint. Furthermore, the geometry of such joint plays an important role for the

predominant stress state. A Single Overlap Joint (SLJ) design is still being used as the most common topology for primary aircraft structures, aiming for low manufacturing complexity and costs.
The latest developments in manufacturing techniques allow for a wider choice of CFRP-layups. As an example, the fuselage of the *A350 XWB* is being built by Automated Fibre Placement (AFP) techniques. Furthermore, recent studies have demonstrated how a reduction of ply thickness in composite laminates enables great freedom with respect to layup design and leads to a delay in damage onset as well as enhanced ultimate load [1-11 - 1-13]. Those two developments mark a significant step in terms of manufacturing quality, allowing for more complex stacking sequences and joint topologies. Suddenly, a simple but structural wise inefficient SLJ-design with quasi-isotropic layup can be replaced by a more advanced joint topology, such as a stepped, scarfed or slotted joint, with a non-conventional layer orientation. Tailoring laminate related design parameters therefore plays a key role in the reduction of detrimental peel stress concentrations in load carrying joints and contributes to the goal of further promoting adhesive bonding for primary aircraft structures.

1.2 RESEARCH OBJECTIVES

The aim of this thesis is to explore novel design concepts for adhesively bonded CFRP-joints, which shall be applied in heavy-loaded primary aircraft fuselage structures. The suggested concepts mainly address improvements in static damage onset and ultimate load of the joint. This is attained by a new design approach that benefits from the layup characteristics of composite materials. The research comprises the investigation of three laminate specific design parameters:

- Stacking sequence
- Single ply thickness
- Overlap stacking

These three parameters have been individually studied for composite materials in general, but have not been combined nor applied to the scope of adhesively bonded CFRP-joints. **Figure 1-1** shows a schematic of the SLJ-design, which is the most common design for bonded joints and therefore a sound reference for this study.

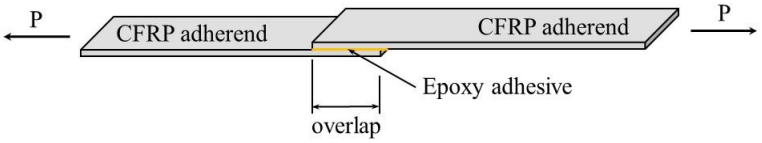

Figure 1-1: Schematic illustration of a SLJ under tensile loading

1.3 THESIS OUTLINE

Figure 1-2 shows the structure of this thesis, based on the different chapters. **Chapter 2** covers the literature review on various design parameters, which have been studied in the context of adhesively bonded CFRP-joints, in order to enhance the damage onset, damage progression and final failure under quasi-static tensile loading. In **Chapter 3,** the first laminate design parameter, fiber direction, is investigated. It is discussed how fiber direction of the outermost layer, as well as stacking sequence and bending stiffness of the adherend affect the failure mechanism of CFRP-SLJs. **Chapter 4** presents the influence of the unidirectional (UD) ply thickness on the failure mechanism of the latter. **Chapter 5** introduces the concept of stacking multiple overlaps through the thickness of one adherend and addresses the question of how a change in global overlap topology increases maximum load as well as the average lap shear strength in comparison with the common SLJ-design. Finally, in **Chapter 6**, a conclusion and outlook are given. In addition, limitations which have been experienced throughout this research are discussed.

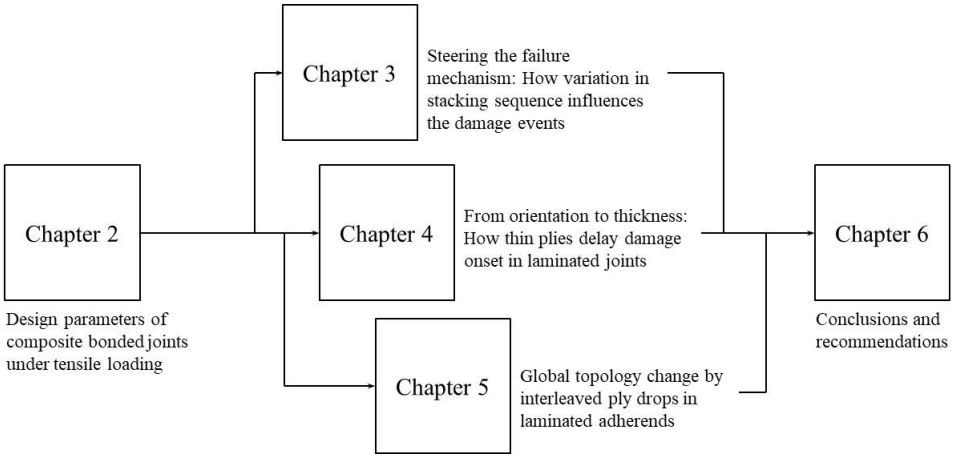

Figure 1-2: Structure of this thesis

REFERENCES

[1-1] T. Loebel, D. Holzhueter, M. Sinapius, C. Huehne: *A hybrid bondline concept for bonded composite joints*. German Aerospace Center (DLR), 2016

[1-2] E. Godwin and F. Matthews: *Review of the Strength of Joints in Fibre-Reinforced Plastics: Part 2 Adhesively bonded joints*. Composites, vol. 13, pp. 29-37, 1982

[1-3] R. Adams: *Strength Predictions for Lap Joints, Especially with Composite Adherends. A Review*. J. Adhesion vol. 30, no. 1-4, pp. 219-242, 1989

[1-4] S. Teixeira de Freitas, J. Sinke: *Adhesion properties of bonded composite-to-Aluminium joints using peel tests*. The Journal of Adhesion, vol. 90, pp. 511-525, 2014

[1-5] S. Teixeira de Freitas, J. Sinke: *Failure analysis of adhesively-bonded skin-to-stiffener joints: Metal–metal vs. composite–metal*. Engineering Failure Analysis, vol. 56, pp. 2–13, 2015

[1-6] C. Lopes, P. Camanho, Z. Gürdal, P. Maimí, and E. González: *Low velocity impact damage on dispersed stacking sequence laminates. Part II: Numerical simulations*. Compos. Sci. Technol., vol. 69, no. 7–8, pp. 937–947, 2009

[1-7] A. Muc and W. Gurba: *Genetic algorithms and finite element analysis in optimization of composite structures*. Journal of Composite Structures, vol. 54, no. 2–3, pp. 275–281, 2001

[1-8] T. Sebaey, E. González, C. Lopes, N. Blanco, and J. Costa: *Damage resistance and damage tolerance of dispersed CFRP laminates: Design and optimization*. Journal of Composite Structures, vol. 95, pp. 569–576, 2013

[1-9] T. Kruse, T. Koerwien, R. Ruzek: *Fatigue Behaviour and Damage Tolerant Design of Composite Bonded Joints for Aerospace Application*. 17th European Conference on Composite Materials, Munich, Germany, 2016

[1-10] D. Peeters, M. Abdalla: *Design Guidelines in Nonconventional Composite Laminate Optimization*. Journal of Aircraft, vol. 54, no. 4, pp. 1454-1464, 2017

[1-11] P. Camanho, C. Dávila, S. Pinho, L. Iannucci, P. Robinson: *Prediction of in situ strengths and matrix cracking in composites under transverse tension and in-plane shear*. Journal of Composites: Part A, vol. 37, pp. 165–176, 2006

[1-12] S. Sihn, R. Kim, K. Kawabe, S. Tsai: *Experimental studies of thin-ply laminated composites*. Journal of Composite Science and Technology, vol. 67, pp. 996-1008, 2007

[1-13] R. Amacher, J. Cugnoni, J. Botsis, L. Sorensen, W. Smith, C. Dransfeld: *Thin ply composites: Experimental characterization and modelingof size-effects*. Journal of Composite Science and Technology, vol. 101, pp. 121-132, 2014

2 DESIGN PARAMETERS OF COMPOSITE BONDED JOINTS UNDER TENSILE LOADING

2.1 INTRODUCTION

The strength of an overlap bonded joint under tensile loading conditions is influenced by a variety of design parameters. Before investigating those design parameters in the coming chapters of this Ph.D.-thesis, this chapter gives an overview on what has been done so far to improve the strength of composite bonded joints under tensile loading.
This literature review is divided in four sections, two dedicated to topology design parameters (**section 2.2** and **section 2.3**) and two dedicated to material design parameters (**section 2.4** and **section 2.5**).
Generally, one can cluster the topology design parameters for CFRP overlap bonded joints in two categories: Global and local topology. The global includes different overall joint topology, such as SLJ, Double Overlap Joints (DLJ) or scarf joints, and other general geometric features like overlap length, bond line thickness, in **section 2.2**. The local joint topology includes parameters related with fillet geometry and tapering the tip of the overlap, in **section 2.3**.
The materials present at the joint have also an influence on its overall strength. They can be divided into adhesive materials and adherend materials. In both fields a substantial amount of work was published. **Section 2.4** gives an overview of the adhesive parameters that can be tailored to improve the strength of the joint, while **section 2.5** focusses on the adherend parameters. In the later, CFRP-adherends themselves consist of laminated plies, which can be tailored, for example in terms of fiber orientation, ply thickness or stacking sequence. These adherend or laminate specific design parameters are discussed in detail.

2.2 GLOBAL TOPOLOGY

Various topologies for overlap bonded joints have been studied. **Figure 2-1** shows a general overview of some of the topologies found in literature [2-1, 2-2]. Global joint topologies can thereby be classified into two categories of either disturbed or undisturbed shapes. Disturbed, as in **Figure 2-1** a)-e), is thereby defined, in the context of this thesis, as a joint topology with one or more noticable offsets between the adherends, while undisturbed, as in **Figure 2-1** f)-i), is defined such that the adherends are aligned in parallel flatwise.

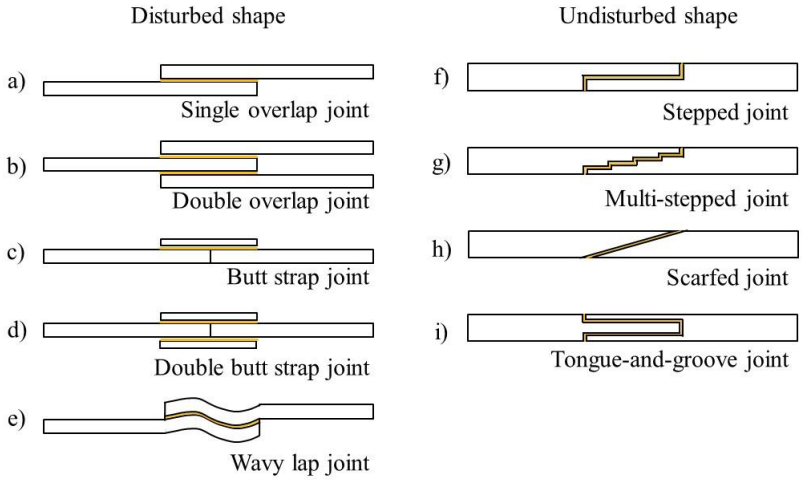

Figure 2-1: Global joint topologies

The most commonly used joint in practise is probably the SLJ, in **Figure 2-1** a), and the reason for this is the easiness of design and manufacturing [2-1]. When the SLJ is under tensile loading, the bonding area suffers shear stress. In addition, the offset between the adherends creates a secondary bending moment which results in peel stresses at the edge of the bond line. In order to reduce the peel stress at the bond line edge, it seems necessary to avoid the offset [2-3 – 2-4]. In a symmetric double lap joint, **Figure 2-1** b), the centre adherend experiences no bending moment, but the outer adherends do, thus giving rise to tensile stresses in the adhesive layer at the unloaded overlap end, and compressive stresses at the loaded overlap end [2-5]. A similar concept is the use of an additional butt strap, aligning both adherends, as can be seen in **Figure 2-1** c). This results in a reduction of peel stresses at the end of the bond line. Adding a second butt strap on the bottom side provides full symmetry. However, the use of butt straps adds weight to the structure and interrupts the aerodynamic efficiency.

2.2.1 Bond line length and adherend/adhesive thickness

Significant amount of work can be found in literature on the effect of overlap length, adherend thickness and adhesive thickness on the joint strength. It has been shown that adhesive joints have their optimum strength for thin bond line thicknesses around 0.1mm to 0.5mm [2-6]. An extensive statistical analysis was performed by da Silva et al. [2-7], studying three different adhesive types against three different bond line thicknesses of 0.2mm, 0.5mm, and 1.0mm. The results showed that average lap shear strength increases as the bond line gets thinner and the adhesive gets tougher. Ozel et al. [2-8] performed 2D non-linear Finite Element Analysis (FEA) on SLJs subjected to bending and found that, the load carried by the SLJ with the flexible adhesive increased with increasing overlap length up to a certain threshold, depending on adherend bending stiffness. Aydin et al. [2-9] predicted the average lap shear strength of SLJ with different adherend thicknesses and overlap length, by using non-linear FEA. It was

demonstrated both numerically and experimentally that, peak peel stress occurs at the free edges of the overlap. Failure originated in two locations: 1) around the central zone of the overlap due to shear stress, and 2) at the free edges of the adhesive layer due to peel stress. Moreover, it was also found that, more stress is transferred from the edge to the center of the overlap with increasing adherend thickness. This was concluded to be the reason for the increase in the strength of joints with increasing adherend thickness at the same overlap length. CFRP and Aluminium (Al) SLJs with different overlap lengths were tested by Kim et al. [2-10], providing a relationship between failure loads, modes, and bond line length. Unlike cohesive failure in the Al-Al joints, it was found that the final failure mode was delamination in the composite adherends. It was also seen that, in joints with a bonding length-to-width ratio smaller than 1, the joint strength increased with increasing bond line length. But in joints with length-to-width ratio larger than 1, the joint strength increased only slightly. In summary, bond line length and thickness were amongst the first design parameters, studied in the context of joint strength, and depending on adherend material, width and thickness, they need to be carefully choosen, before looking into other, more advanced local topology optimizations.

2.2.2 Wavy lap joint

Researchers have constantly been working on new alternative joint designs, looking for better performances. One of these new designs is the bonded wavy lap joint presented by Zeng and Sun [2-11], as can be seen in **Figure 2-2**.

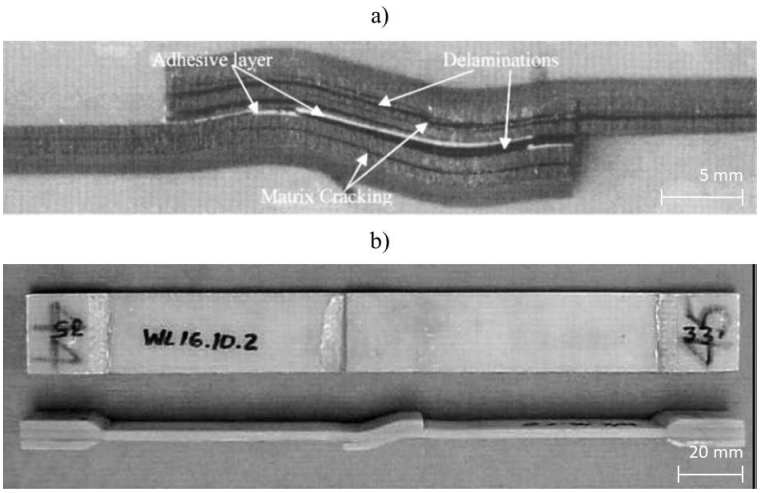

Figure 2-2: Wavy lap joint, a) cross-section of overlap area of Zeng and Sun [2-11], b) wavy lap joint design of Avila and Bueno [2-12] in top and side view

With this new topology, they were able to transfer the shear stress more evenly over the length of the joint than in a SLJ of the same adherend layup and thickness. For the two adherend layups studied, $[0/90/0/90]_{2s}$ and $[90/0/90/0]_{2s}$, the average lap shear strength of the wavy joint was significantly higher than that of conventional SLJs, reaching at least 100% higher average

lapshear strength, σ_{LSS}, for layup $[90/0/90/0]_{2s}$ and at least 50% higher σ_{LSS} for layup $[0/90/0/90]_{2s}$ [2-11]. Avila and Bueno [2-12, 2-13] performed experimental and numerical studies on wavy lap joints with 25mm overlap length, 16-layer plain weave E-glass/epoxy adherends and epoxy paste adhesive. It was found an increase in maximum load of 41%, compared to a reference SLJ-design, which is believed to result from the out-of-plane compressive stresses developed near the tip of the overlaps. Generally, the wavy lap joint appears as an interesting structural optimization concept, turning out-of-plane tensile (peel) into compressive stresses. However, the quite disturbed shape of the overlap region would disqualify for applications such as circumferential joints of aircraft fuselage panels, where aerodynamic aspects play an important role. Aside from the embracing shape of the overlap, studies showed that the joint strength also depends on the chosen layup of the adherends [2-12].

2.2.3 Scarf and stepped joints

Scarf joints or stepped lap joints are often studied in the context of repair of composite laminates. Undisturbed shapes, as in **Figure 2-1** f) to i), avoid offset, while at the same time no extra weight is added. This comes with the cost of a reduced cross-section at the joint area and a geometrically more complex design. A stepped joint is basically a single overlap where the adherends loose half of their initial thickness for the length of the overlap joint. It can result in a decrease of peel stress [2-14]. For a smoother stress distribution, it makes sense to implement several steps. The ultimate level of this idea leads to the scarf joint, where a straight overlap occurs under an angle. Through this optimization, the strength of the joints can be increased by 90% to 150% compared to a reference SLJ-design [2-14]. Wu et al [2-15] compared the damage tolerance of scarf and stepped-lap joints under quasi-static loading, using FEA. Thereby the damage was represented by an artificial interface discontinuity embedded in the bond line between composite adherents. The results showed that the stepped lap joint exhibited better damage tolerance than the scarf joint, assuming the chosen adhesive holds a linear elastic material response. The scarf joint topology can overall provide a smoother stress distribution, but remains challenging to manufacture with CFRP-adherends. Therefore, the stepped joint would be a better candidate for CFRP-bonded joints, especially since multiple steps can be created throughout the lamination process.

2.2.4 Finger joints

Compared to the traditional SLJ-design, finger joints (FJ) are a promising alternative to increase joint strength due to a more gradual load transfer to the composite adherends as they lead to lower peel stresses [2-1, 2-16]. Adams et al. [2-17] published work on step lap joints. It was found that the butted regions at the ends of the fingers will fail under tensile loading. FJs, also referred as tongue-and-groove (TG) joints, are commonly used in the wood industry, where slots are created by profiling the bonding surface with a rotational milling tool. In CFRP-adherends, FJ-topologies were mostly studied for laminates with an adherend thickness above 5 mm [2-

18], such as glass fibre reinforced polymer (GFRP) and composite sandwich structures, to connect, for example, components of wind turbine blades. Sayer et al. [2-18] investigated the effect of FJ-topologies on the fatigue life in bonded wind turbine blades. The connection of the shear web to the spar caps of a wind turbine blade was tested experimentally and a specific FJ-topology (*Henkel UpWind Beam*) was chosen to increase fatigue life over a SLJ design. The use of particular cover laminates at the bond line between spar cap and web resulted in up to 50 times higher joint strength under fatigue loading, compared to a reference beam design without cover laminates. Another method to create a FJ-topology is the so-called *ply interleaving technique* of single plies. This means two adherends with overlapping fingers are laminated together, letting the plies of left and right adherend interleave each other in the joint area. This method is mainly used to join adherends with different materials, such as CFRP/GFRP or CFRP/Titanium, in one co-curing step. Ahamed et al. [2-19] developed a *ply-interleaving technique* for joining quasi-isotropic CFRP/GFRP adherends. The strength of both interleaved-scarf and finger joints were 75% of the un-notched GFRP laminate strength, provided the distance between 0-0 ply terminations exceed a certain threshold value, approximately 6 mm. It was concluded that joint failure is caused by delamination at the location where plies terminate, as well as by transverse matrix cracking within off-axis plies. Dvorak et al. [2-20, 2-21] investigated adhesive FJs for woven E-glass/vinyl-ester composite laminated plates to steel or other composite plates, with applications in ship structures. The study was focussed on the stress distributions inside the FJs. As in other joint configurations, they found peel stress concentrations at the tips of the bonded area, that depend on the local topology of the adherends. They also found a significant advantage of FJ- over SLJ topologies: Peel stresses inside the joint region remained independent from the adherend thickness. Canyurt et al. [2-22] used a genetic algorithm tensile strength estimation model (GATSEM) to estimate the strength of adhesively bonded FJs, considering overlap length (OL), bond line thickness (BLT), pre-stress near the free edges of the bond line and material type of joining parts. With this model they were able to optimize the overlap length and bond line thickness for maximum fatigue life. Compared to an initial FJ-configuration with reference overlap length and bond line thickness, the fatigue life could be increased by 219% for CFRP/CFRP, by 182% for steel/CFRP and by 195% for Al/CFRP FJ-configurations. This significant improvement in joint strength under fatigue loading demonstrates how much effect the parameters OL and BLT have on the overall joint strength, as discussed in **section 2.2.1**. Generally, the finger joint, as a type of a multi-stepped lap joint, seems a promising candidate for overall joint strength enhancement. The difficult part is, to perform a sufficient surface pre-treatment prior to the bonding process and to assure accurate geometrical tolerances in the assembly. Nevertheless, Ahamed et al. [2-19] could demonstrate the technical feasibility of very narrow finger slots with their ply interleaving method, at least in a co-curing step.

2.3 LOCAL TOPOLOGY

2.3.1 Spew fillet shapes and adherend taper

Local joint topology parameters have shown to have a significant influence on the overall joint strength, such as in the areas of the stress concentration, by tapering the adherend edges and adding a spew fillet at the edges of the adhesive [2-23]. Shaping locally the adherend and/or adhesive edges can provide a smoother transition in the joint geometry, reducing the stress concentration. Work performed in metal-to-composite DLJs show that the combination of inside taper and spew fillet can reduce the stresses by up to 50% in comparison with the basic design, resulting in an increase in strength of up to 50% [2-23 - 2-27]. However, if thermal loads become significant, such as at low temperatures, inside taper and spew fillet decrease the overall strength. For composite SLJ, shaping the adhesive fillet and chamfering the composite adherend also reduce the stress concentrations at the substrate, which can result in an increase up to 30% in strength [2-28 – 2-32]. **Figure 2-3** presents an overview of spew fillet designs after Lang and Mallick [2-28].

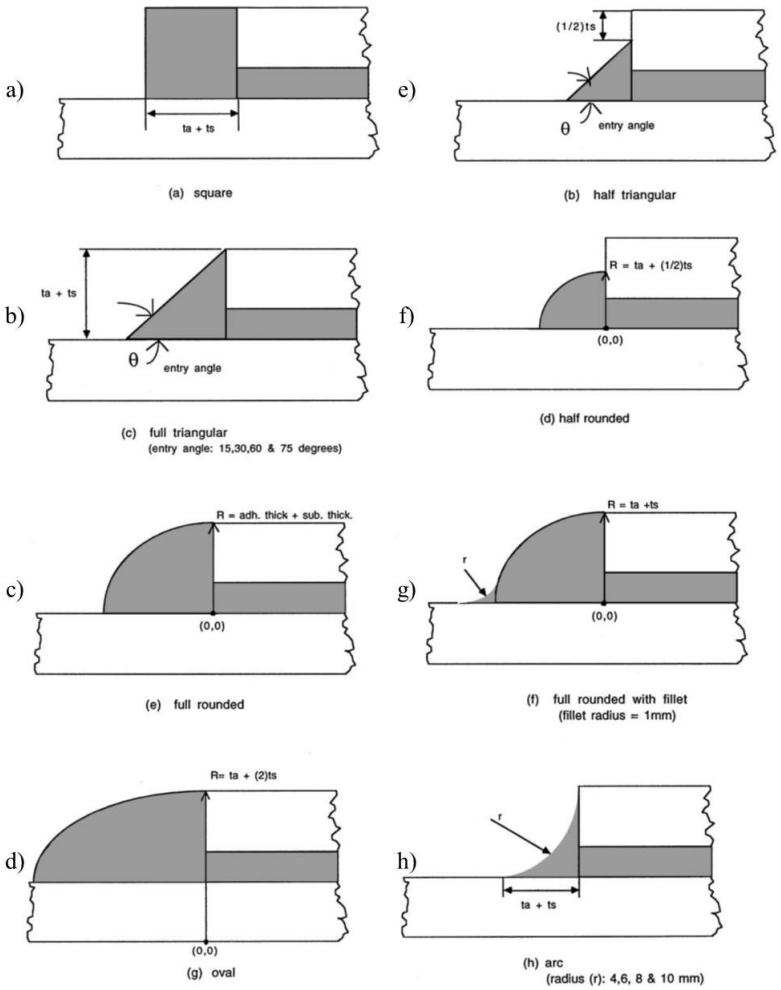

Figure 2-3: Spew fillet designs to reduce stress concentrations at the overlap edge, after Lang and Mallick [2-28]

Nevertheless, it is also agreed in literature that the strength increase based on local topology changes, highly depends on the materials properties (adhesive and adherend) and load conditions (if thermal loads are significant), so there is no generalized rule [2-32]. Schollerer et al. [2-33] investigated different state-of-the-art concepts to reduce the peel stress at the bond line tip of SLJs, by chamfering, different adhesive spew fillet geometries, and a mixed adhesive joint, see **Figure 2-4**.

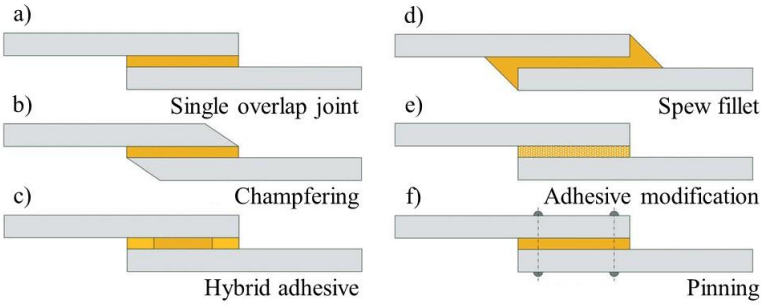

Figure 2-4: State-of-the-art joint designs after Schollerer et al [2-33]

These designs were compared to a novel local adherend surface toughening concept, using a thermoplastic Polyvinylidenfluorid (PVDF) layer, illustrated in the following **Figure 2-5**. They found that the local surface toughening concept was more efficient in increasing overall joint strength than the state-of-the-art concepts. The joint strength for the surface toughening specimens could be increased by 84% compared to the reference SLJ design, outperforming all other concepts of **Figure 2-4**. However, this result is not exactly in line with other studies on local topology optimization, and it is, once again, highly dependent on the adhesive bond line length, the adhesive thickness, and on the length of the surface toughening patch. Generally, local topology optimization through taper and spew fillet shaping appears to be an effective way to reduce particularly the high peak peel stresses at the bond line tips, but at the same time it has to be in line with a well-designed global joint topology.

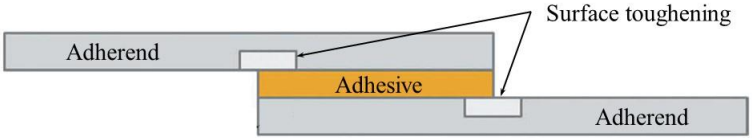

Figure 2-5: Surface toughening method after Schollerer et al [2-33]

2.4 ADHESIVE MATERIALS

It is important to distinguish between adhesive strength and joint strength. The joint strength may not increase if a stronger adhesive is used. A strong and stiff adhesive will withstand higher stresses but its high stiffness will rapidly increase stress concentrations at the edges. A flexible adhesive will distribute more evenly the stresses along the bonded area, but it is generally less strong and will withstand lower stresses before failure [2-34]. To overcome this bottleneck, a large amount of work was published on varying the material properties of the adhesive along the overlap, either by placing different adhesive at the edges and at the center of the overlap (mixed or dual adhesive) or by grading the adhesive properties along the overlap.

2.4.1 Mixed adhesives

Da Silva et al. [2-35, 2-36] performed experimental lap shear tests with the same brittle adhesive for the center part but three different ductile adhesives for the tip region of the overlap. The mixed-adhesive technique was found to give up to 221% increase in joint strength compared to a ductile adhesive alone, and up to 212% increase in joint strength compared to a brittle adhesive alone. It was concluded that, for a mixed adhesive joint to be stronger than the brittle and the ductile adhesive used individually, the load carried by the brittle adhesive must be higher than that carried by the ductile adhesive [2-36]. In the work on surface toughening, from previous **section 2.3.1**, Schollerer et al. [2-33], also studied the concept of a mixed adhesive in order to decrease stress peaks on the tip of the bond line, see **Figure 2-4** c). A reduction of 30% in shear stress and 60% in peel stress was numerically demonstrated at the bond line tip, compared to a SLJ reference design with one continuous adhesive. However, this promising stress analysis could not be further validated through experimental data. Loebel et al. [2-37] presented a hybrid bond line concept for CFRP bonded joints, implementing a rather ductile thermoplastic adhesive towards both tips and a brittle epoxy adhesive in the center of the bond line of a SLJ, so that a physical barrier for growing disbonds was obtained, providing a fail-safe design, see **Figure 2-6**. For this design, it was needed to combine the two different joining techniques of adhesive bonding and thermoplastic welding. The study demonstrates that manufacturing complexity, in the form of two different joining methods can be overcome.

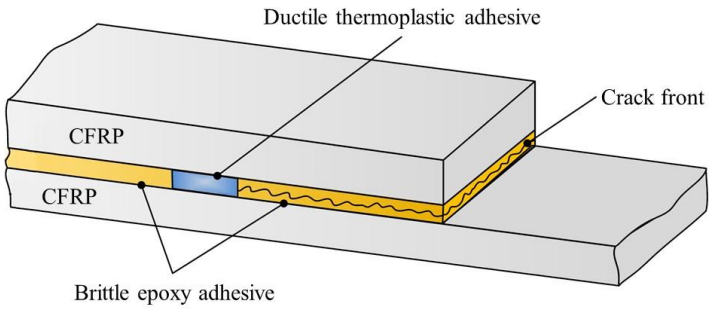

Figure 2-6: Hybrid thermoplastic-thermoset bond line concept for CFRP-SLJs after Loebel et al. [2-37]

Da Silva and Adams [2-38] proposed a numerical FEA on strength predictions for DLJs, used over a wide temperature range. Following the mixed modulus concept described by Hart-Smith [2-39], a brittle adhesive with high modulus in the middle of the joint retains the strength and transfers the entire load at high-temperatures, while a ductile adhesive at the ends of the joint is the load-bearing adhesive at low-temperatures. Figure 2.7 summarizes the results of the study. It should be stressed out, that this study is based on a riveted specimen design, but results, such as yielding load over temperature, can be discussed nontheless. The legend entries *Supreme 10HT*, *Redux 326* and *MAJ3* refer to the names of different adhesive systems, with *Redux 326* being the stiff and brittle high-temperature adhesive and *Supreme 10HT* being the ductile low-

temperature adhesive. A mixed adhesive joint (*MAJ3*) is the third of several functionally graded combinations of both systems, that were studied. As can been seen from the figure, for a joint with dissimilar adherends, the combination of two adhesives, in **Figure 2-7** referenced as *MAJ3*, was found to give a higher load capacity over the full temperature range than the use of a high-temperature adhesive alone.

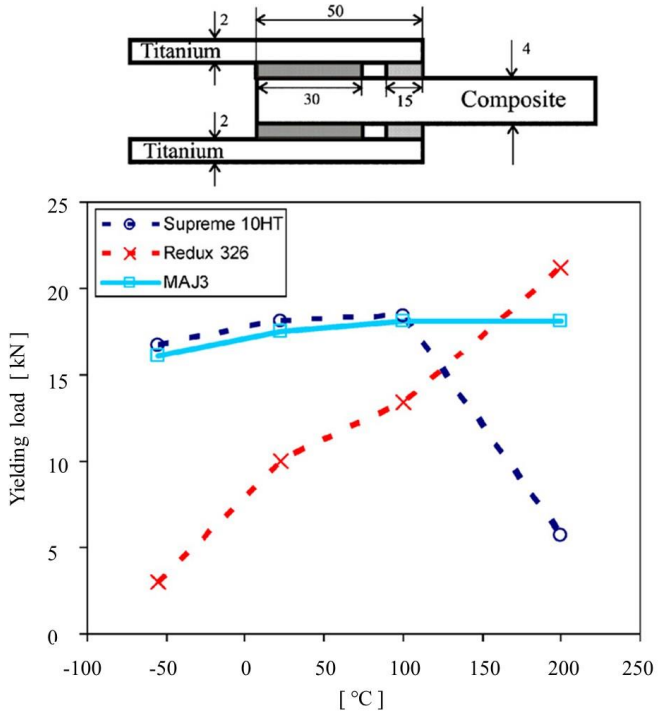

Figure 2-7: Yielding load of functionally graded CFRP-Titanium bolted DLJs over a wide range of temperature, after da Silva and Adams [2-38]

Neves et al. [2-40] extended the previous work with analytical models. Over the entire overlap length, adhesive shear and peel stress distributions of the analytical model were in very close agreement with the previous FEA of da Silva and Adams [2-38].

2.4.2 Functionally graded adhesives

Durodola [2-41] reviewed a wide range of theoretical and experimental work on the use of functionally graded adhesive bonding from the 1960s to date. Studies generally agree on the conclusions that, strength of bonded joints can be significantly increased with functionally graded adhesive, compared to a constant modulus adhesive. In particular along the bond line at mid-thickness, peel stress is more sensitive than shear stress to changes in adhesive tensile modulus grading. Variable modulus adhesives were studied by Fitton and Broughton [2-42] as

an approach to optimise joint strength. In agreement with previous literature [2-35 – 2-40], it was concluded that bond lines with variable modulus in the adhesive can reduce stress concentrations and consequently increase joint strength. The variable modulus of the adhesive also changed the failure mode, from interlaminar failure inside the adherend for constant, high modulus adhesive to cohesive failure for a variable modulus bond line. Stein et al. [2-43] proposed a closed-form analytical solution for stress distribution of functionally graded adhesive lap joints with laminated adherends of any joint configuration. It was identified an effect of locally incorrect stress results at the very ends of the overlap, occurring within their employed framework. Interestingly, it was concluded that, for design studies or widely used non-local failure criteria, this drawback was shown to be of minor importance. Overall, the concept of mixed and functionally graded adhesives appears to be a good candidate in order to disseminate local peel stress concentrations around the tip of the overlap. It is also a suitable design, if joints are exposed over a wide range of temperature or for joints with dissimilar adherend materials or bending stiffnesses. A dual adhesive, same as the tapered spew fillet described in previous **section 2.3.1**, could therefore be combined with other global topology concepts, like a finger joint, in order to achieve higher joint strength than with each of these concepts individually.

2.5 ADHEREND MATERIALS

2.5.1 Adherend bending stiffness

Ganesh and Choo [2-44] have varied the braiding angle of composite materials to vary the adherend elastic modulus along the overlap length. Numerical simulations show a decrease of 20% in the peak shear stress at mid-thickness of the adhesive layer, when using a variation of braiding angle from 10° to 35° in comparison with the reference joint with constant braiding angle of 10°. Boss et al. [2-45] found that the combination of this technique with local topology changes, such as tapering the adherends, can further decrease the peak shear stress by another 20%. Finally, it was pointed out that, modulus grading of adherends is simpler to implement in terms of manufacturing than geometrical grading through tapering.

2.5.2 Stacking sequence and layup variation

Another way to modify the adherend stiffness or overlap properties in composite adherends is to tailor the laminate stacking sequence. Research in the field of composites shows that certain stacking sequences can retard delamination. Therefore, making use of the anisotropy of the composite could potentially counteract their poor out-of-plane strength, which can have a positive impact on the performance of composite adhesively bonded joints subject to peel stresses. However, the few publications found on this topic give contradictory results: The stress analysis of Renton and Vinson [2-46] and Aydin [2-47], showed that 0° plies close to the bond line give smoother stress distribution both at the adherends and at the adhesives. Nevertheless,

tests performed by Purimpat [2-48] showed that larger angles close to the bond line result in a more complex crack path and increase the final joint strength up to 30%. Similar trends were found under fatigue loading, in which a 45° angle close to the bond line increased significantly the crack propagation resistance [2-49, 2-50]. Finally, Ozel [2-51] showed that by only varying the composite layup, the lap shear strength can vary up to 120%. Thus, there is a clear potential to improve strength of the SLJ by tailoring the composite adherend properties.

2.5.3 Ply thickness

Thin plies are currently among the most promising approaches to improve the performance of CFRPs due to their ability to enhance the off-axis performance of composites and postpone delamination. With the development of the fiber tow spreading technology, it is nowadays possible to produce laminates with a very thin single ply thickness, meaning from conventional size (> 100μm) down to about 20μm [2-52]. Significant research was carried out to evaluate the mechanical performance of thin plies in comparison with conventional composites. Camanho at al. [2-53] experimentally demonstrated that a decrease in ply thickness would lead to a delay of matrix cracking and delamination growth and would therefore enhance the mechanical performance of the composite laminate in their off-axis and out-of-plane directions. Sihn et al. [2-54] published an experimental study of composite thin ply laminates in 2007. Uniaxial tensile tests under static and fatigue loading were carried out on unnotched and open-hole (OHT) specimens. Tests on impact and compression strength after impact (CAI) were also conducted. By analysing stress–strain curves, and by applying several measurement techniques, such as Acoustic Emission (AE), X-ray photography and ultrasonic C-scanning, they observed that micro-cracking, delamination and splitting damage were suppressed in thin ply laminates under static, fatigue and impact loadings. Yokozeki et al. [2-55] performed similar experimental studies to prove that the decrease of ply thickness would have an effect on strength and damage resistance of the laminates. The results showed superior characteristics of thin ply laminates on static tension, tension-tension in fatigue, on no-hole compression strength (NHC), open-hole compression strength (OHC) and CAI tests. About 10% increase in OHC and CAI strength was measured with decreasing the ply thickness from 145g/m^2 to 75g/m^2. In addition, a decrease in damage accumulation was found for thin plies in uniaxial tensile tests using AE measurement techniques. Arteiro et al. [2-56] developed a micro-mechanical finite element (FE) model of a composite sub-laminate, in order to accurately represent the micro-mechanical response of composite laminates with thin plies. The model consisted of a representative volume element of a 90° ply in between two homogenised $\pm\ \theta°$ plies. The theory of in-situ strength presented earlier by Camanho et al. [2-53] was applied to demonstrate that a decrease in ply thickness can be correlated to an in-situ effect, characterised by a reduction in the applied stress, that was needed to extend a transverse crack along the thickness of the ply when the ply thickness increases. Furthermore, the in-situ effect was identified to play an important role on the delay of other matrix-dominated failure mechanisms [2-56]. Amacher et al. [2-52] followed the work of Yokozeki et al. [2-55] using the same approach of experimental characterization. The results agreed very well with previous research of Sihn et al. [2-54], showing that thin ply composites

exhibit a significant delay in damage initiation in comparison with conventional laminates. By using different ply thicknesses, ranging from 30g/m^2 to 300g/m^2 in quasi-isotropic (QI) tensile tests, quasi-brittle failure was identified in the thin plies instead of extensive delamination and transverse cracking patterns in thick plies. Arteiro et al. [2-57] recently published a comprehensive review on thin ply polymer composite materials. It was well concluded that thin plies improve the in-plane matrix related allowable, but can also enhance residual strength and damage tolerance. Moreover, the increased design flexibility allows for multifunctional optimisation with great potential regarding weight and cost reduction [2-57]. Therefore, the thin plies concept is a promising candidate to help increasing joint strength in the challenge of this thesis.

2.5.4 Interface topology and interlayer toughening

Bisagni et al. [2-58] carried out experimental studies to investigate the behaviour of bonded CFRP joints with through-thickness local reinforcement. Spiked thin metal sheets were inserted as local interlaminar reinforcement, which enabled a significant delay in damage progression under cyclic loading, when compared to pristine joints. Shang et al. [2-59] worked on improving the resistance to delamination of composite adhesive joints by using a novel CFRP laminate with a reinforced high toughness resin on the bond line surface. Results showed an increase of 22% in average lap shear strength, compared SLJs with non-toughened resin on the surface. They observed, how the failure mode changed from delamination inside the adherends in case of the non-toughended to cohesive failure in the adhesive in case of the surface-toughened adherends. Finally, Cugnoni et al. [2-60] evaluated eight different formulations of thin ply composites ranging from low modulus to high modulus carbon fibres through compression strength after impact (CAI) and open hole tensile (OHT) tests. They concluded that, for thin ply composites, the maximum strength is limited by the ultimate strain of the fibre. By adding a thermoplastic interlayer toughening component, they could show an increase in damage resistance in the thin plies.

2.6 CONCLUSION

Chapter 2 reflects on the topics investigated in literature to improve the lap shear strength of a bonded joint, mainly under quasi-static loading. While some parameters like overlap length and adhesive thickness are fairly well studied, others like functionally graded adhesives were more recently discovered. Particularly those concepts of increasing out-of-plane properties, which are related to the laminate specific parameters, such as fiber orientation, ply thickness and ply interleaving, are not yet well understood and represent a great potential. On the fiber orientation, there were several different studies conducted with non-conclusive results. The beneficial effect of thin plies was demonstrated so far on CFRPs alone but never investigated in the context of bonded joints. Global topology change by means of ply interleaving technique also has a great potential to reduce peak peel and shear stresses but could so far only be achieved in co-cured repair patches.

The aim of this work is therefore, to further explore the potential of these laminate specific design parameters on the lap shear strength of CFRP bonded joints. Shang et al. [2-61] recently reviewed various techniques to reduce peel stresses inside laminated adherends. They concluded that global design parameters, such as overlap length, bond line thickness or fillet design may have a more significant effect on the lap shear strength. Therefore, it is expected that a change in global joint topology, such as an FJ-design with interleaved plies, would lead to higher increase in lap shear strength than a local change in fiber orientation and ply thickness, but at the cost of a more complex joint production and assembly.

REFERENCES

[2-1] R. Adams: *Strength Predictions for Lap Joints, Especially with Composite Adherends. A Review.* Journal of Adhesion, vol. 30, pp. 219-242, 1989

[2-2] S. Teixeira de Freitas, J. Sinke: *Failure analysis of adhesively-bonded skin-to-stiffener joints: Metal–metal vs. composite–metal*. Eng. Failure Analysis, vol. 56, pp. 2-13, 2015

[2-3] P. Cooper, J. Sawyer: *A Critical Examination of Stresses in an Elastic Single Lap Joint.* NASA Technical Paper 1507, 1979

[2-4] K. GültekİN, S. AkpİNar, A. Özel, G. Öner: *Effects of unbalance on the adhesively bonded composites-aluminium joints.* Journal of Adhesion, vol. 93, pp. 674-687, 2016

[2-5] N. Chowdhury, J. Wang, W. Chiu, P. Chang: *Experimental and finite element studies of thin bonded and hybrid carbon fibre double lap joints used in aircraft structures.* Composites Part B: Engineering, vol. 85, pp. 233-242, 2016

[2-6] D. Gleich, M. van Tooren, A. Beukers: Analysis and evaluation of bondline thickness effects on failure load in adhesively bonded structures. Journal of Adhesion Science and Technology, vol. 15, pp. 1091-1101, 2001

[2-7] L. da Silva, T. Rodrigues, M. Figueiredo, M. de Moura, J. Chousal: *Effect of Adhesive Type and Thickness on the Lap Shear Strength.* Journal of Adhesion, vol. 82, pp. 1091-1115, 2006

[2-8] A. Ozel, M. Aydin, S. Tembliz: *The effects of overlap length and adherend thickness on the strength of adhesively bonded joints subjected to bending moment.* Journal of Adhesion Science and Technology, vol. 18, pp. 313-325, 2004

[2-9] M. Aydin, A. Ozel, S. Tembliz: *The effect of adherend thickness on the failure of adhesively bonded single-lap joints.* Journal of Adhesion Science and Technology, vol. 19, pp. 705-718, 2005

[2-10] T. Kim, J. Kweon*, J. Choi: *An Experimental Study on the Effect of Overlap Length on the Failure of Composite-to-Aluminum Single-Lap Bonded Joints.* Journal of Reinforced Plastics and Composites, vol. 27, pp. 1071-1081, 2008

[2-11] Q. Zeng, C. Sun: *Novel design of a bonded lap joint*. American Institute of Aeronautics and Astronautics (AIAA) Journal, vol. 39, pp. 1991 – 1996, 2001

[2-12] A. Avila, P. Bueno: *An experimental and numerical study on adhesive joints for composites.* Composite Structures, vol. 64, pp. 531-537, 2004

[2-13] A. Avila, P. Bueno: *Stress analysis on a wavy-lab bonded joint for composites.* Int. Journal of Adhesion and Adhesives, vol. 24, pp. 407-414, 2004

[2-14] L. da Silva, R. Adams: *Techniques to reduce the peel stresses in adhesive joints with composites.* Int. Journal of Adhesion and Adhesives, vol. 27, pp. 227-235, 2007

[2-15] C. Wu, C. Chen, L. He, W. Yan: *Comparison on damage tolerance of scarf and stepped-lap bonded composite joints under quasi-static loading.* Composites Part B, vol. 155, pp. 19-30, 2018

[2-16] A. Crocombe, I. Ashcroft: Modelling of Adhesively Bonded Joints. Springer, 2008, Chapter 1: Simple Lap Joint Geometry, ISBN: 978-3-540-79055-6

[2-17] R.D. Adams, J. Comyn, W.C. Wake: *Structural Adhesive Joints in Engineering*. Springer Science & Business Media, 1997

[2-18] F. Sayer*, A. Antoniou, A. van Wingerde: *Investigation of structural bond lines in wind turbine blades by sub-component tests*. Int. Journal of Adhesion & Adhesives, vol. 37, pp.129-135, 2012

[2-19] J. Ahamed, M. Joosten, P. Callus, S. John, C.H. Wang: *Ply-interleaving technique for joining hybrid carbon/glass fibre composite materials*. Composites Part A, vol. 84, pp. 134-146, 2016

[2-20] G.J. Dvorak, J. Zhang, O. Canyurt: *Adhesive tongue-and-groove joints for thick composite laminates*. Composite Science and Technology, vol. 61, pp 1123–1142, 2001

[2-21] K. Matous, G.J. Dvorak: *Analysis of tongue and groove joints for thick laminates.* Composites Part B, vol. 35, pp. 609-617, 2004

[2-22] O.E. Canyurt, C. Meran, M. Uslu: *Strength estimation of adhesively bonded tongue and groove joint of thick composite sandwich structures using genetic algorithm approach.* Int. Journal of Adhesion and Adhesives, vol. 30, pp. 281-287, 2010

[2-23] G. Belingardi, L. Goglio, A. Tarditi: *Investigating the effect of spew and chamfer size on the stresses in metal/plastics adhesive joints.* Int. Journal of Adhesion and Adhesives, vol. 22, pp. 273-282 ,2002

[2-24] R. Adams, R. Atkins, J. Harris, A. Kinloch: *Stress analysis and failure properties of carbon fibre-reinforced plastic/steel double-lap joints.* Journal of Adhesion, vol. 20, pp. 29-53, 1986

[2-25] M. Hildebrand: *Non-linear analysis and optimization of adhesively bonded single lap joints between fibrereinforced plastics and metals.* Int. Journal of Adhesion and Adhesives, vol. 14, pp. 261-267, 1994

[2-26] A. Rispler, L. Tong, G. Steven, M. Wisnom: *Shape optimisation of adhesive fillets.* Int. Journal of Adhesion and Adhesives, vol. 20, pp. 221-231, 2000

[2-27] R. Kaye, M. Heller: *Through-thickness shape optimisation of typical double lap-joints including effects of differential thermal contraction during curing.* Int. Journal of Adhesion and Adhesives, vol. 25, pp. 227-238, 2005

[2-28] T. Lang, P. Mallick: *Effect of spew geometry on stresses in single lap adhesive joints.* Int. Journal of Adhesion and Adhesives, vol. 18, pp. 167-177, 1998

[2-29] M. Tsai, J. Morton: *The effect of a spew fillet on adhesive stress distributions in laminated composite single-lap joints.* Composite Structures, vol. 32, pp. 123-131, 1995

[2-30] R. Campilho, M. de Moura, J. Domingues: *Numerical prediction on the tensile residual strength of repaired cfrp under different geometric changes.* Int. Journal of Adhesion and Adhesives, vol. 29, pp. 195-205, 2008

[2-31] E. Moya-Sanz, I. Ivanez, S. Garcia-Castillo: *Effect of the geometry in the strength of single-lap adhesive joints of composite laminates under uniaxial tensile load.* Int. Journal of Adhesion and Adhesives, vol. 72, pp. 23-29, 2017

[2-32] S. Budhe, M. Banea, S. de Barros, L. da Silva: *An updated review of adhesively bonded joints in composite materials*. Int. Journal of Adhesion and Adhesives, vol. 72, pp. 30–42, 2017

[2-33] M.J. Schollerer, J. Kosmann, O. Völkerink, D. Holzhüter, C. Hühne: *Surface toughening – a concept to decrease stress peaks in bonded joints*. Journal of Adhesion, vol. 95, pp. 495-514, 2019

[2-34] S. Teixeira de Freitas, J. Sinke*: Failure analysis of adhesively bonded metal-skin-to-composite-stiffener: effect of temperature and cyclic loading.* Journal of Composite Structures, vol. 166, pp. 27-37, 2017

[2-35] L. da Silva, M. Lopes: *Joint strength optimization by the mixed-adhesive technique.* Int Journal of Adhesion and Adhesives, vol. 29, pp. 509-514, 2009

[2-36] P. das Neves, L. Da Silva, R. Adams: *Analysis of mixed adhesive bonded joints part I: Theoretical formulation.* Journal of Adhesion Science and Technology, vol. 23, pp. 1-34, 2009

[2-37] T. Loebel, D. Holzhueter, M. Sinapius, C. Huehne: *A hybrid bondline concept for bonded composite joints.* Int. Journal of Adhesion and Adhesives, vol. 68, pp. 229-238, 2016

[2-38] L. Da Silva, R. Adams: *Joint strength predictions for adhesive joints to be used over a wide temperature range.* Int. Journal of Adhesion and Adhesives, vol. 27, pp. 362-379, 2007

[2-39] L. Hart-Smith: *Adhesive-bonded double-lap joints*. NASA Report CR-112235, 1973

[2-40] P. das Neves, L. Da Silva, R. Adams: *Analysis of mixed adhesive bonded joints part II: Parametric study.* Journal of Adhesion Science and Technology, vol. 23, pp. 35-61, 2009

[2-41] M. Fitton, J. Broughton: *Variable modulus adhesives: an approach to optimised joint performance.* Int. Journal of Adhesion and Adhesives, vol. 25, pp. 329-336, 2005

[2-42] N. Stein, P. Weissgraeber, W. Becker: *Stress solution for functionally graded adhesive joints.* Int. Journal of Solids and Structures., vol. 97/98, pp. 300-311, 2016

[2-43] J. Durodola: *Functionally graded adhesive joints: a review and prospects.* Int Journal of Adhesion and Adhesives, vol. 76, pp. 83-89, 2017

[2-44] V. Ganesh, T. Choo: *Modulus graded composite adherends for single-lap bonded joints.* Journal of Composite Materials, vol. 36, pp. 1757-1767, 2002

[2-45] J. Boss, V. Ganesh, C. Lim: *Modulus grading versus geometrical grading of composite adherends in single-lap bonded joints.* Composite Structures, vol. 62, pp. 113-121, 2003

[2-46] J. Renton, J. Vinson: *The efficient design of adhesive bonded joints*. Journal of Adhesion, vol. 3, pp. 175-193, 1975

[2-47] M. Aydin: *3-D Nonlinear Stress Analysis on Adhesively Bonded Single Lap Composite Joints with Different Ply Stacking Sequences*. Journal of Adhesion, vol. 84, pp. 15-36, 2008

[2-48] S. Purimpat, R. Shahram, A. Shahram: *Effect of fibre angle orientation on a laminated composite single-lap adhesive joint*. Journal of Advanced. Composite Materials, vol. 22, no. 3, pp. 139-149, 2013

[2-49] G. Meneghetti, M. Quaresimin, M. Ricotta: *Influence of the interface ply orientation on the fatigue behaviour of bonded joints in composite materials*. Int. J. Fatigue, vol.

32, no. 1, pp. 82-93, 2010

[2-50] G. Meneghetti, M. Quaresimin, M. Ricotta: *Damage mechanisms in composite bonded joints under fatigue loading*. Composites: Part B, vol. 43 pp. 210-220, 2012

[2-51] A. Ozel, B. Yazici, S. Akpinar, M. Aydin, S. Temiz: *A study on the strength of adhesively bonded joints with different adherends*. Composites: Part B, vol. 62 pp. 167-174, 2014

[2-52] R. Amacher, J. Cugnoni, J. Botsis, L. Sorensen, W. Smith, C. Dransfeld: *Thin ply composites: Experimental characterization and modelingof size-effects.* Composite Science and Technology, vol. 101, pp. 121-132, 2014

[2-53] P. Camanho, C. Dávila, S. Pinho, L. Iannucci, P. Robinson: *Prediction of in situ strengths and matrix cracking in composites under transverse tension and in-plane shear*. Composites Part A, vol. 37, pp. 165-176, 2006

[2-54] S. Sihn, R. Kim, K. Kawabe, S. Tsai: *Experimental studies of thin-ply laminated composites.* Composite Science and Technology, vol. 67, pp. 996-1008, 2007

[2-55] T. Yokozeki, Y. Aoki, T. Ogasawara: *Experimental characterization of strength and damage resistance properties of thin-ply carbon fiber/toughened epoxy laminates.* Composite Structures, vol. 82, pp. 382-389, 2008

[2-56] A. Arteiro, G. Catalanotti, A. Melro, P. Linde, P. Camanho: *Micro-mechanical analysis of the in-situ effect in polymer composite laminates.* Composite Structures, vol. 116, pp. 827-840, 2014

[2-57] A. Arteiro, C. Furtado, G. Catalanotti, P. Linde, P. Camanho: *Thin-ply polymer composite materials: a review*. Composites Part A, vol. 132, 2020

[2-58] C. Bisagni, D. Furfari, M. Pacchione: *Experimental investigation of reinforced bonded joints for composite laminates.* Journal of Composite Materials, vol. 52, pp. 431-447, 2018

[2-59] X. Shang, E.A.S. Marques, J.J.M. Machado, R.J.C. Carbas, D. Jiang, L.F.M. da Silva: *A strategy to reduce delamination of adhesive joints with composite substrates*. Proceedings of the Institution of Mechanical Engineers, Part L: Journal of Materials: Design and Applications, Special Issue MDA2018

[2-60] J. Cugnoni, R. Amacher, S. Kohler, J. Brunner, E. Kramer, C. Dransfeld, W. Smith, K. Scobbie, L. Sorensen, J. Botsis: *Towards aerospace grade thin-ply composites: Effect of ply thickness, fiber, matrix and interlayer toughening on strength and damage tolerance.* Composite Science & Technology, vol. 168, pp. 467-477, 2018

[2-61] X. Shang, E. Marques, J. Machado, R. Carbas, D. Jiang, L. da Silva: *Review on techniques to improve the strength of adhesive joints with composite adherends*. Composites Part B, vol. 177, 2019

3 STEERING THE FAILURE MECHANISM: HOW VARIATION IN STACKING SEQUENCE INFLUENCES THE DAMAGE EVENTS

This chapter is based on the journal article: J. Kupski, S. Teixeira de Freitas, D. Zarouchas, P. Camanho, R. Benedictus: *Composite layup effect on the failure mechanism of single lap bonded joints.* Journal of Composite Structures, vol. 217, pp. 14-26, 2019 [3-1].

3.1 INTRODUCTION

A review of previous studies in **Chapter 2** depicts a general agreement: increasing the SLJ longitudinal bending stiffness, either by increasing the number of 0° layers or by placing those near the outside faces of the adherends, results in a reduction of peel stresses at the tips of the bond line and increases the overall joint strength under tensile loading.

However, there is no common agreement on the most beneficial layup sequence to increase the load at damage initiation compared to one at maximum failure load. While some studies have indicated that a 0° layer close to the interface with the adhesive will lead to higher load strength [3-2], other studies show the opposite, stating that larger angles will increase the joint strength [3-3]. This also leads to paradoxical results in terms of the most beneficial failure mode, along with the highest joint strength (if there is any consistency): some studies claim that cohesive failure leads to higher strengths [3-4] while other show benefits in the more complex intra-ply failure to the joint strength [3-5]. In-plane longitudinal bending stiffness may be the most relevant design parameter to decrease peak peel stresses, which correlates with a 0° ply orientation adjacent to the bond line interface and subsequently a cohesive failure inside the adhesive material. But this choice may only be valid until damage initiation. At final failure, the situation might be different.

The missing piece is, therefore, to analyse the failure modes of lap joints with various layups and to analyse the corresponding load at damage initiation, as well as the maximum load, in order to address those discrepancies. This chapter aims to address these questions by giving more insight into the effect of the laminate layup on the damage initiation and final failure of composite SLJs. Adhesively bonded SLJs made from CFRP-adherends with different layups and epoxy film adhesive are analysed experimentally and numerically. An implementation into a 3D finite element model gives insight into the stress field around the bond line and explains the failure mechanisms.

3.2 MATERIALS AND SPECIMENS

3.2.1 Materials

The materials used for this study were unidirectional pre-impregnated (Prepreg) tapes from carbon fibres and epoxy resin in combination with an epoxy film adhesive. The Prepreg tape was *Hexply® F6376C-HTS (12K)-5-35%* (*HEXCEL Composites in Duxford, UK*), containing high tenacity *Tenax®-E HTS45* standard modulus fibres (*TOHO TENAX Europe GmbH*) and the *Hexply® F6376* thermoplastic-toughened epoxy matrix system. The adhesive was chosen *Hysol® EA 9695™ 050K AERO* in 240g/m^2 areal weight, including a knit supporting carrier (*HENKEL AG & Co. KGaA in Duesseldorf, Germany*). The relevant material parameters, extracted from technical datasheet (TDS) [3-6, 3-7], as well as from previous studies with similar adhesives [3-5, 3-8], are presented in **Table 3-1** and **Table 3-2**. All values are valid at room temperature (23°C). Indices are given for different coordinate directions with "1", '2' and "3" standing for the direction along in-plane longitudinal, in-plane transverse and out-of-plane, and with "T" and "C" standing for "tensile" and "compressive", respectively.

Longitudinal tensile strength	X_T	2274MPa[a]
Longitudinal compressive strength	X_C	1849MPa[a]
Transverse tensile strength	Y_T	102MPa[a]
Transverse compressive strength	Y_C	255MPa[a]
Longitudinal tensile modulus	E_{11T}	142000MPa[a]
Transverse tensile modulus	$E_{22T} = E_{33T}$	9100MPa[a]
In-plane shear modulus	$G_{12} = G_{13}$	5200MPa[a]
Transverse shear modulus	$G_{23} = E_{33T} / (2(1+\nu_{23}))$	3500MPa[a]
In-plane shear strength	$S_{12} = S_{13}$	63MPa[a]
Transverse shear strength	S_{23}	35MPa[a]
In-plane Poisson's ratio	$\nu_{12} = \nu_{13}$	0.27[b]
Transverse Poisson's ratio	ν_{23}	0.30[b]

[a] TDS of *Hexply® F6376C-HTS (12K)-5-35%*, *HEXCEL / AIRBUS* [3-6]

[b] adapted from *Hexply-8552/IM7*, Camanho et al. [3-7]

Table 3-1: Adherend material properties

It must be stated that the value of transverse tensile strength Y_T, as provided by the TDS of *Hexply® F6376C-HTS (12K)-5-35%, HEXCEL / AIRBUS* [3-6], seems arguably high, as typical values for state-of-the-art, thermoplastic-toughened systems, such as Hexply M21E, reach about 80MPa [3-8]. Therefore, an additional material test according to *ASTM-D3039-14* was performed, to experimentally confirm those values, which are suggested by the datasheet. The results of the quasi-static transverse tensile test are presented in-depth in **APPENDIX G**.

Tensile strength	X_{Adh}	48MPa[a]
Tensile modulus	E_{Adh}	2019MPa[a]
Poisson's ratio	ν_{adh}	0.34[b]

[a] Teixeira et al. [3-5]

[b] TDS of *Hysol® EA 9695™ 050K AERO* in 240g/m² [3-9]

Table 3-2: Adhesive material properties

3.2.2 Specimens

Specimens were built according to the American Society for Testing and Materials (*ASTM*) *D 5868-01* [3-10], with a constant overlap length and width of 25.4mm. The composite adherends consist of 16 UD-layers of 0.125mm single ply thickness. **Table 3-3** lists the four different layups investigated with their correspondent longitudinal bending stiffness. The reference fuselage panel is represented by the quasi-isotropic (QI) stacking sequence $[(45/90/-45/0)_2]_s$, with 45° as the outermost layer in contact with the adhesive. The two other configurations are also quasi-isotropic, with 90° and 0° as the outermost layer, respectively. By comparing these three layups, the effect of the fibre angle in contact with the adhesive layer will be studied. The fourth configuration maintains the outer layer of 45° as in the reference but with higher number of 0° layers. In this way, a comparison with the reference layup will show the effect of increasing the longitudinal bending stiffness without changing the fibre angle in contact with the adhesive layer (45° on both).

Stacking sequence	Equivalent longitudinal bending stiffness
$[(45/90/-45/0)_2]_s$	39.6GPa
$[(90/45/0/-45)_2]_s$	46.0GPa
$[(0/45/90/-45)_2]_s$	72.4GPa
$[(45/0/-45/0)_2]_s$	69.4GPa

Table 3-3: Layup configurations

The longitudinal bending stiffness was determined based on the classical laminate theory (CLT) as the flexural engineering constant of a laminate given by

$$E_x^f = \frac{12}{D_{11}^* t^3} \qquad (3\text{-}1)$$

for symmetric layups, where D^*_{11} is the corresponding first row/first column entry of the resulting inverse of the bending stiffness matrix, t is the overall laminate thickness of 2mm and x corresponds to the direction along the SLJ-length (longitudinal direction) [3-11].

3.2.3 Laminating process

The adherends were laminated in a Prepreg hand layup process, with 20min of debulking at an under pressure lower than 100mbar in between every fourth layer. All laminates were cured in the same cycle, packed between a base and a caul plate from aluminium. *Fiberflon® 408.07-P* Polytetrafluoroethylene (PTFE) coated glass fabric was used in the laminate surface to be bonded instead of conventional silicone coated peel ply. This is in accordance with the recommendation from literature, in which the PTFE-coated fabric was the only peel ply out of five tested that obtained good adhesion after peel ply removal [3-12]. The autoclave curing cycle for the *Hexply® F6376C-HTS (12K)-5-35%* Prepreg laminate was at 180°C and 9bar gauge pressure for 120min time. The setup resulted in plates with a roughness of 60µm average depth on both surfaces. This roughness has been measured using an *OLYMPUS LEXT OLS3100* confocal laser scanning microscope, on a remaining piece of one of the original Prepreg plates. The measurement was performed at the outside of the plate, within the last ca. 50mm from the edge of the plate. It was ensured that the focus of the laser scan was not chosen too close to the edge of the specimen, where apparent delamination due to rough mechanical trimming may give a misleading result.

3.2.4 Surface treatment

A suitable surface treatment prior to bonding was chosen as combination of degreasing the surface with Acetone and ultra violet (UV) ozone treatment. The UV/Ozone treatment is a physical treatment consisting of the application of high intensity ultra violet light in the presence of ozone gas to both clean and modify the surface of the specimen on a molecular level. This treatment is effective for the removal of organic contaminants. The process works by decomposing the organic compounds into volatile substances (i.e. water and carbon dioxide) with the use of ultraviolet rays (important wave lengths for this process are 184.9nm to 253.7nm) and by strong oxidations during the formation and decomposition of the ozone [3-13, 3-14]. However, the use of UV/ozone is ineffective for removing inorganic contaminants. Therefore, the surface was previously cleaned with acetone, to remove the bulk of organic contaminants and the inorganic surface contaminants that may be present. The UV/ozone treatment was applied for 7min, with the UV-light tubes distancing 40mm from the specimen surface. Bonding the adherends was performed within 30min after the application of the surface treatment. This procedure was performed according to previous studies that showed good CFRP-surface wettability after applying the same method [3-15].

3.2.5 Bonding process

The adhesive bonding process was performed by laying the uncured film adhesive onto the cured adherends and arranging a vacuum setup around them.
Figure 3-1 shows the dimensions of the SLJs and a picture of the final specimens. The SLJs dimensions are in accordance with standard *ASTM D 5868-01* [3-10].

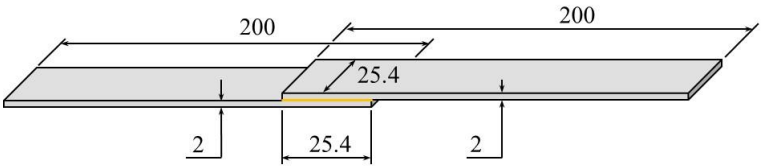

a) SLJ specimen design (dimensions in mm)

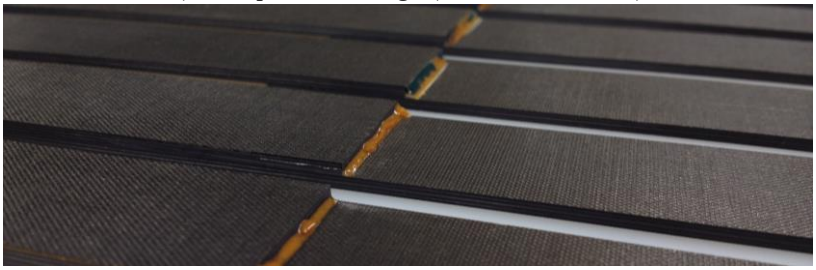

b) Picture of the specimens

Figure 3-1: Single Lap bonded Joints

Excess adhesive gathered at the bond line tips and formed a small fillet at the edges - **Figure 3-1** b). The curing process was performed in an autoclave at 2bar gauge pressure and 177°C curing temperature for 120min dwell time.

3.2.6 Bond line thickness

After bonding, the adhesive thickness of each specimen was measured by taking from the total overlap thickness, the total thickness of both CFRP-adherends. All thickness values throughout this thesis were consistently measured with a digital micrometer with an accuracy of 1µm, while the overlap length was measured with a digital calliper of accuracy 10µm. The use of a micrometer was preferred over a microscope, as multiple measurements could be taken from random spots of the specimen, while only the outside cross-section of the overlap can be measured with microscope, unless performing multiple cuts, which results in loss of samples before testing. Note that the thickness of the adhesive was thereby indirectly derived from measuring the total thickness overlap thickness, which takes into account two uncertainties: The thickness variation of the adherend and the thickness variation of adhesive. From thickness measurements of the adherends alone, it was found a variation of ± 20µm, resulting from an uneven layup. This turned out to be lower than the variation inside the adhesive, which results from misalignment in the bonding jig.

The final adhesive thickness was significantly smaller than the recommended value between 150µm and 200µm, according to the material datasheet, revealing a mean value of 44 ± 47µm. Adhesive flow out due to over pressure in the curing phase would be a possible explanation. However, lots of care has been taken by adjusting the adhesive bonding cycle. After a series of curing pre-trials, both with different temperature and pressure values, as well as after contacting the manufacturer about this issue, a cycle of 120min steady hold at 177°C at a relative over

pressure of 2bar (= 3bar absolute) was identified as best compromise for excess squeeze out versus the prevention of voids. It is therefore believed, that the significant roughness of both adherend surfaces (60µm), adjacent to the bond line, may have soaked a major portion of the adhesive material into their cavities and caused the reduced bond line thickness.

3.3 EXPERIMENTAL SETUP

3.3.1 Surface analysis

A surface analysis using contact angle measurements was performed to the treated CFRP-surfaces to assess their wettability. The contact angle of a 4µl distilled water drop was measured for the rough specimen surface, having a topology imprint from the PTFE/glass fabric with 60µm surface roughness, using the *TECHNEX Cam200/Attension Theta V4.1.9.8* system.

3.3.2 Quasi-static lap shear test

Five specimens per layup configuration were subject to quasi-static tensile loading in accordance to *ASTM D 5868-01* [3-10]. The tests were displacement controlled with a constant displacement rate of 1.3mm/min. They were performed on a *ZWICK-ROELL AllroundLine Z250 SW* testing machine with a load cell of 250kN.

Figure 3-2 illustrates a schematic representation of the test setup. The specimen was hold by two clamps at 250bar hydraulic pressure. The initial distance of the clamps was set at 200mm, with a misalignment of 2mm to counterbalance the overlap offset. A mechanical extensometer, *BTC-EXMACRO.H02* by *ZWICK-ROELL/testXpert II*, captured the elongation between two points of 60mm distance, adjacent to the overlap area. Additionally, the strain field of the overlap area was monitored using digital image correlation (DIC) technique. For this, the *VIC-3D™* system by *CORRELATED SOLUTIONS*, Inc. was used at a 2 Hz frame capture speed. In order to monitor the damage initiation of the specimens, an Acoustic Emission (AE) system by VALLEN *Systeme GmbH* was employed, consisting of two *VS900-M* sensors, which were attached onto the same side of the specimen at ± 42.5mm from the overlap centre and connected to the *AEP4H 34dB* amplifier.

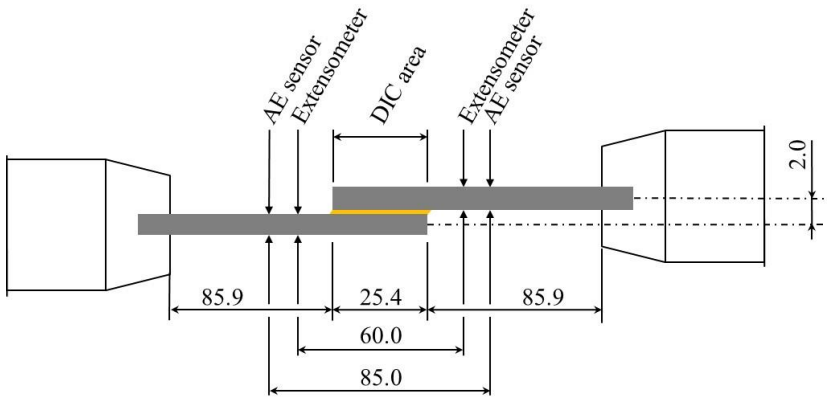

Figure 3-2: Test setup for static tensile loading (dimensions in mm)

3.4 NUMERICAL ANALYSIS

A finite element analysis (FEA) was performed with the commercial software *ABAQUS V6.14-1*. The purpose of the FEA was to numerically simulate the SLJ under tensile loading. An implementation into a 3D-model gives insight into the stress field around the bond line, aiming to interpret the resulting failure mechanisms. The composite was modelled as linear elastic, based on the properties listed in **Table 3-1** while the adhesive was modelled linear-elastic/plastic, using those values from **Table 3-2**. Within this study, there are no plasticity model nor yield criteria used. The material is modelled as elastic-plastic, with 4 data points defining the stress-strain curve in the plastic regime, including isotropic hardening. The load was applied in a single step with 6 load increments taking into account non-linear geometry effects.

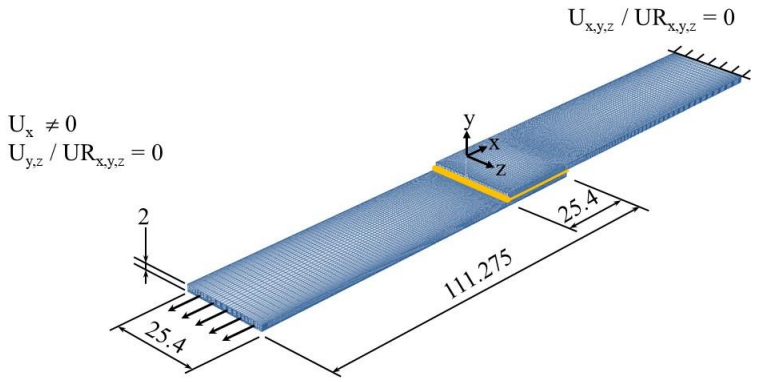

Figure 3-3: 3D FE-model between the clamps with specimen dimensions and boundary conditions (dimensions in mm)

3.4.1 Boundary conditions

The specimen between the clamps was simulated using solid 3D-elements.
Figure 3-3 illustrates the model, including dimensions, boundary conditions and mesh. At the right side all 3 Degrees of Freedom (DoF) are fixed, while on the left side, solely longitudinal displacement is allowed (x-direction). Although the average bond line thickness in the real specimens was 44µm (+- 47µm), it was decided to model the bond line thickness as 62.5µm. This value is the upper limit of the adhesive thickness measured at the real specimens instead of the average bond line thickness and it was considered to be a good compromise between real specimen dimensions and being numerically feasible.

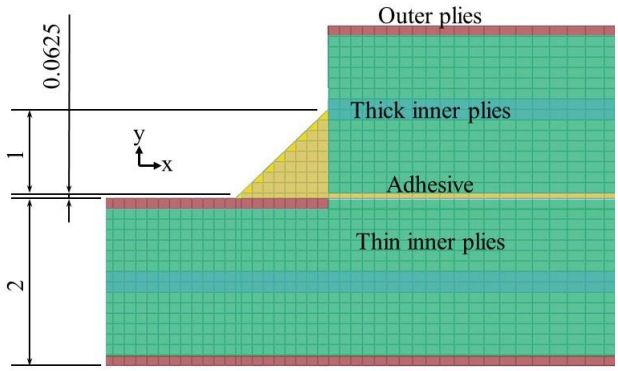

Figure 3-4: Zoom on fillet region and material section assignments (dimensions in mm)

In **Figure 3-4** the region around the left overlap edge is illustrated. The spew fillet design is thereby an approximation of its experimental counterpart. All 4 times 5 specimens of this study had a spew fillet shape similar to a 45° triangle. In fact, the shape was in 16 cases rather convex, and in 4 cases concave. For 8 specimens, the height of the spew fillet reached all the way up to the top of the adherends, while in the remaining cases developing less volume. However, in all cases, the spew fillet reached at least up to half of the height of the adherend (= 1mm).
The fillet shape of the specimens was thereby captured visually prior to testing. The shape was not consistent amongst different specimens and in some cases not even throughout the width of one specimen.
Figure 3-1 gives a general impression of the spew fillet shape. Based on the rather arbitrary result of visual inspection, a compromise needed to be found to not over- or underrepresent the geometry in FEM. A sensitivity study was performed in **Figure 3-5** on peel stress over bond line length with different triangle sizes, concluding that a half adherend height was a suitable choice. This design choice is rather conservative, compared to the spew fillet shape of the actual specimens.

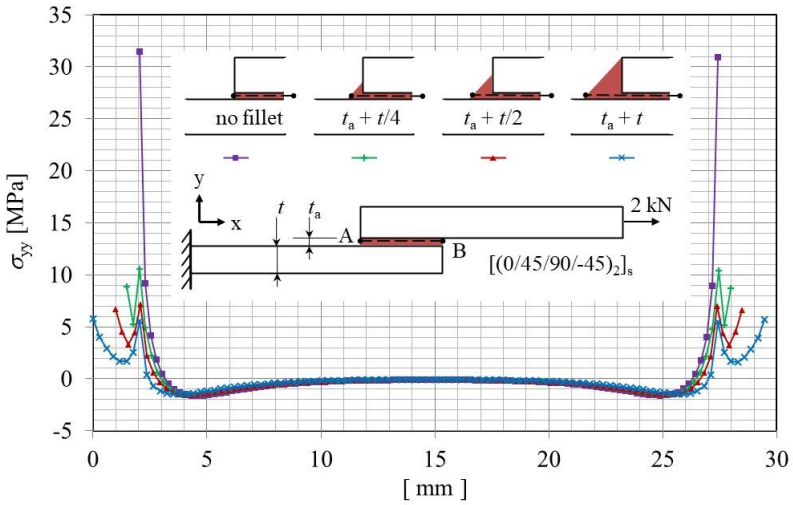

Figure 3-5: Peel stress over bond line length with different triangle sizes

Each composite adherend was modelled with 16 elements through the total thickness of 2mm, which corresponds to one element per single UD-layer of 125µm. Amongst different element types, offered by *ABAQUS V6.14-1 Implicit*, the linear 3D-continuum element with 8 nodes (*C3D8*) was selected for a feasible numerical accuracy versus computational cost for the specific boundary conditions and dimensions of the SLJ-design. The mesh density of the model was refined along the overlap length of the joint to gain numerical accuracy at regions with stress concentrations.

3.4.2 Mesh convergence study

A mesh convergence study was performed in order to guarantee that the results were mesh independent. In **Figure 3-6**, the peel stress (σ_{yy}) is plotted along the overlap length, from left to right, including the length of both fillets in **Figure 3-6** a), and through the thickness of the overlap left edge, from bottom to top in **Figure 3-6** b). Both paths are situated in the centre of the joint in width direction. In order to avoid stress singularities at any interface, the path in **Figure 3-6** a) was chosen exactly in the middle of the bond line and in **Figure 3-6** b) 31.25µm inwards of the overlap end (in x-direction). The length and height of one element in this overlap tip region was set to 125µm, so that the path was plotted at ½ of an element thickness in **Figure 3-6** a) and at ¼ of an element length in **Figure 3-6** b). The dimensions of Mesh 1 in **Figure 3-6** a) were based on the smallest element size at the bond line region with the dimensions length = 125µm, height = 62.5µm, width = 500µm, leading to 688,296 elements in total. A mesh refinement was performed, increasing the number of elements in the overlap region and leading to a total number of 732,054 (Mesh 2). A sufficient convergence in stress values could be established with the coarser Mesh 1 of 688,296 elements of type *C3D8*. All the results presented

in this paper are therefore based on Mesh 1.

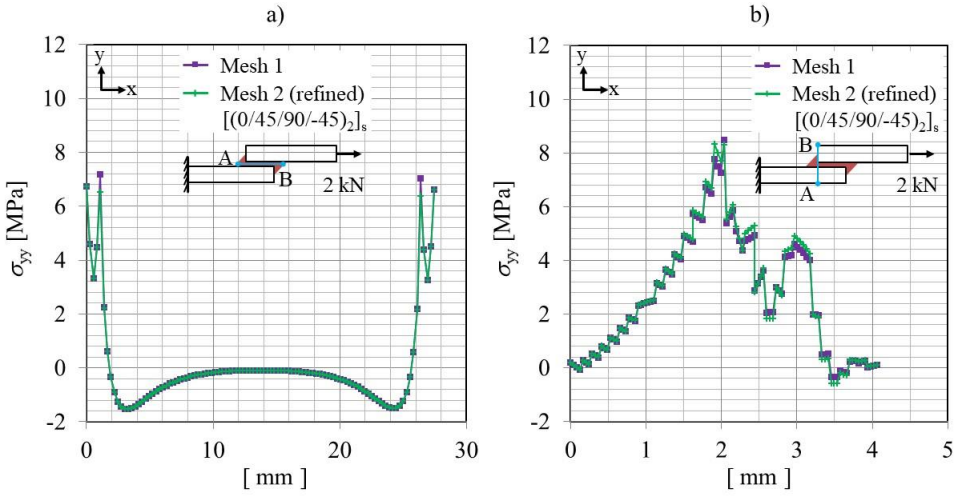

Figure 3-6: Mesh convergence study on peel stress distribution a) along overlap length, b) through overlap thickness

3.5 EXPERIMENTAL RESULTS

3.5.1 Surface analysis

A combined surface treatment of Acetone degreasing and exposure to UV-light in an ozone-containing atmosphere reduced the value of the contact angle by 43%, from 59° (± 19°), before treatment to 34° (± 6°), after treatment. This value is in accordance with literature and corresponds to a good wettability of the surface [3-15].

3.5.2 Quasi-static lap shear test

Figure 3-7 and **Table 3-4** present typical load displacement curves for each configuration as well as the average lap shear strength (σ_{LSS}) with standard deviation, derived from the maximum load divided by the overlap area. The displacement depicted in the graph was derived from the mechanical extensometer shown in **Figure 3-2**. QI-layups with 45° and 90° as outermost ply show no appreciable difference in average lap shear strength, while a 0°-layer outside $[(0/45/90/-45)_2]_s$ and the configuration with increased longitudinal bending stiffness $[(45/0/-45/0)_2]_s$ have significantly higher values of average lap shear strength. The 0°-outside configuration shows 46% and the stiffened configuration 98% increase in average lap shear strength in comparison with the reference layup $[(45/90/-45/0)_2]_s$.

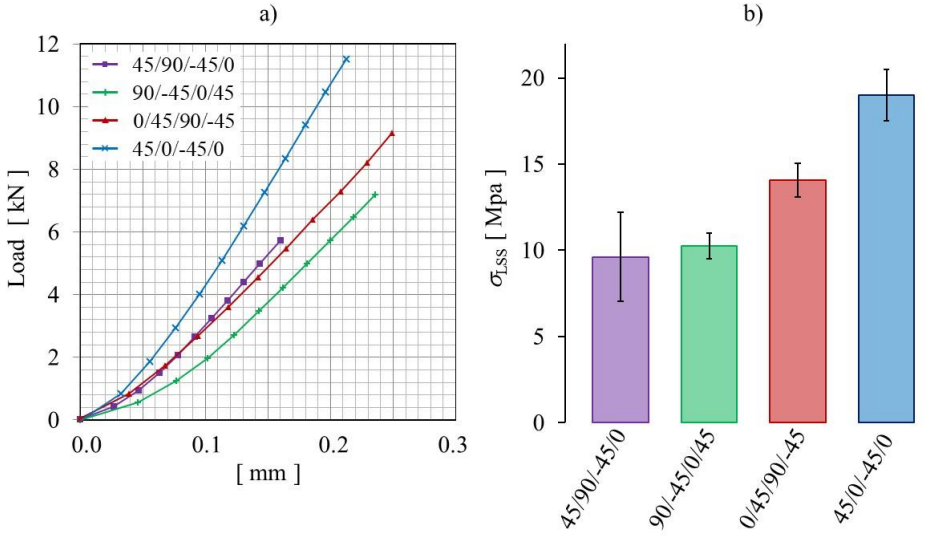

Figure 3-7: a) Load-displacement curves, b) average lap shear strength and corresponding standard deviation for different layups

Layup	$[(45/90/-45/0)_2]_s$	$[(90/-45/0/45)_2]_s$	$[(0/45/90/-45)_2]_s$	$[(45/0/-45/0)_2]_s$
σ_{LSS} [MPa]	9.6 (± 2.5)	10.3 (± 0.8)	14.1 (± 1.0)	19.0 (± 1.5)

Table 3-4: Average lap shear strength, σ_{LSS} (± standard deviation) for different layup configurations

For all specimen there is a noticeable non-linearity of the load-displacement curve until approximately 0.1mm of displacement. It is believed that this trend is caused by initial slack in the testing rig at the beginning of the test. When comparing the stiffness of the different load-displacement curves, layup $[(45/0/-45/0)_2]_s$ shows the steepest slope. This is in agreement with a high longitudinal bending stiffness of the adherend – see **Table 3-3**. However, this correlation does not specifically apply to the other three layups, which show almost the same slope. For example, layup $[(0/45/90/-45)_2]_s$ has a 83% higher longitudinal bending stiffness compared to $[(45/90/-45/0)_2]_s$, while the joint stiffness is similar between the two.

So, in this comparison, the (overall tensile) joint stiffness, given by load over displacement on the tensile machine (measured with extensometer) seems to be not affected by the difference in longitudinal bending stiffness of the CFRP adherends, which is a theoretically calculated value with CLT based on ideal geometry and perfectly flat laminae. In a tensile test, the in-plane stiffness of the adherends should actually play a more important role in the elastic response of the joints. Hence, it is not surprising that the $[(45/0/-45/0)_2]_s$ configuration exhibits higher

stiffness than the remaining ones. The difference among the other 3 configurations (same in-plane stiffness) is actually more surprising, certainly being - at least partially - explained by the different bending stiffnesses.

3.5.3 Final fracture surfaces

In **Figure 3-8**, the typical fracture surfaces for each layup configuration are illustrated. In **Figure 3-8** c) specimens with the ply angle of 0° adjacent to the bond line failed mostly in the bond line with limited damage on the composite adherends (intra-laminar failure of the 0°-ply). The final fracture surface shows cohesive failure, with yellow shades on either of the adherends fracture surfaces, as well as failure near one of the interfaces, being observed as black surfaces, and switching from one side to the other around the center of the bond line. This failure mode was consistent for all specimens. When the fibre angle of the outermost layer was turned away from 0°, the crack path tended to change from within the bond line into the composite. For the extreme case of a 90° ply angle adjacent to the bond line, the joint failed entirely inside the composite, this being consistent for all specimen – see **Figure 3-8** b). The crack propagated deep into the composite up to the third layer away from the bond line.

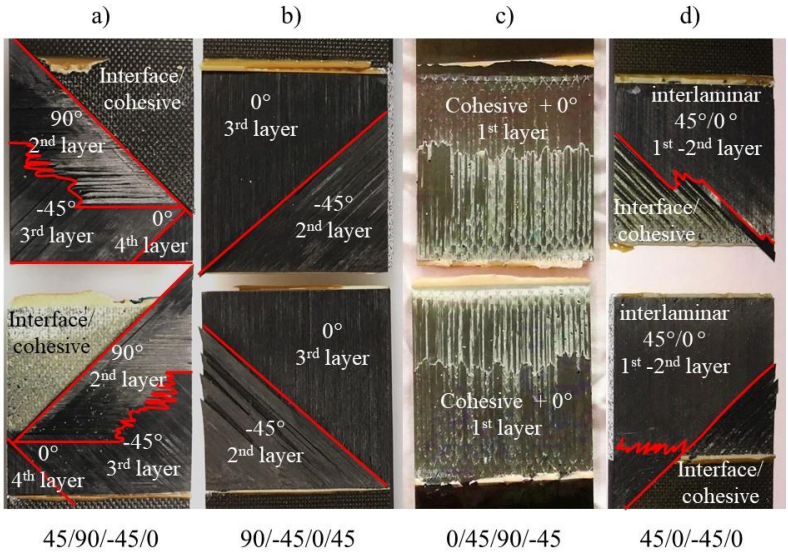

Figure 3-8: Typical fracture surfaces for each layup configuration

For the remaining two configurations with 45° as outside layer, there was a mixed failure mode between the bond line close to the interfaces and failure inside the composite. In case of the reference configuration $[(45/90/-45/0)_2]_s$ in **Figure 3-8** a), the crack propagated up to the third layer of the composite (4th layer visible), while in case of $[(45/0/-45/0)_2]_s$ it reached only the interface between first and second layer – see **Figure 3-8** d). However, this result was not

consistent for all 5 specimens in neither of those two configurations. A variation of the area distribution between failure in the adhesive versus failure in the composite, as well as variation in crack depth from 1st up to 4th layer was noticed for the reference layup $[(45/90/-45/0)_2]_s$. The observation matches the larger scatter of measured average lap shear strength in **Figure 3-7** b) for these two configurations. In case of layup $[(45/0/-45/0)_2]_s$, the area distribution between failure in the adhesive versus failure in the composite was similar in all cases, while the crack depth varied between first and second layer, reflecting more homogeneous results. It is also interesting to note that for all configurations, the crack had the tendency to stop propagating inside the composite whenever reaching the first 0°-ply. These observations are in line with Kahn et al. [3-16]. However, Purimpat et al. [3-17] observed intra-laminar failure for the case of $[(0/45/90/-45)_2]_s$ inside the adjacent UD-layer rather than cohesive failure in the adhesive.

3.5.4 Damage initiation

Figure 3-9 and **Table 3-5** present results from AE-monitoring during the tests. In **Figure 3-9** b) the average load for a damage initiation is presented for the four different layup configurations. The values were derived from plotting load versus cumulative acoustic hits of two sensors over time for every specimen. **Figure 3-9** a) shows an example on how these values were derived. The dashed line indicates the load [N] over time [s] and the marked lines represent the cumulative number of acoustic hits over time [s] for one specimen of the layup $[(0/45/90/-45)_2]_s$. A sudden increase of inclination of cumulated hits for both AE-sensors at 53s indicates the event of a damage initiation at 3.5kN for this specimen.

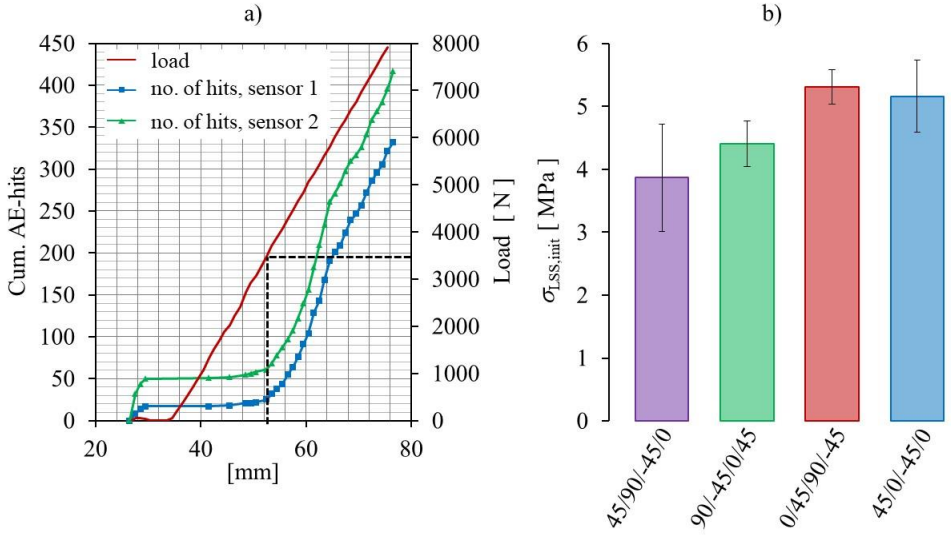

Figure 3-9: a) Cumulative acoustic hits vs. load for $[(0/45/90/-45)_2]_s$, b) average lap shear stress (± standard deviation) at damage initiation of different layups

Layup	$[(45/90/-45/0)_2]_s$	$[(90/-45/0/45)_2]_s$	$[(0/45/90/-45)_2]_s$	$[(45/0/-45/0)_2]_s$
Load [N]	2540 (± 558)	2870 (± 223)	3440 (± 132)	3280 (± 349)
Average lap shear stress [MPa]	3.87 (± 0.86)	4.41 (± 0.37)	5.31 (± 0.27)	5.16 (± 0.57)

Table 3-5: Acoustic Emission results for load and average lap shear stress (± standard deviation) at damage initiation.

3.6 NUMERICAL RESULTS

3.6.1 Model validation

In order to validate the simulations, the strain distribution measured during test by means of DIC is compared with numerical results. **Figure 3-10** shows a representative example of the peel strain distribution along the mid-thickness of the bond line. In width direction, the paths are set along the edge of the bond line, where the strains from the DIC are recorded. The values presented correspond to layup $[(0/45/90/-45)_2]_s$ at a reference load of 2kN. This value was set in order to stay within the area of linear elastic material behaviour before damage initiation.

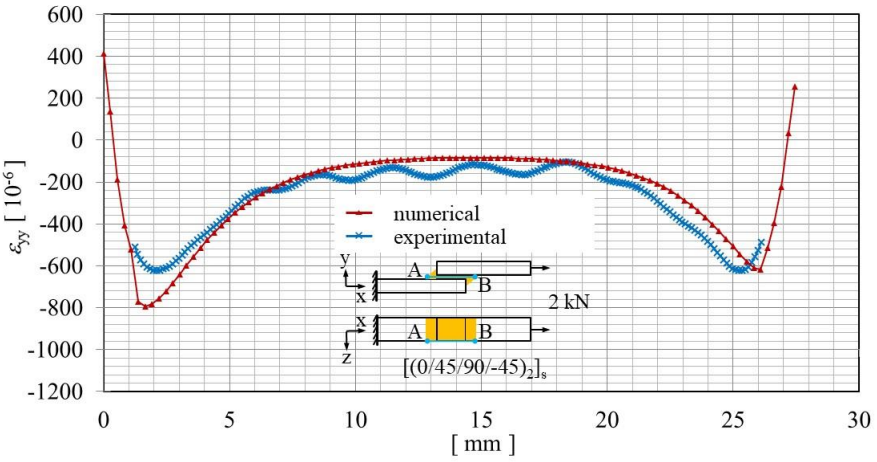

Figure 3-10: Peel strain(ε_{yy}) in microstrain [10^{-6}] along the bond line, numerical versus experimental method

Overall, the numerical analysis predicts well the experimentally measured strain distribution. The deviation is larger at the bond line tips, where the strains are higher. This might be due to two main reasons: 1) the strain field captured by the camera represents the strain of the colour coating that was applied to provide a contrast rich speckle pattern, as common for DIC systems

and 2) the method to extract strain values via image correlation software *Vic3D 7*, is prone to some inaccuracy when picking the load path, which may not exactly match the ideal location of the numerical model.
Since the model contains a perfectly symmetric layup sequence and the design comprises a point symmetry (in 2D) or line symmetry (in 3D, z-direction) around the center of the overlap region, any stress distribution is expected to be symmetric towards the two overlap tips. However, an asymmetry is pronounced at the edges, where **Figure 3-10** is plotted, and it decreases significantly towards the mid width of the specimen. An experimentally derived asymmetry of the strain field is understandable; but it is not clear what is causing the asymmetry in the FE-model.

3.6.2 Stress analysis

The numerical analysis can be further explored to study the stresses around the overlap region. **Figure 3-11** presents the shear (τ_{xy}) and peel (σ_{yy}) stress distribution along the bond line length for all layup configurations given by the numerical model at a pre-defined load of 2kN, before damage initiation. The plot path is taken at centre position in width direction of the joint and mid-thickness of the bond line.

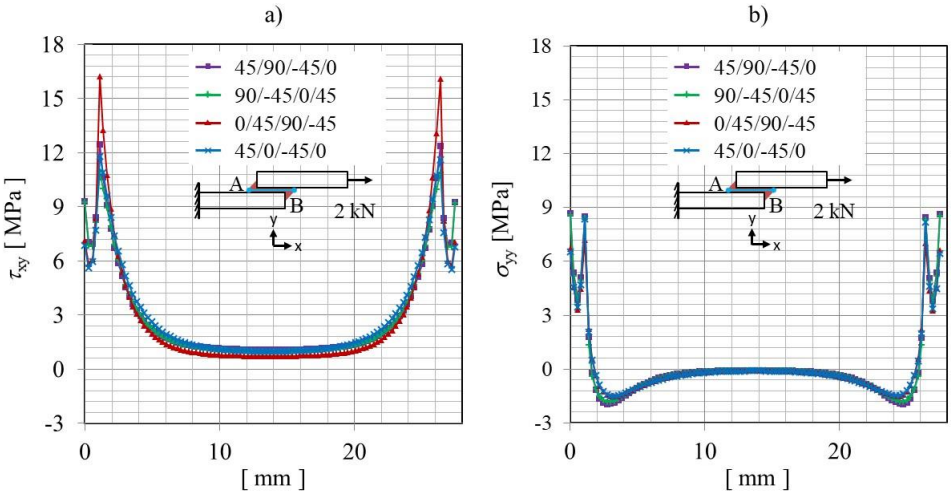

Figure 3-11: a) Shear (τ_{xy}), and b) peel (σ_{yy}), stress along the bond line of the joint at centre position in width

The comparison of the different layups along the overlap length does not show large deviations in stress level. The plots show the characteristic form for shear and peel stress known from analytical solutions [3-18]. Only on the shear stresses at the bond line tips, the differences are more visible. The 0/45/90/45 configuration has larger peak shear stresses close to the overlap

tips and slightly lower at the mid of the overlap. However, plotting shear (τ_{xy}) and peel (σ_{yy}) stress through the thickness of the overlap, reveals more differences between the layups. In **Figure 3-12**, plots are taken at centre position in width and covers the complete overlap thickness of 4.0625mm length from bottom to top. Thereafter in **Figure 3-13**, a closer focus is taken onto the near region around the adhesive bond line.

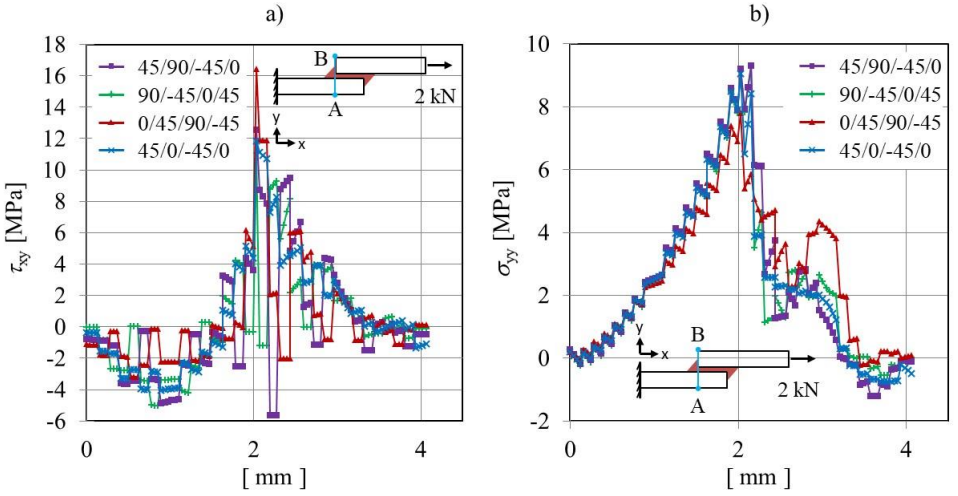

Figure 3-12: Shear (τ_{xy}), a) and and peel (σ_{yy}), b) stress through the overlap thickness at centre position in width

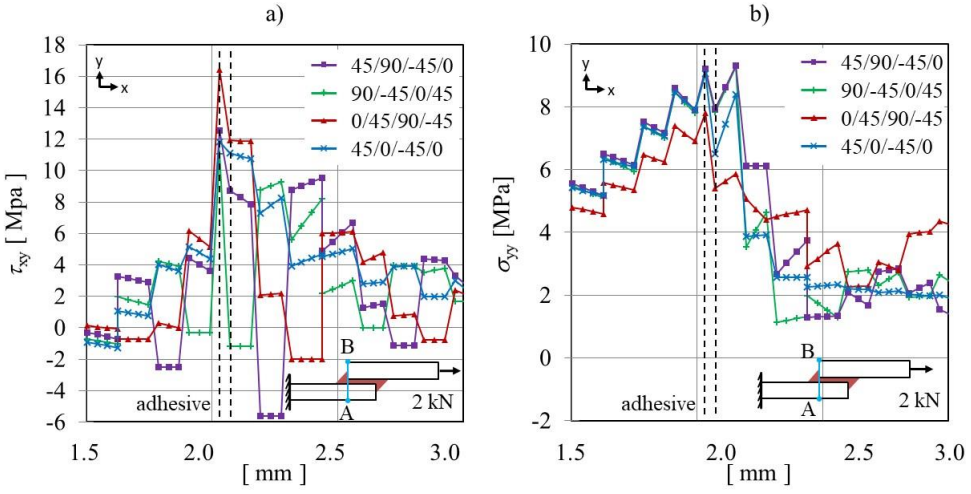

Figure 3-13: Shear (τ_{xy}), a) and and peel (σ_{yy}), b) stress through the overlap thickness at centre position in width, focussed region around the bond line

Both stresses contain fairly rough jumps in stress loads at the interfaces between adjacent UD-layers. The peak stresses are in the centre of the plot at the location of the adhesive. There are two interesting findings when analysing these plots: Firstly, when looking into the values for layup $[(0/45/90/-45)_2]_s$ (red line, triangular marker) around the adhesive region, this layup has the highest shear stress value inside the bond line in **Figure 3-13** a) and at the same time the lowest peel stress, in **Figure 3-13** b). Thus, the ply angle of 0° adjacent to the bond line affects the stress distribution in such a way that the loads are carried mainly by the adhesive layer in shear. The corresponding peel stresses at the adhesive as well as inside the composite laminates are lower for this configuration in comparison with all other configurations – see **Figure 3-13** b). Interestingly, the 0°–outermost configuration is related to mostly cohesive failure, rather than failure inside the composite. This failure pattern fits well with the stress comparison shown in **Figure 3-13**, meaning lower out-of-plane stresses in the composite laminate and higher shear stresses in the adhesive, hence failure mainly in the adhesive. Secondly, the peel stress plots on the right are more consistent for the different layup configurations, while the shear stress distribution on the left differs more significantly. As peel stresses are out-of-plane, the ply angle does not have a large influence on the peel stress distribution. Therefore, a 0° can carry the same amount of peel stresses as the 45° or 90° – similar out-of-plane stiffness. Contrary to this, for the shear stresses, as an in-plane stress, the fiber angle has a significant influence on its stress distribution. Therefore, the 90° layers are consistently the ones with the lowest shear stresses for all layup configurations, since they have the lowest in plane stiffness.

3.6.3 Failure analysis

The numerical approach to derive the load at damage initiation was established by post-processing the stress tensor for every node. A set of user-defined subroutines was built to contain various failure criteria. As a result of the *World-Wide Failure Exercise* (WWFE) I and II [3-19 - 3-20], one can find a variety of applicable failure criteria, based on continuum damage mechanics, for composite structures under different two- or three-dimensional stress states. The benchmark results also reveal that not every failure theory can conclusively predict every load case and failure pattern [3-21]. On the other hand, the unsymmetrical 3D-stress state inside a single overlap has not been covered by any of the WWFE test cases. Therefore, to ensure reliable results, it was decided to use several failure criteria for both the composite and the adhesive in order to understand which criterion fits the best to this specific load case. For a failure inside the composite, the *Hashin* [3-22, 3-23], *Puck* [3-24 - 3-26] and a *3D-invariant based* criterion of Camanho et. al. [3-7] were used. All three criteria distinguish between fibre and matrix failure. For the adhesive, the *Mises* and the quadratic *Drucker-Prager* yield criterion were used. In the later, the study follows the approach of da Silva et al. [3-27 - 3-28], where the yield criterion can be expressed as

$$aq^b - p = p_t \quad (3\text{-}2)$$

The terms that appear in Equation (3-2) are defined as

$$a = \frac{1}{3(\beta-1)\sigma_{yt}} \quad (3\text{-}3)$$

$$q = \sqrt{\frac{1}{2}[(\sigma_1-\sigma_2)^2+(\sigma_2-\sigma_3)^2+(\sigma_3-\sigma_1)^2]} \quad (3\text{-}4)$$

$$b = 2$$

$$p = \frac{1}{3}(\sigma_1+\sigma_2+\sigma_3) \quad (3\text{-}5)$$

$$p_t = \frac{\beta\sigma_{yt}}{3(\beta-1)} \quad (3\text{-}6)$$

with b as the exponent parameter, σ_{yt} for the yield stress of the adhesive in tension, β representing the ratio of yield stress in compression to the yield stress in tension and σ_1, σ_2 and σ_3 being the principal stresses at the element nodes. Those stress values were linearly extrapolated from the integration points, according to the given element type *C3D8*. In this study, there were no experimental values available for the compressive yield stress of the chosen adhesive *Hysol® EA 9695™ 050K AERO*. The β-value was chosen 1.45, based on values found in literature for adhesives with comparable Young's modulus and yield strength [3-5, 3-9, 3-27]. An additional sensitivity study was performed, where the suggested value of β from literature was altered by ± 15%, to identify by how much the results are affected by the β-change. As a result, it can be stated that a ± 15% variation of β has in average an effect of ± 10% on the damage initiation load, when using the Drucker-Prager criterion for cohesive failure. It must therefore be noted, that the accuracy of the failure prediction is significantly affected by the chosen input-value for β. The results of the sensitivity study on β-variation can be found in APPENDIX H.

For the failure criteria of the composites, it is important to note that the strength of a single UD-layer inside a stacking sequence varies with respect to its ply thickness and position within the sequence. This in-situ effect was incorporated, following recent work of Camanho et al. [3-29]. The UD-properties in comparison with their elevated in-situ representative are shown in **Table 3-6**.

	UD properties [MPa]		In-situ properties [MPa]	
In-plane shear strength	s_L[a]	104	s_L^{is}	126
Transverse shear strength	s_T[a]	35	s_T^{is}	42
Transverse tensile strength	y_T[a]	102	y_T^{is}	162
Transverse biaxial tensile strength	y_{BT}[b]	63	y_{BT}^{is}	110
Transverse compressive strength	y_C[a]	-255	y_C^{is}	-296

[a] TDS of *F6376 HEXCEL / AIRBUS* [3-6]

[b] adapted from *Hexply-8552/IM7*, Camanho et al. [3-7]

Table 3-6: UD versus in-situ laminate properties

The occurrence of damage initiation was determined, once the specific failure criterion indicates that at least one node reaches failure. Values at which damage initiation is indicated in the numerical model were then compared with the loads indicated by the AE during the experiments. **Figure 3-14** and **Table 3-7** illustrate the comparison of experimental AE-results versus the numerical approach in terms of average lap shear stress at damage initiation.

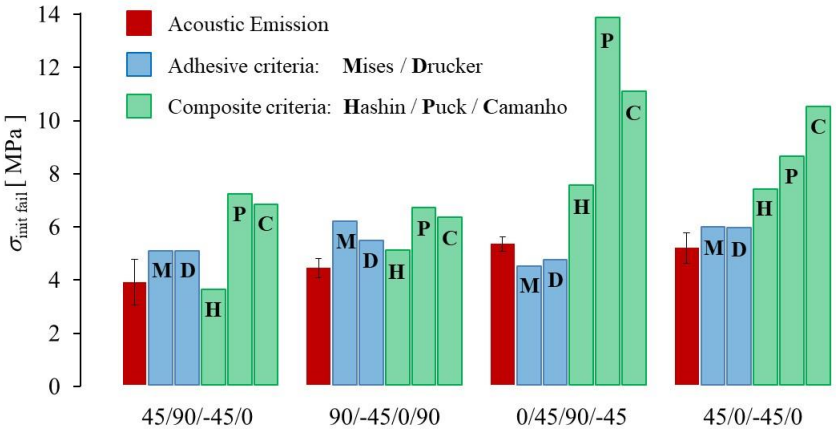

Figure 3-14: Average lap shear stress at damage initiation: experimental versus numerical results

Layup	$[(45/90/-45/0)_2]_s$	$[(90/-45/0/45)_2]_s$	$[(0/45/90/-45)_2]_s$	$[(45/0/-45/0)_2]_s$
σ_{LSS} - EXP	9.6 (±2.6)	10.3 (± 0.7)	14.1 (± 1.0)	19.0 (± 1.5)
σ_{1st_AE} - EXP	3.9 (± 0.9)	4.4 (± 0.4)	5.3 (± 0.3)	5.2 (± 0.6)
σ_{1st_Mises} - NUM	5.1	6.2	4.5	5.9
$\sigma_{1st\_Drucker}$- NUM	5.1	5.4	4.8	5.9
σ_{1st_Hashin}- NUM	3.6	5.9	7.5	7.4
σ_{1st_Puck}- NUM	7.2	6.7	13.8	8.6
$\sigma_{1st\_Camanho}$- NUM	6.8	6.3	11.6	10.5

Table 3-7: Average lap shear strength (± standard deviation) versus stress at damage initiation: Experimental (EXP) and numerical (NUM) approach with values in [MPa]

Considering the mechanical behaviour of single lap joints under tension [3-2, 3-18] and looking to the failure modes presented in **Figure 3-8**, matrix tensile failure is the dominant failure mode within the composite laminate. After the index values for all different failure modes were checked, matrix tension values were identified as most critical. Hence the index values, presented in **Figure 3-14** and **Table 3-7**, solely represent this case. For the first two laminates, $[(45/90/-45/0)_2]_s$ and $[(90/-45/0/45)_2]_s$ the criteria indicate failure within adhesive and in the composite at loads close to the experimental results. There is a tendency though, that in both layups the damage initiates inside the adhesive (except for the *Hashin* criterion). For the two

stronger layups, $[(0/45/90/-45)_2]_s$ and $[(45/0/-45/0)_2]_s$, damage initiation at the composite adherents is generally indicated at significantly higher loads than for the adhesive. The adhesive failure criteria are in overall agreement with the experimental results. For all four layups, damage initiation tends to appear in the adhesive. However the loads of failure initiation of the adhesive and of the composite tend to get closer for the configuration of $[(90/-45/0/45)_2]_s$ and further away for the $[(0/45/90/-45)_2]_s$. The fact that the load for damage initiation in the composite is significantly higher than in the adhesive for the layups $[(0/45/90/-45)_2]_s$ and $[(45/0/-45/0)_2]_s$, in comparison with the layups $[(45/90/-45/0)_2]_s$ and $[(90/-45/0/45)_2]_s$, shows that a crack is less likely to grow inside the composite in the two former layups than in the two later layups. This is very much in agreement with the fracture surfaces presented in **Figure 3-8**, since for the layups $[(45/90/-45/0)_2]_s$ and $[(90/-45/0/45)_2]_s$ the damage grows further inside the composite than for the layups $[(0/45/90/-45)_2]_s$ and $[(45/0/-45/0)_2]_s$. Layups $[(0/45/90/-45)_2]_s$ and $[(45/0/-45/0)_2]_s$ show a larger scatter between the composite criteria with no visible trend. The failure indices for the *Puck* and *3D-invariant based* criteria include the in-situ effect for material allowable, whereas the original UD-properties were used for the *Hashin* criterion. With respect to the SLJ-design and materials depicted by this study, there is no clear tendency which of the composite criteria is more applicable, since there is no general trend for all layups studied, whereas both criteria for failure inside the adhesive, *Mises* and *Drucker-Prager*, indicate similar values that match well with the experimentally observed.

As earlier in **section 3.2.1**, it must be stated that the value of transverse tensile strength Y_T, as provided by the TDS of *Hexply® F6376C-HTS (12K)-5-35%*, *HEXCEL / AIRBUS* [3-6], seems arguably high, compared to typical values for state-of-the-art, thermoplastic-toughened systems, such as Hexply M21E, reach about 80MPa [3-8]. The additional material test according to *ASTM-D3039-14* in **APPENDIX G** confirms a value of 104 MPa, which is in agreement with the value of the provided datasheet. **Figure 3-15** illustrates the location of failure according to each criterion. The location was determined from the node coordinates given by the *ABAQUS* input-file. All criteria consistently indicate failure in the region around the bond line tip of the non-free adherend side. The location may arbitrarily switch from the left to the right tip since stresses are fairly similar in both overlap tips. Looking through the thickness of the overlap, the adhesive tends to fail at the interface with the first UD-layer for all layups. In case of composite failure, the location differs. Depending on the layup, failure in the composite tends to initiate at the interface of that UD-layer with the lowest longitudinal bending stiffness, meaning near the 90°-layer. This result does generally correspond to the observations of fracture surfaces in **Figure 3-8**. However, the final fracture surface at maximum load is a different state and cannot be taken as direct guideline to predict an initial failure mechanism.

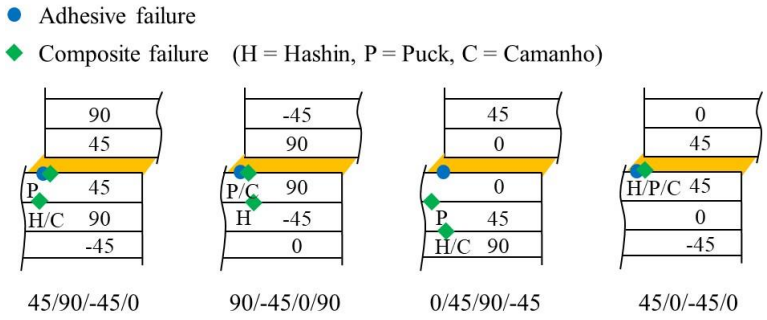

Figure 3-15: Location of damage initiation due to FEA

3.7 DISCUSSION

Figure 3-16 summarizes the experimental results. It presents the average lap shear strength (σ_{LSS}, based on the maximum load), the AE-based average lap-shear stress at damage initiation (σ_{init}), the final fracture surfaces and the equivalent longitudinal bending stiffness for all configurations. QI-layups with 45° and 90° as outermost ply show similar average lap shear strength, while a 0°-layer outside and the configuration with increased longitudinal bending stiffness have significantly higher values. The AE-based stresses, where damage initiation is estimated, are significantly lower (less than 50%) than average lap shear strength (σ_{LSS}) in all cases. This difference indicates that there is still a remarkable portion of residual tensile strength for composite bonded joints after damage initiation.

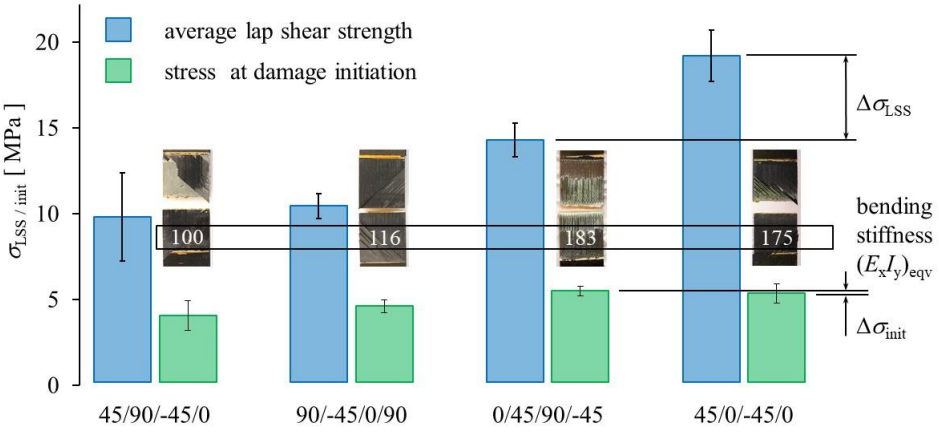

Figure 3-16: Average lap shear strength (± standard deviation) at maximum load vs. damage initiation in respect to bending stiffness

3.7.1 Effect of adherend bending stiffness

From the layups investigated, there is clearly two groups in terms of bending stiffness of the laminate adherends: the group with lower bending stiffness, the first two layups $[(45/90/-45/0)_2]_s$ and $[(90/-45/0/90)_2]_s$, and the group with higher bending stiffness, the two last layups $[(45/0/-45/0)_2]_s$ and $[(0/-45/90/45)_2]_s$. In terms of damage initiation, these groups can be distinguished as: lower stiffness leads to lower loads at damage initiation and vice versa, which has been observed both experimentally and numerically. Numerical simulations indicate that there is a tendency for damage to initiate in the adhesive bond line. This is in fact in accordance with earlier studies [3-18, 3-30, 3-31], correlating strength of SLJs only to the stress analysis and adhesive failure. However, when we look to the maximum load carried by the joints, by means of average lap shear strength, this trend does not entirely apply. It is noticeable that the layups $[(45/0/-45/0)_2]_s$ and $[(0/-45/90/45)_2]_s$, with similar bending stiffness, have similar loads at damage initiation but a difference of 35% in average lap shear strength (σ_{LSS}). This means that for the same bending stiffness if changing the stacking sequence such that the final failure progresses inside the composite adherend, i.e., from $[(0/-45/90/45)_2]_s$ - damage inside the adhesive to $[(45/0/-45/0)_2]_s$ - damage inside the composite, the average lap shear strength increases.

Taking into account the relative bending stiffness of each layup configuration, it can then be concluded that increasing the bending stiffness leads to an increase of the joint strength associated with damage initiation. After crack initiation, damage progression inside the composite yields to higher ultimate failure load than one inside the adhesive. This conclusion draws the limits of previous recommendations made in literature to increase bending stiffness to increase joint strength up to damage initiation. If the aim is to increase the maximum lap shear strength at failure, this recommendation is no longer valid.

3.7.2 Effect of outermost ply angle

Based on the observations of the fracture surfaces, the final failure mode is influenced by the orientation of the outermost lamina, in such a way that a 0°-ply in contact with the adhesive will favour failure inside the adhesive and larger angles will favour failure to grow inside the composite. This is in agreement with previous work of Aydin [3-30], Khan et al. [3-16], and Purimpat et al. [3-17] and can be explained with the peel stress (σ_{yy}) and shear stress (τ_{xy}) distribution through the overlap thickness shown in **Figure 3-12** and **Figure 3-13**. Now, the question can be replied, why the appearance of a 0°-ply orientation always prevents a crack to grow further into the composite. On one hand, layup $[(0/-45/90/45)_2]_s$ has the highest shear stress level inside the bond line, with a distinct drop towards the adherends. In addition, this layup has the lowest peak stress in peel at the adhesive, again with a rapid decrease towards the composite. Stresses are focussed on the very narrow area of the bond line and drop significantly when reaching the composite adherend. This results in the joint to fail cohesively inside the adhesive. On the other hand, for the remaining configurations with larger ply-angles in contact with the adhesive, the peel stresses are high in the adhesive and in the composite adherend. This favours

failure to propagated inside the composite, as observed in the final fracture surfaces.
The results shown in **Figure 3-7** and **Figure 3-8** indicate that, cohesive failure does not necessarily lead to the higher lap shear strength at final failure than failure inside the composite. In fact for laminates with similar bending stiffness, such as $[(45/0/-45/0)_2]_s$ and $[(0/-45/90/45)_2]_s$, a failure inside the composite in the former leads to higher lap shear strength than cohesive failure inside the adhesive. It can be concluded that, for the same bending stiffness, larger ply-angles in contact with the adhesive will increase the lap shear strength of the SLJ at final failure. These results are in agreement with the previous of work of Purimpat et al. [3-17]. However, they are both in disagreement with the previous work of Khan et al [3-16] where is concluded, that highest maximum load at quasi-static testing is reached by the configuration with cohesive failure inside the adhesive. As there were not the exact same layup configurations investigated, results may differ. In addition, the morphology of UD 0° plies - with the fibres aligned with the crack growth direction - means that crack migration towards inside the adherend would require fibre fracture, as opposed to UD off-axis plies, where fracture can migrate towards inside the adherend through matrix cracking. This is also an important aspect that should not be neglected.

3.8 CONCLUSION

This study aims to understand the effect of the composite layup on the damage initiation and final failure of composite bonded single lap joints under quasi-static tensile loading. Four different configurations were studied, with the quasi-isotropic stacking sequence $[(45/90/-45/0)_2]_s$ as the reference layup. Three other layups ($[(90/-45/0/45)_2]_s$, $[(0/-45/90/45)_2]_s$ and $[(45/0/-45/0)_2]_s$) were tested in which the angle of the layer in contact with the adhesive ($[(90/-45/0/45)_2]_s$, $[(0/-45/90/45)_2]_s$) and the longitudinal bending stiffness of the adherends ($[(45/0/-45/0)_2]_s$) were varied. Tests were monitored to identify damage initiation loads, as well as maximum loads. FE-analysis were performed to numerically simulate the experimental tests up to damage initiation. From the analysis of the results the following conclusions can be drawn:

- An increase of the in-plane longitudinal bending stiffness of the laminate adherends postpones damage initiation. For all layup configurations, damage tends to initiate in the bond line and, therefore, a stiffer laminate decreases the stress field in the bond line region and increases the load up to damage initiation. However, this relation between stiffness and strength is no longer valid on maximum lap shear strength at failure load.
- The damage progression is influenced by the orientation of the outermost lamina such that, a fiber orientation towards 0° causes the crack to propagate cohesively within the adhesive bond line while as the ply angle increases, the crack tends to propagate further inside the composite. This is related with the fact that, a layup with 0° adjacent to the adhesive interface leads to an increase in the shear stresses inside the adhesive but lower peel stresses inside the composite layup, while a layup with larger ply angles in contact with the adhesive increases the peel stresses in the adhesive and in the neighbouring composite layup.

- The ply angle has a larger influence on the (in-plane) shear stresses than on the (out-of-plane) peel stresses.
- For similar adherend bending stiffness, larger ply-angles in contact with the adhesive will increase the lap shear strength of the SLJ at final failure, because they promote crack propagation inside the composite rather than inside the adhesive.
- There is a clear distinction between the layup effect properties in the damage initiation and final failure of the SLJ. Therefore, an optimized layup might be very different, if the goal is to postpone damage initiation or final failure.
- Finally, a QI-layup may not be the best choice, in terms of tensile joint strength, based on the linear-elastic approach of this study. The findings of this study could then be the basis for a further optimization process of the layup beyond common ply angles.

REFERENCES

[3-1] J. Kupski, S. Teixeira de Freitas, D. Zarouchas, P. Camanho, R. Benedictus: *Composite layup effect on the failure mechanism of single lap bonded joints.* Journal of Composite Structures, vol. 217, pp. 14-26, 2019

[3-2] E. Godwin, F. Matthews: *Review of the Strength of Joints in Fibre-Reinforced Plastics: Part 2 Adhesively bonded joints*. Composites, vol. 13, no. 1, pp. 29-37, 1982

[3-3] R. Adams: *Strength Predictions for Lap Joints, Especially with Composite Adherends. A Review*. J. Adhesion vol. 30, no. 1-4, pp. 219-242, 1989

[3-4] S. Teixeira de Freitas, J. Sinke: *Adhesion properties of bonded composite-to-Aluminium joints using peel tests*. The Journal of Adhesion, vol. 90, pp. 511-525, 2014

[3-5] S. Teixeira de Freitas, J. Sinke: *Failure analysis of adhesively-bonded skin-to-stiffener joints: Metal–metal vs. composite–metal*. Eng. Failure Analysis, vol. 56, pp. 2-13, 2015

[3-6] Material datasheet: *A75-T-2-0123-1-1*. Airbus Material-Handbook Structure, 2014

[3-7] P. Camanho, A. Arteiro, A. Melro, G. Catalanotti, M. Vogler: *Three-dimensional invariant-based failure criteria for fibre-reinforced composites*. Int. Journal of Solids & Structures, vol. 55, pp. 92-107, 2015

[3-8] W. Liebig, C. Leopold, T. Hobbiebrunken, B. Fiedler: *Newtest approach to determine the transverse tensile strength of CFRP with regard to the size effect.* Composites Communications, vol. 1, pp. 54-59, 2016

[3-9] S. Teixeira de Freitas, J. Sinke: *Failure analysis of adhesively-bonded metal-skin-to-composite-stiffener: Effect of temperature and cyclic loading*. Journal of Composite Structures, vol. 166, pp. 27-37, 2017

[3-10] ASTM D5868 - 01: *Standard Test Method for Lap Shear Adhesion for Fiber Reinforced Plastic (FRP) Bonding*, 2014

[3-11] K. Kaw, *Mechanics of Composite Materials*, Taylor & Francis, Boca Raton, FL, 2nd edition, 2006

[3-12] J. Holtmannspoetter, J. Czarnecki, M. Wetzel, D. Dolderer, C. Eisenschink: *The Use of Peel Ply as a Method to Create Reproduceable But Contaminated Surfaces for Structural Adhesive Bonding of Carbon Fiber Reinforced Plastics*. Journal of Adhesion, vol. 89, no.2, pp. 96-110, 2013

[3-13] *Ultraviolet-Ozone Surface treatment*. Three Bond Technical News, 1987

[3-14] J. Poulis: *Small cylindrical adhesive bonds*. PhD thesis, Technical University Delft, The Netherlands, ISBN-90-370-0082-7, pp. 39-62, 1993

[3-15] S. Teixeira de Freitas, D. Zarouchas, J. Poulis: *The use of acoustic emission and composite peel tests to detect weak adhesion in composite structures*. Journal of Adhesion, vol. 94, pp. 743-766, 2018

[3-16] M. Khan, C. Hamar, G. Aglietti, A. Crocombe, A. Viquerat: *Development of Rules for the Design of Composite Bonded Joints*. 11th European Adhesion Conference, Glasgow, United Kingdom, pp. 331-334, 2016

[3-17] S. Purimpat, R. Shahram, A. Shahram: *Effect of fibre angle orientation on a laminated composite single-lap adhesive joint*. Journal of Advanced. Composite Materials, vol. 22, no. 3, pp. 139-149, 2013

[3-18] L. Hart-Smith: *Adhesive bonded single-lap joints*. Technical report NASA CR 112236, Douglas Aircraft Co., Inc., Long Beach, CA, United States, 1973

[3-19] M. Hinton, A. Kaddour: *The background to the Second World-Wide Failure Exercise*. Journal of Composite Materials, vol. 46, pp. 19-20, 2012

[3-20] M. Hinton, A. Kaddour: *The background to Part B of the Second World-Wide Failure Exercise: Evaluation of theories for predicting failure in polymer composite laminates under three-dimensional states of stress*. Journal of Composite Materials, vol. 47, pp. 6-7, 2013

[3-21] B. van Dongen, A. van Oostrum, D. Zarouchas: *A blended continuum damage and fracture mechanics method for progressive damage analysis of composite structures using XFEM*. Composite Structures, vol. 184, pp. 512-522, 2018.

[3-22] Z. Hashin: *Failure Criteria for Unidirectional Fiber Composites*. Journal of Applied Mechanics, vol. 47, pp. 329-334, 1980

[3-23] G. Kress: *Examination of Hashin's failure criteria for Part B of the second world-wide failure exercise: Comparison with test data*. Journal of Composite Materials, vol. 47, no. 6-7, pp. 867-891, 2013

[3-24] A. Puck, H. Schuermann: *Failure analysis of FRP laminates by means of physically based phenomenological models*. Journal of Composites Science and Technology, vol. 58, pp. 1045-1067, 1998

[3-25] A. Puck, J. Kopp, M. Knops: *Guidelines for the determination of the parameters in Puck's action plane strength criterion*. Journal of Composites Science and Technology, vol. 62, pp. 371–378, 2002

[3-26] M. Deuschle, A. Puck: *Application of the Puck failure theory for fibre-reinforced composites under three-dimensional stress: Comparison with experimental results*. Journal of Composite Materials, vol. 47, no. 6-7, pp. 827–846, 2013

[3-27] L. da Silva, T. Rodrigues, M. Figueiredo, M. de Moura, J. Chousal: *Effect of Adhesive Type and Thickness on the Lap Shear Strength*. Journal of Adhesion, vol. 82, pp. 1091-1115, 2007

[3-28] D. Drucker, W. Prager: *Soil mechanics and plastic analysis or limit design*. Quart. Applied. Mathematics, vol. 10, pp. 157–165, 1952

[3-29] P. Camanho, C. Davila, S. Pinho, L. Iannucci, P. Robinson: *Prediction of in situ strengths and matrix cracking in composites under transverse tension and in-plane shear*. Composites: Part A, vol. 37, pp. 165-176, 2006

[3-30] W. Renton, J. Vinson: *The efficient design of adhesive bonded joints*. J. Adhesion, vol. 7, pp. 175-193, 1975

[3-31] M. Aydin: *3-D Nonlinear Stress Analysis on Adhesively Bonded Single Lap Composite Joints with Different Ply Stacking Sequences*. Journal of Adhesion, vol. 84, pp. 15–36, 2008

4 FROM ORIENTATION TO THICKNESS: HOW THIN PLIES DELAY DAMAGE ONSET IN LAMINATED JOINTS

This chapter is based on the journal article: J. Kupski, D. Zarouchas, S. Teixeira de Freitas: *Thin-plies in adhesively bonded carbon fiber reinforced polymers*. Composites Part B, vol. 181, 2020 [4-1].

4.1 INTRODUCTION

The previous **Chapter 3** showed how a certain stacking sequence can steer the crack to propagate either inside the composite or inside the adhesive and how the position of the outermost 0°-ply plays a crucial role for the type of failure mechanism. An increase in adherend bending stiffness postpones the damage initiation in the joint while the ultimate load is influenced by how the damage progresses. But depending on the designer's preference, the joint may not always be optimized for ultimate load. If a first-ply failure at higher loads is required, the stacking sequence has little influence and other laminate parameters need to be studied.
The review of **Chapter 2** shows that studies have demonstrated how a reduction of ply thickness in composite laminates leads to a delay in damage onset and enhanced ultimate load [4-2, 4-3]. Therefore, the aim of this chapter is to meet the poor out-of-plane strength of the adherends with the application of thin plies. Lap shear specimens with three different ply thicknesses were tested under quasi-static tensile loading. Following the approach of the previous chapter, a combined experimental and numerical approach was used to investigates damage initiation, maximum joint strength and failure mechanism.

4.2 MATERIALS AND SPECIMENS

4.2.1 Materials

The materials used for this study were unidirectional Prepreg tapes from carbon fibres and epoxy resin in combination with an epoxy film adhesive. The Prepreg material was chosen *NTPT-HTS (12K)-5-35%*, which is a thermoplastic-toughened epoxy resin unidirectional (UD) Prepreg system. The adhesive was *Scotch-Weld™ AF 163-2K* in 293g/m^2 areal weight, including a knit supporting carrier, from *3M Netherlands B.V.* The relevant material parameters are presented in **Table 4-1** and **Table 4-2**. All values are valid at room temperature (23°C). Indices are given for different coordinate directions with "1", "2" and "3" standing for the direction along in-plane longitudinal, in-plane transverse and out-of-plane, and with "T" and "C" standing for "tensile" and "compressive", respectively. Note that the values, presented in Table **Table 4-1**, are combined input values from different sources, as the provided material datasheet from *NTPT* was incomplete.

Longitudinal tensile strength	X_T	2,180MPa[a]
Longitudinal compressive strength	X_C	1,057MPa[a]
Transverse tensile strength	Y_T	81MPa[a]
Transverse compressive strength	Y_C	255MPa[d]
Longitudinal tensile modulus	E_{11T}	85,630MPa[a]
Transverse tensile modulus	$E_{22T} = E_{33T}$	9,060MPa[a]
In-plane shear modulus	$G_{12} = G_{13}$	5,000MPa[b]
Transverse shear modulus	$G_{23} = E_{33T} / (2(1+\nu_{23}))$	3,485MPa
In-plane shear strength	$S_{12} = S_{13}$	81MPa[b]
Transverse shear strength	S_{23}	35MPa[d]
In-plane Poisson's ratio	$\nu_{12} = \nu_{13}$	0.27[c]
Transverse Poisson's ratio	ν_{23}	0.30[c]

[a] based on material characterization tests, *ASTM D3039* / *D3518* / *D6641* [4-4 - 4-6]

[b] TDS of *NTPT Thinpreg™ 135* with *HS40/T800* carbon fibers in 67g/m² [4-7]

[c] Camanho et al. [4-8]

[d] TDS of *Hexply® F6376C-HTS (12K)-5-35%*, *HEXCEL / AIRBUS* [4-9]

Table 4-1: Adherend material properties

Tensile strength	X_{Adh}	46MPa[a]
Maximum elongation at break	ε_{tmax}	5.4%[a]
Tensile modulus	E_{Adh}	2,043MPa[a]
Poisson's ratio	ν_{adh}	0.34[b]

[a] Teixeira et al. [4-10]

[b] TDS of *Scotch-Weld™ AF 163-2K* 293g/m² [4-11]

Table 4-2: Adhesive material properties

4.2.2 Specimens

In order to examine the effect of ply thickness on tensile bonded joint strength, the SLJ was chosen as the reference design for this study. Three different design configurations were tested in which the SLJ geometry, with overlap length and width of 25.4mm, was kept constant but the composite laminate adherends ply thicknesses changed. **Table 4-3** shows the three composite adherend configurations, referred to as THICK, MEDIUM and THIN. In order to limit the study to the effect of the single ply thickness, the interface ply angle was kept the same for the three configurations as well as the adherend bending stiffness, ranging from 35.9GPa (THIN) to 37.9GPa (THICK). Based on CLT, the longitudinal bending stiffness was determined as the flexural engineering constant of a laminate given by

$$E_x^f = \frac{12}{D_{11}^* t^3} \quad (4\text{-}1)$$

for symmetric layups, with D^*_{11} being the first row/first column entry of the resulting inverse of the bending stiffness matrix, *t* being the overall laminate thickness and x corresponding to the direction along the SLJ-length (longitudinal direction) [4-12].
Five specimens were built per test configuration in accordance with *ASTM-D-5868* [4-13]. All adherend laminates were manufactured from the same Prepreg roll, with 32 layers of a single ply thickness of 50µm, adding up to 1.6mm total adherend thickness. The MEDIUM and THICK configuration were built by stacking blocks of 2 plies and 4 plies of the same ply angle, respectively. In this way an increase in ply thickness is achieved by the ply blocks, see **Table 4-3**. The idea of stacking ply blocks was already introduced by Sihn et al. [4-14] and is a common method for creating specimens of different ply thickness from the same Prepreg roll.

Design configuration	Stacking sequence	Eqv. longitudinal bending stiffness [GPa]	UD ply thickness [mm]
THICK (Ply block of 4 plies)	$[(45)_4/(0)_4/(-45)_4/(90)_4]_s$	37.9	4x 0.05 = 0.20
MEDIUM (Ply block of 2 plies)	$[(45)_2/(0)_2/(-45)_2/(90)_2]_{2s}$	36.6	2x 0.05 = 0.10
THIN (Single ply)	$[(45/0/-45/90]_{4s}$	35.9	1x 0.05 = 0.05

Table 4-3: Three test configurations with different ply thickness, by means of ply blocks of 2 layers for the MEDIUM and 4 layers for the THICK configuration

Composite adherends were laminated in a Prepreg hand layup process, with 5-10min of de-bulking at an under pressure lower than 100mbar between every fourth layer. The laminates were placed between a base plate of 12mm thickness and a caul plate of 2mm thickness from 2024-T3 aluminium alloy. An autoclave curing process comprised a single dwell step at 177°C and 5bar gauge pressure, with 800mbar under pressure inside the vacuum bag for 120min time. In order to minimize resin flow-out along the edges of the laminate, aluminium barriers were added. **Figure 4-1** shows optical microscopy images, *CARL ZEISS AxioCam ECr 5s* with 10x magnification, of the cross sectional cut of the three laminates with different ply thickness configurations after curing. The thickness of different ply blocks per configuration is visible. For the THICK configuration, the ply block of 4 layers can be identified as well as the symmetry line of the stacking sequence with 8 layers (2 times ply block). Correspondingly, for the MEDIUM configuration, the ply block of 2 layers and the symmetry line with 4 layers (2 times ply block) can be identified. Finally, for the THIN, the single layers and the symmetry lines are visible. The interface between the layers within one ply block is hardly noticed. Therefore, it is reasonable to consider a ply block as a single UD-layer with increased thickness.

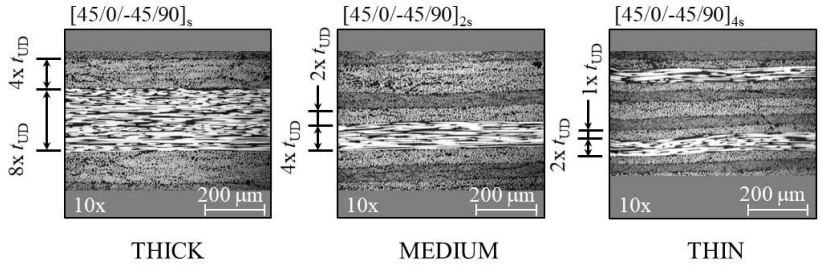

Figure 4-1: Cross sectional cut of laminates with different ply blocks, optical microscopy images, *Carl Zeiss AxioCam ECr 5s* with 10x magnification

4.2.3 Surface treatment

A suitable surface treatment prior to bonding was chosen as combination of degreasing the surface with Acetone and a 7min long exposure to UV-light inside an ozone containing atmosphere. The procedure was performed according to previous studies that showed good CFRP surface wettability after applying the same treatment [4-15 - 4-17]. The efficiency of the surface treatment was evaluated by measuring the contact angle of a 4µl distilled water, using the *TECHNEX Cam200/Attension Theta V4.1.9.8* system. The value of this contact angle reduced by 78.9%, from 101.3° (± 1.3°), before treatment, to 21.3° (± 0.9°), after treatment, for all configurations. These values are in accordance with literature and correspond to a good wettability of the surface [4-17].

4.2.4 Bonding

The uncured film adhesive was placed onto the treated surface of the cured adherends and a vacuum setup was arranged around it for the secondary bonding process. Curing was performed at 2bar autoclave pressure and 120°C temperature for 90min dwell time, while venting the vacuum bag to full atmosphere. After the bonding process, the average bond line thickness was measured 141µm (± 26µm), which deviates by 6% from the manufacturer's TDS of 150µm. This is considered within acceptable tolerance. Excess adhesive formed a small fillet at the bond line tips.

4.3 EXPERIMENTAL ANALYSIS

4.3.1 Experimental setup

Five specimens per layup configuration were subject to quasi-static tensile loading, in accordance with *ASTM D 5868-01* [4-13]. The displacement controlled tests were performed on a *ZWICK-ROELL Allround Line Z250 SW* testing machine with a load cell of 250kN, with a constant displacement rate of 1.3mm/min. **Figure 4-2** illustrates a schematic representation of the test setup. The specimen was held by two clamps at 250bar hydraulic pressure. The initial distance of the clamps was set at 200mm, with a misalignment of 1.8mm to counterbalance the overlap offset. A mechanical extensometer, *BTC-EXMACRO.H02* by *ZWICK-ROELL/testXpert II*, captured the elongation between two points of 60 mm distance, adjacent to the overlap area. Additionally, the strain field of the overlap area was monitored using DIC technique. For this, the *VIC-3D*™ system by *Correlated Solutions, Inc*. was used. In order to monitor the damage events of the specimens, an AE-system by *VALLEN Systeme GmbH* was employed, consisting of two *VS900-M* sensors, which were attached onto the same side of the specimen at ± 42.5mm from the overlap centre and connected to the *AEP4H 34dB* amplifier.

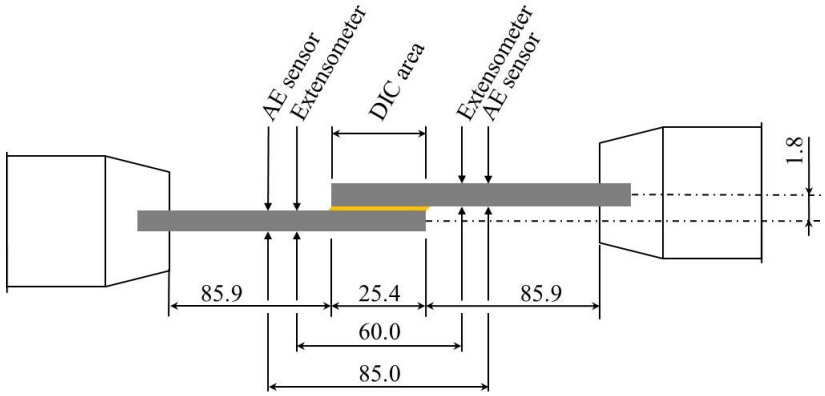

Figure 4-2: Test setup for static tensile loading, dimensions in [mm]

4.3.2 Load-displacement

Figure 4-3 a) shows typical load-displacement curves for the three different ply thickness configurations. The maximum load ranges (in average) from 16.1kN for the THICK to 18.5kN for the THIN configuration, which is an increase of 15% with decreasing ply thickness. The average lap shear strength (σ_{LSS}) in **Figure 4-3** b) is derived by dividing maximum load (P_{max}) over the bonded area for each specimen, given by the bond line length multiplied by the specimen width. The results show an increase of 16% in average lap shear strength when comparing THICK to THIN ply thickness configuration. In addition, the strain energy under the

load-displacement curve allows a comparison of average energy until failure for the three different ply thickness configurations. This has been derived determining the area under the load-displacement curve using a trapezoid rule. The result is presented in **Figure 4-3** c), indicating a 21% increase in strain energy for the THIN in comparison with the THICK ply thicknesses.

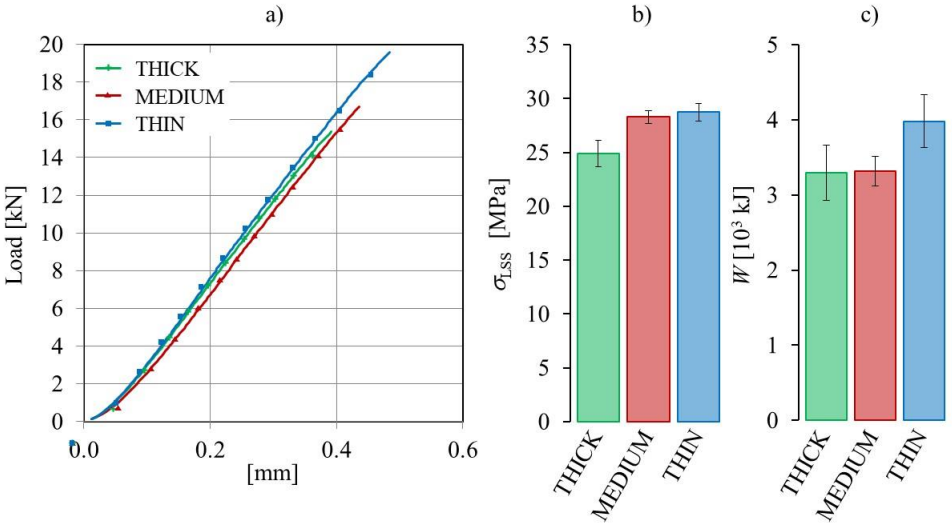

Figure 4-3: a) Typical load displacement curves, b) average lap shear strength (σ_{LSS} ± standard deviation) and c) strain energy (W ± standard deviation) for the three different ply thickness configurations

4.3.3 Damage initiation

Figure 4-4 and **Table 4-4** present the results from AE-monitoring recorded during tests. On the left hand side, in **Figure 4-4** a)-c), the chosen approach of previous **section 3.5.2** provides cumulative AE-hits (left axis) against recorded load (right axis) over the displacement for the three different configurations, THICK, MEDIUM and THIN, respectively. Unlike the results in **section 3.5.2** however, the characteristic knee-point is not clearly pronounced. On the right-hand side in **Figure 4-4** d)-f), instead, the cumulative energy (left axis) and the load (right axis) are plotted over the displacement.

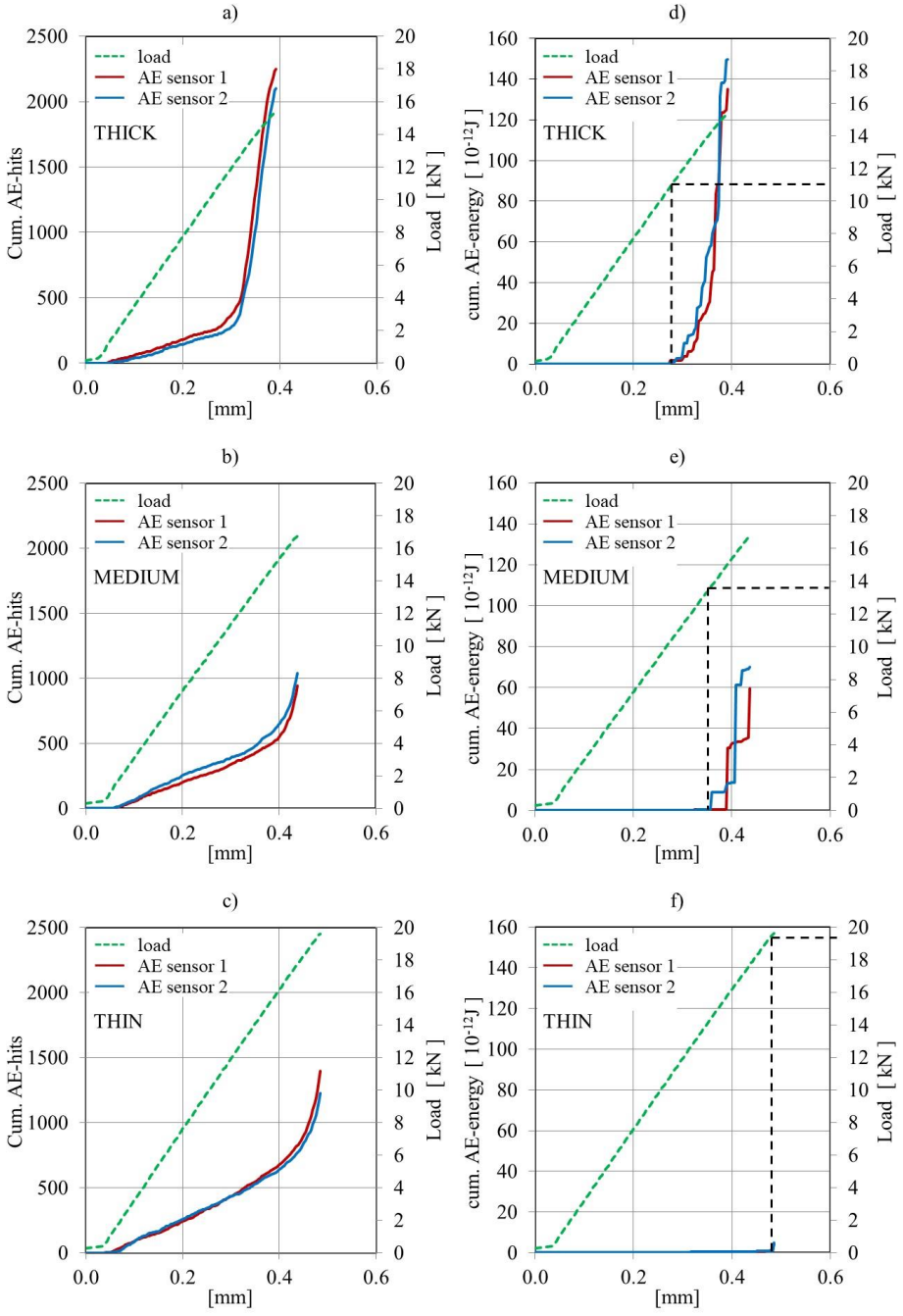

Figure 4-4: Typical measurements of cumulative acoustic hits [-] a)-c) and cumulative acoustic energy [10^{-12} J] d)-f) for the three different ply thickness configurations

All AE-hit plots on the left side of **Figure 4-4** start with a linear line with a small slope, until the number of hits increases significantly such that the line continues with a steeper slope. This trend is typical for all configurations. The point where the plots change to a steeper slope is believed to indicate damage initiation inside the specimen. The AE-hits in the initial slope region have no significant energy, and seem to accumulate energy only after the knee point.
Comparing the cumulative number of AE-hits on the left side, **Figure 4-4** a)-c), with the cumulative AE-energy on the right side, **Figure 4-4** d)-f), the significant change of the plots is more pronounced in the later. Therefore, the plots of **Figure 4-4** d)-f) are for this study chosen over the proposed method of **section 3.5.2**, to obtain the load at which damage first initiates, proposing the following criterion:

$$E^{AE}_{i} > 0.10 \text{ x } 10^{-12} \text{ J} \quad \text{AND} \quad E^{AE}_{i+1} \geq 2 \text{ x } E^{AE}_{i} \quad (4\text{-}2),$$

with E^{AE}_{i} being the acoustic energy per hit. The criterion was set to be consistent for all cases in **Chapter 4**. Based on the results, it can be observed that, the displacement at which damage initiation is believed to occur, is postponed to higher values when decreasing the ply thickness. The number of hits as well as the cumulative AE-energy after this knee point are significantly reduced for the THIN ply configuration. However, on the number of hits, in **Figure 4-4** a)-c), this difference is more visible between the MEDIUM and THICK configuration than between the MEDIUM and the THIN. The final cumulative energy, in **Figure 4-4** d)-f) changes significantly between the configurations, in average from 163 x10^{-12}J in case of the THICK down to 9 x10^{-12}J for the THIN configuration. At the same time, the displacement at damage initiation increases from 0.28mm up to 0.40mm when comparing the THICK to the THIN configuration. By comparing the position of the knee point for the three different ply thickness configurations, it can be concluded, that the damage initiation is postponed to 47% higher loads with decreasing ply thickness. **Table 4-4** summarizes maximum load as well as load and displacement at damage initiation in comparison with the total amount of cumulative hits and AE-energy, for the three different ply thickness configurations. The cumulative AE-energy per configuration was thereby derived in two steps: firstly, the final cumulative energy of each of the two sensors was averaged for each specimen. Secondly, the cumulative AE-energy was averaged over all specimens per configuration.

Design	THICK	MEDIUM	THIN
Maximum load P_{max} [kN]	16.1 (± 0.8)	16.9 (± 0.4)	18.5 (± 0.7)
Lap shear strength σ_{LSS} [MPa]	24.9 (± 1.2)	28.3 (± 0.6)	28.8 (± 0.8)
Strain energy W [10^3 kJ]	3.3 (± 0.4)	3.3 (± 0.2)	4.0 (± 0.4)
Load at damage initiation [kN]	11.1 (± 0.8)	13.5 (± 0.9)	16.3 (± 1.5)
Displacement at damage initiation [mm]	0.28 (± 0.02)	0.35 (± 0.01)	0.40 (± 0.04)
Cumulative AE-hits	2063 (± 469)	847 (± 149)	826 (± 281)
Cumulative AE-energy [J]	162.8 (± 41.9)	41.3 (± 12.9)	8.5 (± 4.3)

Table 4-4: Maximum load (P_{max}), lap shear strength (σ_{LSS}) and energy (W), load / displacement at damage initiation, based on cumulative AE energy release, for the three different ply thickness configurations (average (± standard deviation))

4.3.4 Final fracture surfaces

Figure 4-5 shows typical fracture surfaces of the different ply thickness configurations. The fracture surfaces show that the failure occurred partly inside the composite and partly inside the adhesive. However, in all cases the composite failure clearly dominates the final fracture surface. A comparison of the three configurations reveals that the final fracture surface spreads over a larger area with increasing UD-ply thickness. The difference in total fracture surface between the configurations is quantified in **Table 4-5**, being A_f^{comp} and A_f^{coh} the area of the fracture surface inside the composite adherend, and inside the adhesive, respectively, A_f^{total} the total area of the fracture surface and A_{OL} the overlap area. On average, the total fracture surface in the THICK configuration is of 760mm^2, decreasing to 668mm^2 for the MEDIUM and to 637mm^2 for the THIN configuration.

Design	THICK	MEDIUM	THIN
A_f^{comp} [mm^2]	721 (± 59)	651 (± 19)	607 (± 265)
A_f^{coh} [mm^2]	38 (± 25)	17 (± 9)	30 (± 145)
$\frac{A_f^{coh}}{A_f^{comp}+A_f^{coh}}$ [%]	5.1 (± 3.0)	2.6 (± 1.3)	4.7 (± 2.2)
$\frac{A_f^{total}}{A_{OL}}$ [%]	117.8 (± 9.5)	103.5 (± 1.9)	98.8 (± 4.2)

Table 4-5: Fracture surface analysis, average values (± standard deviation)

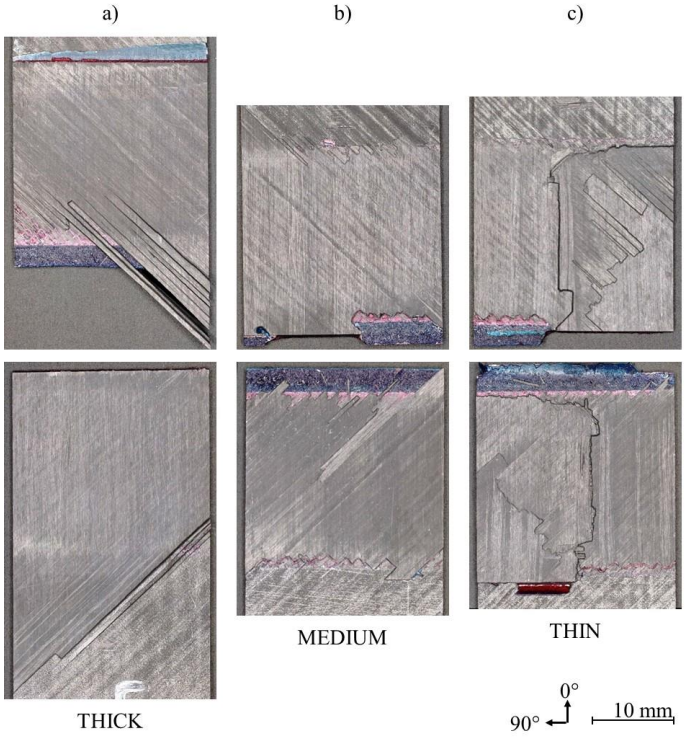

Figure 4-5: Typical fracture surfaces for each ply thickness configuration after final failure

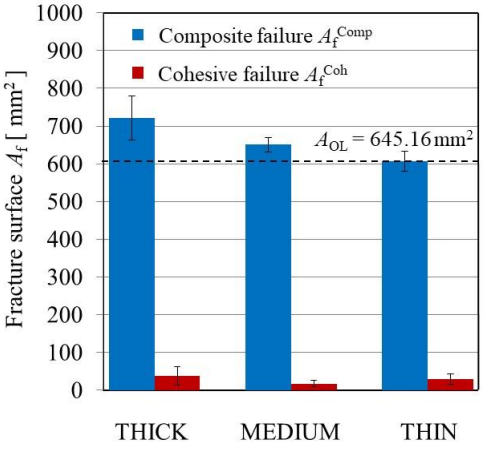

Figure 4-6: Composite and cohesive failure in comparison for each ply thickness configuration after final failure

In **Figure 4-6**, the portion of composite versus cohesive failure is plotted for each ply thickness configuration. Comparing the three areas of cohesive failure, there is no visible trend. An

average cohesive fracture surface area of 38mm^2 for the THICK decreases to 17mm^2 for the MEDIUM and increases again to 30mm^2 for the THIN configuration. Comparing the area of cohesive versus total failure, the THICK configuration resembles 5.1% cohesive failure, while the MEDIUM contains 2.6% and the THIN 4.7% of the fracture inside the adhesive.
Post mortem fracture surface analysis was performed using the *KEYENCE VR5000* wide-area 3D profiling system. **Figure 4-7** shows the bottom side of a typical THICK configuration (**Figure 4-5** a). The final fracture surface is presented as a 3D profile. A cross section profile along the length of the overlap is also shown below the 3D profile. This height profile throughout the overlap region gives an idea where the crack has travelled through the laminate. **Figure 4-8** and **Figure 4-9** show the 3D and the height profile along the overlap length for the typical MEDIUM and the THIN configuration. The ply thickness t_{UD} represents the single layer thickness in case of the THIN but the total thickness per ply block, in case of the MEDIUM and THICK configurations. The experimental ply thickness deviates from the nominal values of **Table 4-3** by about 10%.

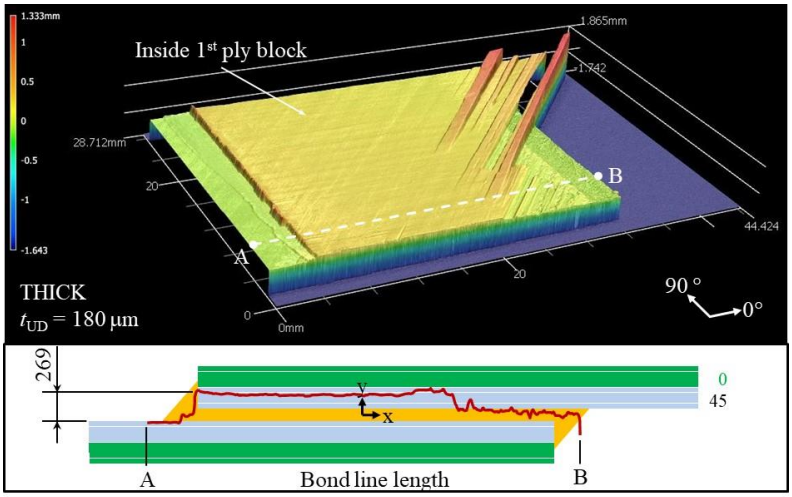

Figure 4-7: Final fracture surface of a typical THICK configuration

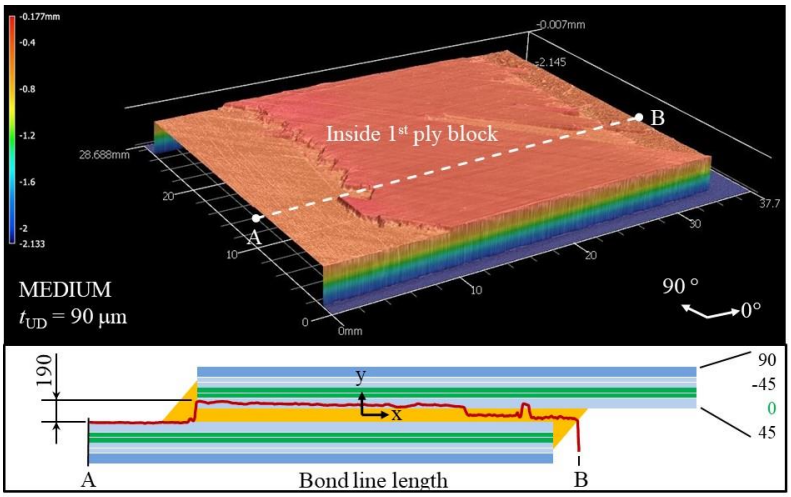

Figure 4-8: Final fracture surface of a typical MEDIUM configuration

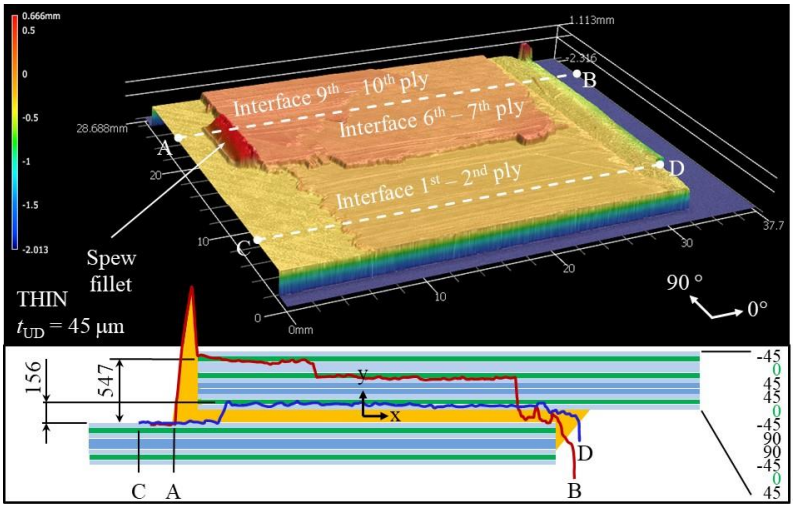

Figure 4-9: Final fracture surface of a typical THIN configuration

In the THICK configuration, in **Figure 4-7**, the crack progresses partly inside the first 45° ply block of the top adherend, and partly inside the adhesive bond line. A similar crack propagation is visible in the cross-section cut of the MEDIUM configuration, in **Figure 4-8**. However, in **Figure 4-9**, there are several steps inside the composite laminate of the upper adherend visible in the final fracture surface of the THIN configuration. Two paths are plotted along the overlap length. In the path A-B, the crack overcomes multiple laminae and reaches up to the 10th layer away from the adhesive bond line, propagating in the longitudinal (in-plane) direction. After 30% of overlap length, the crack path changes to transverse (out-of-plane) direction, dropping through the thickness of the adherend, and continues in the longitudinal (in-plane) direction

along the interface of the 6th and 7th ply. In the second path C-D, the final fracture surface was identified on the interface between 1st and 2nd layer. In all three cases, the fracture surface tends to locate near the interface between a 0°- and a 45°-ply.
It is important to notice that, for the THICK and MEDIUM, the crack despite intralaminar within 45° ply blocks seems to propagate preferably at the interface between two 45°-plies, which would actually mean interlaminar failure. This is no longer the case for the THIN (no ply blocks), where the crack path is along the 0/45°-interface. In the microscopic images of **Figure 4-1**, the interface within a ply block is much less pronounced than the interface between plies of different orientation, due to nesting effects. Nevertheless, the crack path for THICK and MEDIUM seems to be affected by the interface of the ply blocks. The fracture patterns could potentially be different if the different ply thicknesses were achieved by producing plain plies of different thicknesses instead of a ply block.

4.4 NUMERICAL ANALYSIS

4.4.1 Numerical model

A FEA of the SLJ geometry under tensile loading was performed with the commercial software *ABAQUS 2017*. The purpose of this FEA was to numerically simulate the experimental tests up to damage initiation. An implementation into a 3D model gives insight into the stress field around the bond line, aiming to capture load and location of damage initiation and help to interpret the resulting failure mechanisms. The composite was modelled as linear elastic, based on the properties listed in **Table 4-1** while the adhesive was modelled linear-elastic, using the values from **Table 4-2**. The bond line thickness was modelled with 150µm (nominal thickness). The load was applied in a single step with 6 load increments taking into account non-linear geometry effects. The specimen between the clamps was simulated using continuous 3D solid elements with reduced integration (*C3D8R*). **Figure 4-10** illustrates the model with the boundary conditions and mesh. At the right side all nodes inside the cross-sectional surface were blocked in 3 DoF, while on the left side, solely longitudinal displacement was allowed (x-direction).

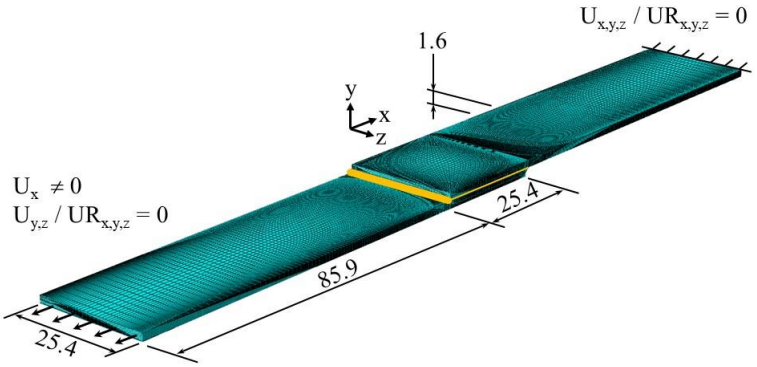

Figure 4-10: 3D FE-model between the clamps with specimen dimensions in [mm], and boundary conditions

The region around the left overlap edge is highlighted in **Figure 4-11**. The spew fillet geometry is an approximation of its experimental counterpart. All specimens of this study had a spew fillet shape similar to a 45° triangle. In all cases, the spew fillet reached at least up to half of the adherend's height (= 0.8mm). Based on this, it was decided to model a triangular fillet shape of 45° slope reaching up half the height of the adherend, as a good approximation to represent the specimens within this study.

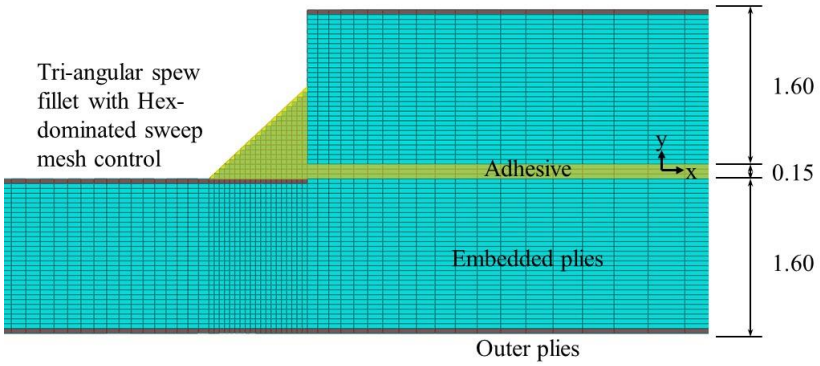

Figure 4-11: Zoom on overlap region with triangular spew fillet and material section assignments, all dimensions in [mm]

4.4.2 Mesh convergence

To guarantee that the results were mesh independent, a mesh convergence study was performed. In **Figure 4-12**, the peel stress (σ_{yy}) is plotted along the overlap length, from left to right, including the length of both fillets in **Figure 4-12** a), and through the thickness of the overlap left edge, from bottom to top in **Figure 4-12** b). Both paths are situated in the centre of the joint

in width direction. The length and width of one element in the overlap tip region is set to 100µm, while the thickness of one element corresponds to one UD-ply thickness of 50µm, throughout the whole model. In order to avoid showing the stress jumps at the interface, the path in **Figure 4-12** a) was chosen exactly in the middle of the bond line and in **Figure 4-12** b) 5µm inwards of the overlap end, in x-direction.

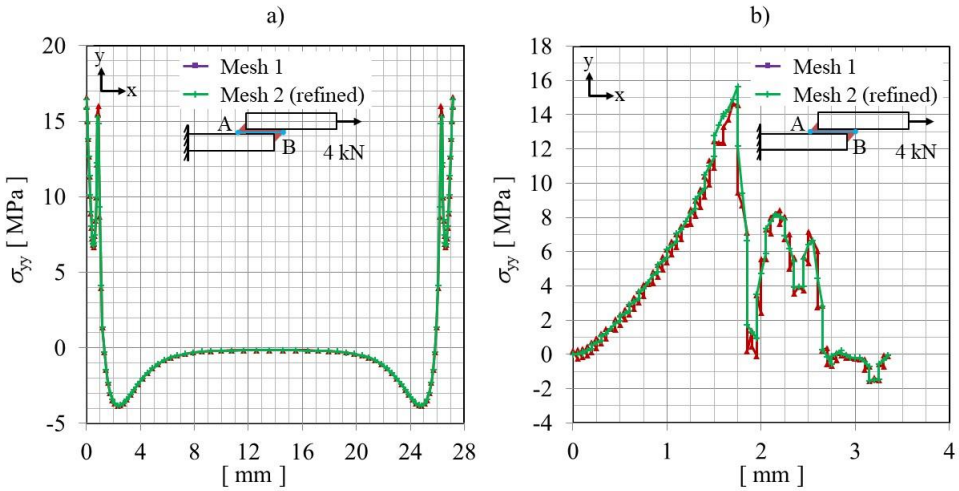

Figure 4-12: Mesh convergence study on peel stress (σ_{yy}) distribution along overlap length a) and through bond line thickness b)

Mesh 1 is composed of 3D brick elements with 8 nodes (linear interpolation) and reduced integration (one integration point at the centre of the brick). These elements in *ABAQUS* are referred to as *C3D8R*. The dimensions of Mesh 1 (*C3D8R* in green) in **Figure 4-12** a) were based on the smallest element size at the bond line region with the dimensions length = 100µm, width = 100µm and height = 50µm. Towards the clamps the size of the elements is gradually increased, leading to 921,344 elements of type *C3D8R* in total. Mesh 2 is a mesh refinement of Mesh 1. The refinement has been performed in two ways: (1) by increasing the number of elements in the overlap region, leading to a total number of 2,036,516 elements and (2) by increasing the number of integration points within one element from 1 to 8, choosing a 3D-solid element with linear interpolation of type *C3D8* with no reduced integration (8 integration points) (Mesh 2 in red). The mesh refinement (Mesh 2 in comparison with Mesh 1) affects the stress distribution around the tip of the overlap. A difference in maximum stress values of 4.6% in **Figure 4-12** a) and 6.5% in **Figure 4-12** b) was considered a sufficient convergence with the coarser Mesh 1 of 921,344 elements of type *C3D8R*. All results presented in this study are therefore based on Mesh 1.

4.4.3 Model validation

In order to validate the numerical simulations, the strain distribution measured during test by means of DIC is compared with numerical results. **Figure 4-13** shows a representative example of the peel strain distribution along the mid-thickness of the bond line. In width direction, the paths are set along the edge of the bond line, where the strains from the DIC are recorded. The presented values correspond to the design configuration with MEDIUM ply thickness of 100µm and layup $[(45)_2/(0)_2/(-45)_2/(90)_2]_{2s}$ at a reference load of 4kN. This value has been chosen to make sure the comparison is performed before damage initiation occurred in the test.

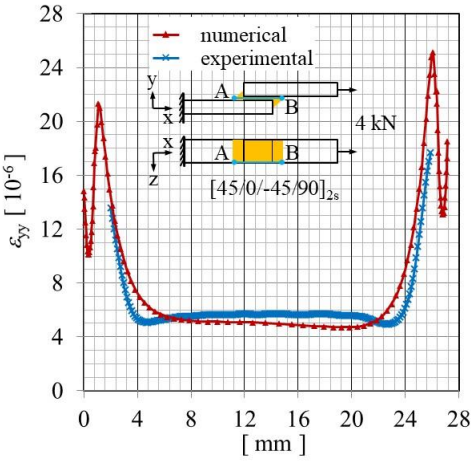

Figure 4-13: Peel strain(ε_{yy}) along the bond line in [10^3 microstrain], numerical versus experimental method

Overall, the numerical analysis agrees well with the experimentally measured strain distribution. However, there are some deviations between the plots towards the bond line tips. This is believed to be caused by two main reasons: 1) the strain field captured by the camera is representing the strain of the colour coating, that was applied to provide a contrast rich speckle pattern, as common for DIC systems and therefore some discrepancy between these and the real adhesive strain is expected; and 2) due to the quite small adhesive bond line thickness of 141µm, the method to extract strain values via image correlation software *Vic3D 7*, is prone to inaccuracy when picking the peel strain (ε_{yy}) visualization path, which may not exactly match the same location as that of the numerical model.

Moreover, **Figure 4-13** also shows an asymmetry of the numerical strains at the edges. This asymmetry decreases significantly towards the mid-width of the specimen. This effect is believed to occur due to a layup related reason: the laminate is not antisymmetric, so that, according to the given CLT, the entries D16 and D26 of the ABD matrix have values unequal zero [4-12]. This instance leads to a bending-twisting coupling inside the laminated adherends. The offset between the adherends due to the SLJ geometry causes an inevitable momentum of

secondary bending, which induces a twist to the joint, translating into a difference in peel stress between the left and right bond line tip.
When comparing the strain distribution of the three different configurations inside the adhesive along the bond line, a decrease in asymmetry with thinner ply thickness can be observed. A laminate with infinitesimal ply thickness would have no more coupling effect and consequently no more asymmetry in the plot. This change in asymmetry of the strain distribution inside the adhesive with decreasing ply thickness may influence the global joint behaviour. But it is believed this would marginally affect the peak peel and shear stress values at damage initiation or at final failure.

4.4.4 Numerical stress analysis

Once the numerical analysis is validated, it can be further explored to study the stresses around the overlap region. **Figure 4-14** presents the shear (τ_{xy}) and peel (σ_{yy}) stress distribution along the bond line length for all layup configurations given by the numerical model at a pre-defined load of 4kN. None of the tested specimens indicated any significant amount of AE-hits nor accumulated AE-energy up to this load. Therefore, the value was set in order to stay within a region before damage initiation. The plot path is taken at the centre position in width direction of the joint and mid-thickness of the bond line. The results show almost identical stresses along the bond line for the three configurations, both in shear (τ_{xy}) and peel (σ_{yy}).

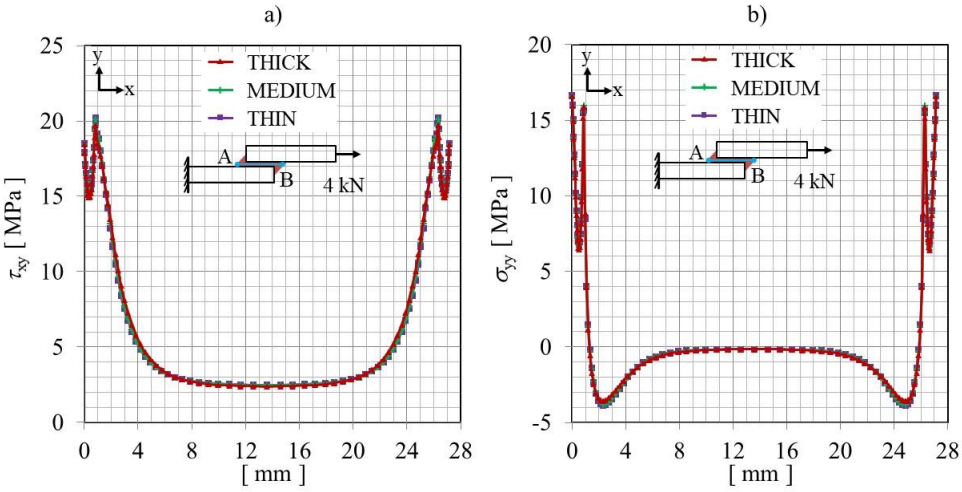

Figure 4-14: Numerical comparison of a) shear stress (τ_{xy}) and b) peel stress (σ_{yy}) along the full bond line length including the spew region, at mid-width position

In **Figure 4-15**, plots are taken at the center position in width and cover the complete overlap thickness of 3.35mm length from bottom to top. **Figure 4-16** gives, a closer look of the same stresses near the region of the adhesive bond line.
Figure 4-15 shows that stresses vary inside the composite adherends depending on the ply

thickness, while remaining again almost identical inside the adhesive. The shear stress (τ_{xy}) distribution in **Figure 4-15** a) differs significantly, while the peel (σ_{yy}) stress plots in **Figure 4-15** b), are more consistent for the different ply thickness configurations. This effect is related to the ply thickness, or in fact to the different stacking sequences of the THIN, MEDIUM and THICK configuration in **Table 4-3**. As shown in previous work from the authors [4-18], the fiber orientation does not have a large influence on the out-of-plane peel stress distribution inside the adherend, while for the shear stresses, as an in-plane stress, the fiber orientation has a significant influence on its stress distribution.

As stated in **Table 4-3**, the equivalent laminate bending stiffness of the adherends as well as the outermost layer in contact with the adhesive are kept constant throughout the test design. Therefore, global and local stiffness of the adherends remain constant and the adhesive experiences the same peel and shear stresses in all three configurations.

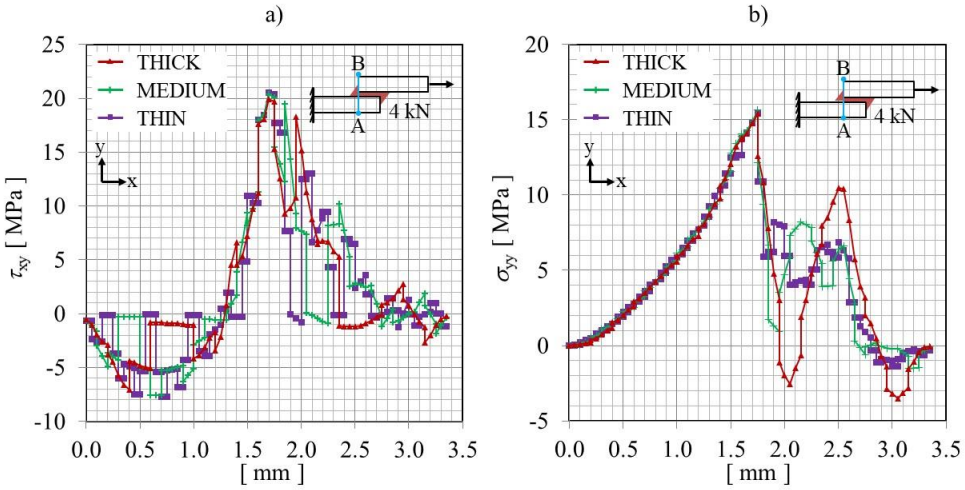

Figure 4-15: Numerical comparison of a) shear stress (τ_{xy}) and b) peel stress (σ_{yy}) through the full overlap thickness, at mid-width position

Looking closer onto **Figure 4-16**, the maximum (σ_{yy}) and shear (τ_{xy}) stress are situated at different locations inside the joints: both the shear (τ_{yx}) and peel (σ_{yy}) stress have their maximum at the interface between the outermost 45° layer and the adhesive, towards the upper adherend. This point is indicated in **Figure 4-16** a) and b) with the right dashed line. Inside the adhesive, the maximum shear (τ_{yx}) stress is at the center of the adhesive in the through-thickness direction. The maximum peel (σ_{yy}) stress, however, is more pronounced towards the interface with the upper adherend, **Figure 4-16** a) and b), right dashed line. These observations for maximum (σ_{yy}) and shear (τ_{xy}) stress are consistent for all three configurations. Therefore, it can be concluded that, a different adherend ply thickness does not have an influence in the location of stress hot spots inside the adhesive, when looking through the thickness at the tip of the bonded region.

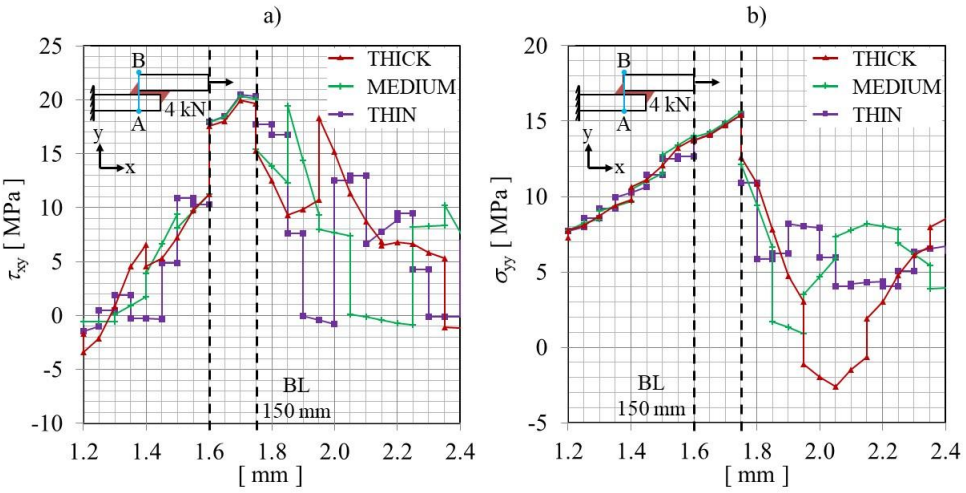

Figure 4-16: Numerical comparison of a) shear stress (τ_{xy}) and b) peel stress (σ_{yy}) around the adhesive bond line, at mid-width position

4.5 DISCUSSION

4.5.1 Sentry-function

A correlation of the AE-data and load-displacement curves can give more insights into the damage characterization. One method, which is used for this correlation, is called *Sentry function* [4-19]. The *Sentry function* is the natural logarithm of the ratio between mechanical and acoustic emission energies, reading:

$$f(x) = ln\frac{E_s(x)}{E_a(x)} \quad (4\text{-}3)$$

where $E_s(x)$, $E_a(x)$ and x are the strain energy, the AE-energy and the displacement, respectively. The strain energy is taken as the area under the load-displacement curve whereas the AE-energy is the summation of energy of each wave. Depending on the material damaging progression, the *Sentry function* behaviour can take any combination of the following four trends:

- Type I (P_I (x)): Increasing trend, representing a strain energy storing phase
- Type II (P_{II} (x)): A sudden drop of the function which may be related to a significant internal material failure occurrence
- Type III (P_{III} (x)): An equilibrium state between the mechanical and AE-energy

- Type IV (P_{IV} (x)): A decreasing behaviour which is related to the fact that the AE-activity is greater than the material strain energy storing capability, so that the damage has reached a maximum

For a typical specimen of each configuration, the *Sentry function* is plotted over the load-displacement curve in **Figure 4-17**. The beginning of the load-displacement curve, up to a displacement of 0.65mm, is excluded here: an initial non-linearity in the load-displacement curves ("toe") at the start of the test would lead to a large (Type II) drop, but does not correspond to any form of damage initiation. A similar general trend is visible for all three different ply thickness configurations. The logarithmic plot starts with a (Type II) drop in case of MEDIUM and a gentler (Type IV) in case of the THIN configuration. In all three configurations there is a slightly increasing trend (Type I) pronounced over the majority of the plot. In the MEDIUM configuration, this (Type I) trend changes into a (Type III) plateau. With decreasing ply thickness, the length of this (Type I) trend, or in case of the MEDIUM (Type III) plateau, increases, followed by a sudden drop of (Type II) and a subsequent decreasing behavior of (Type IV) until final failure. This last Type IV is longer, in terms of displacement, for the THICK than the MEDIUM and it disappears for the THIN.

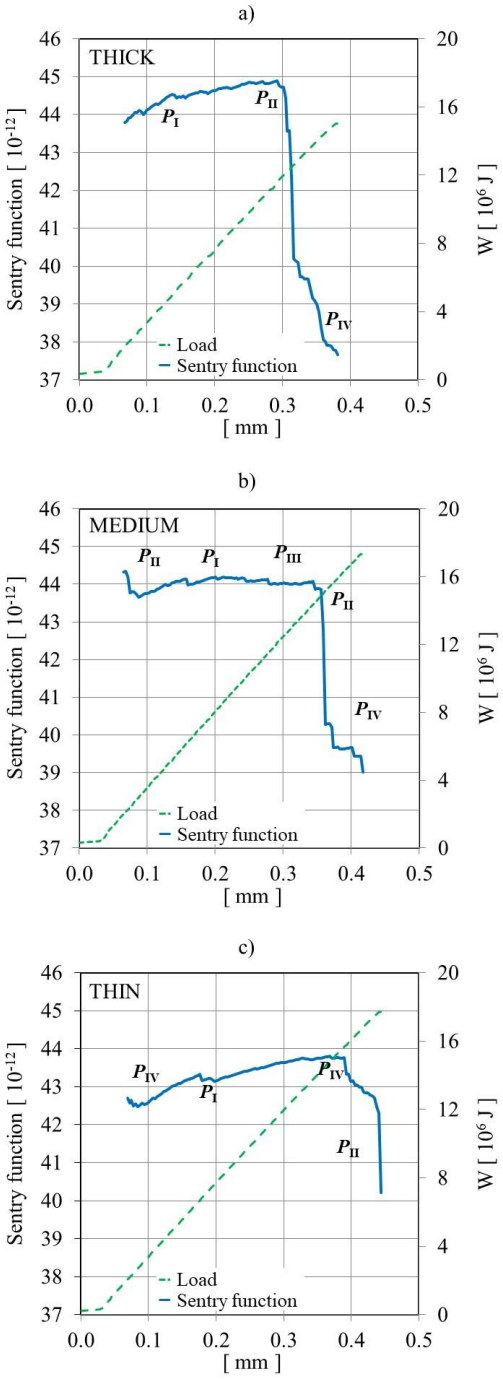

Figure 4-17: *Sentry function* over load-displacement curve for different ply thickness configurations

The initial (Type II) drop observed in the MEDIUM configuration as well as the less pronounced (Type IV) decrease in the THIN configuration may be related to possible manufacturing defects inside the adhesive bond line. It is believed that those defects are significant in terms of acoustic energy in relation to the so far energy stored in the specimen but not significant enough in relation to the overall damage process. Further findings of the *Sentry function* analysis will be discussed after presenting the results of the section hereafter.

4.5.2 Failure analysis

The numerical approach to derive the load at damage initiation was established by post-processing the stress tensor for each node. A set of user-defined subroutines was built to contain various failure criteria. For the adhesive, the *Mises* as well as the *Drucker-Prager* yield criterion were used. In the later, the study follows the approach of da Silva et al. [4-20], where the yield criterion can be expressed as

$$aq^b - p = p_t \quad (4\text{-}4)$$

The terms that appear in (4-4) are defined as in previous **section 3.6.3**, with b as the exponent parameter, σ_{yt} for the yield stress of the adhesive in tension, β representing the ratio of yield stress in compression to the yield stress in tension and σ_1, σ_2 and σ_3 being the principal stresses at the element nodes. In this study, there were no experimental values available for the compressive yield stress of the chosen adhesive *HYSOL EA 9695^{TM} 050K AERO*. The β-value was chosen 1.45, based on values found in literature for adhesives with comparable Young's modulus and yield strength [4-10].

For the ply failure inside the composite, the *3D-invariant based* criterion of Camanho et. al. [4-21] was used. The criterion distinguishes between fibre and matrix failure. In this criterion, the strength of a single UD-layer inside a stacking sequence varies with respect to its ply thickness and position within the sequence. This in-situ effect is incorporated, following the work of Camanho et al. [4-8]. The UD-properties in comparison with their elevated in-situ representative are shown in

Table 4-6. The values show how much the values increase with respect to their position and thickness.

	In-plane shear strength S_L	Transverse shear strength S_T	Transverse tensile strength Y_T	Transverse biaxial tensile strength Y_{BT}	Transverse compressive strength Y_C
UD / ply block	81[a]	35[b]	81[a]	50[c]	-255[b]
Double-THICK 0.40mm INNER	99	43	128	88	-299
THICK 0.20mm OUTER	85	37	81	50	-266
THICK 0.20mm INNER	104	45	128	86	-310
MEDIUM 0.10mm OUTER	104	45	114	73	-310
MEDIUM 0.10mm INNER	126	54	180	130	-358
THIN 0.05mm OUTER	126	54	161	109	-358
THIN 0.05mm INNER	151	65	255	204	-408

[a] based on material characterization tests, *ASTM D3039 / D3518 / D6641* [4-4 - 4-6]

[b] TDS of *NTPT Thinpreg™ 135* with *HS40/T800* carbon fibers in 67g/m² [4-7]

[c] Camanho et al. [4-8, 4-21]

Table 4-6: Adherend in-situ material properties, all values in [MPa]

Figure 4-18 and **Table 4-7** present the comparison of experimental and numerical results. On the experimental side, the values for average lap shear strength (dark-blue) were directly provided by the load cell and the values for average shear stress at damage initiation (light-blue) were derived from cumulative AE-energy plots – see **Table 4-4**. On the numerical side, the stress tensor of the *ABAQUS* output database (ODB) was post-processed through a set of user-defined subroutines, containing the failure criteria. The non-linear FEA indicates damage initiation inside the adhesive at lower loads than inside the composite. For all ply thicknesses, both *Mises* (dark-purple) and *Drucker-Prager* (light-purple) stress-based criteria indicate a failure initiation inside the adhesive at lap shear stresses between 7.4MPa and 8.7MPa, which

is at about 30% of the maximum load applied. Damage initiation inside the composite, given by the *3D-invariant based* failure criteria (green), is indicated in the same range as adhesive failure, in case of the THICK ply thickness, but then rises to higher stresses than in the adhesive for the other ply thicknesses. The failure inside the composite follows the trend of the experimental values, obtained by AE-signals, although at about 40% lower stresses, while failure inside the adhesive remains constant for all configurations. Consequently, the difference between adhesive failure and composite failure increases with decreasing ply thickness. This discrepancy may be caused by the sensitivity of the failure analysis. The subroutine runs all nodes of the model and indicates failure as soon as the first node reaches a failure index > 1. The AE-sensors on the other hand are set to a minimum threshold for signal recording of 50dB and it is believed that these two thresholds may not be comparable.

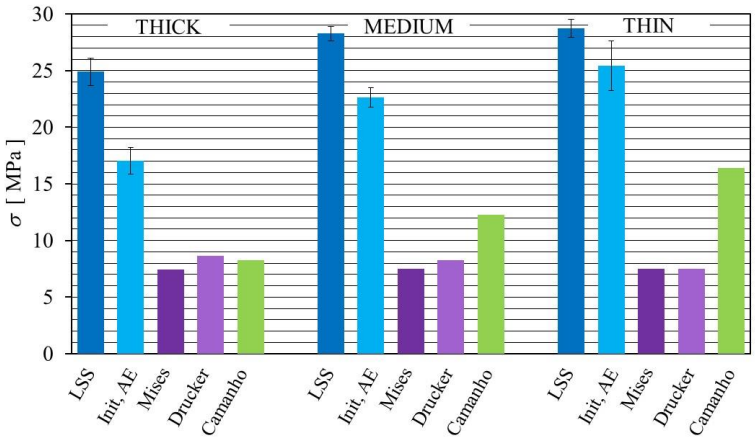

Figure 4-18: Experimental average lap shear strength versus experimental and numerical average shear stress at damage initiation

Configuration	σ_{LSS} EXP	$\sigma_{init,\ AE}$ EXP	*Mises* NUM	*Drucker Prager* NUM	*Camanho* NUM
THICK	24.9 (± 1.2)	17.0 (± 1.2)	7.4	8.7	8.3
MEDIUM	28.3 (± 0.6)	22.6 (± 0.9)	7.5	8.2	12.3
THIN	28.8 (± 0.8)	25.4 (± 2.2)	7.5	7.5	16.4

Table 4-7: Average lap shear strength versus stress at damage initiation: Experimental (EXP) and numerical (NUM) approaches, all values in [MPa] (±standard deviation)

Figure 4-19 illustrates the location of failure, focussing on the region around the left bond line tip. The 3D model is reduced to a 2D illustration, showing only those nodes in x-y-plane, with the highest failure index in the width direction of the specimen (z-plane). The location of failure was determined at the node coordinates given by the *ABAQUS* ODB-file.

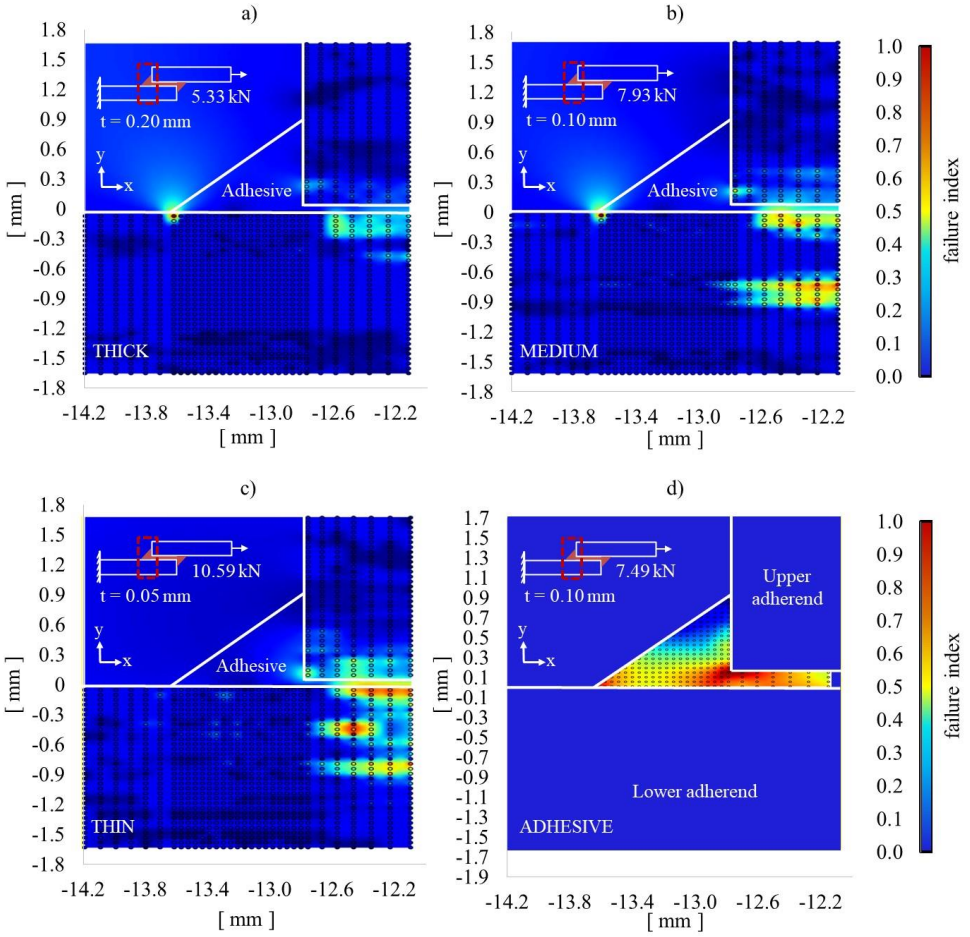

Figure 4-19: FEA-location of damage initiation

Figure 4-19 a) – c) illustrates the distribution of failure indices inside the composites, for the different ply thicknesses a) THICK, b) MEDIUM, c) THIN. In all three cases, composite failure is indicated in the region around the bond line tip of the non-free adherend side. The location may arbitrarily switch from the left to the right tip since stresses are fairly similar in both overlap tips. It is noticeable how the failure moves from the outer ply (first layer in contact with the adhesive bond line) towards the center of the adherend with decreasing ply thickness. In case of the THIN ply thickness, in **Figure 4-19** c), a high failure index close to 1 is indicated in three different interfaces, which points towards the observations from the final fracture surfaces in **Figure 4-9**. **Figure 4-19** d) presents the failure pattern inside the adhesive, based on the *Mises* criterion. Here, the results for different ply thicknesses were very close to each other. Therefore, the plot of the MEDIUM ply thickness is chosen, to represent all three cases. Unlike in the composite, the highest index values for adhesive failure are indicated towards the upper adherend (free edge) at the tip of the overlap.

Following Camanho's approach, allowables for transverse matrix strength are enhanced due to the application of the in-situ theory [4-8]. Therefore, a decrease in ply thickness must consequently lead to first ply failure inside the composite at a higher load. This thought correlates with the observations of AE-signals, which show that the sudden increase of cumulative acoustic energy occurs at higher loads when decreasing the ply thickness. The observation is also in agreement with recent studies of Amacher et al. [4-2] and Cugnoni et al. [4-3], who showed that a decrease in ply thickness postpones damage initiation and leads to higher fatigue life as well as impact resistance.

In the FE analysis, stresses in the adhesive before damage initiation are almost identical in all three cases. So, a decrease in ply thickness would primarily affect the damage initiation inside the composite adherend. The prediction of the first-ply failure location inside the composite matches the observations of the fracture surface analysis in **section 4.3.4**, where the fracture plane in case of the THIN configuration reached much deeper inside the composite adherend. However, the final fracture surfaces in **Figure 4-5** enable a glance at the last failure of the entire bonded joint, but do not tell about the location of damage initiation or propagation.

The result of the final fracture surfaces raises the question, how the crack could overcome several layers inside the composite, when reaching a sufficiently small ply thickness in the THIN configuration. From the experimental side of this study, it appears that decreasing the ply thickness favours multiple transverse matrix cracking, as in the THIN, instead of single in-plane delamination, as in the THICK and MEDIUM. The in-situ theory might give an answer: While in THIN plies, multiple small cracks are in favor to propagate transversely, in THICK plies a transverse crack would turn into fiber direction and propagate as delamination, once it reaches the next interface between two plies.

The numerical results indicate that the damage initiation occurs at a lower load inside the adhesive than inside the composite. The discrepancy raises the question, whether the experimental AE-results are to be related to the composite failure alone. Both matrix and adhesive materials have very similar stiffness and density properties, and their location with respect to the position of the AE-sensors is almost identical, so that the AE signal does not specifically tell, if a failure happens inside the matrix of the composite laminated adherend or inside the adhesive. However, when looking onto **Figure 4-4** a)-c), the cumulative AE-hits do indicate some form of damage in the early stage, before reaching the knee point of significant increase in acoustic energy release. It is believed, that the adhesive inside the bond line suffers early damage at low loads, which is captured by the *Mises* and *Drucker-Prager* criterion, before the *3D-invariant based* criterion indicates damage initiation inside the composite, which correlates with the massive increase in cumulative acoustic energy in **Figure 4-4** d)-f). In addition, it can be expected that the adhesive has a more ductile behaviour than the composite adherend. It is believed that this ductile damage would be less easily detectable by AE than the more brittle damage of the adherends.

The location, where the *Sentry function* undergoes its sudden drop (Type II), can be related to the location of significantly increasing cumulative AE-energy, of **Figure 4-4** d)-f). It is believed that this significant increase in acoustic energy (or sudden drop of the *Sentry function*), which occurs at higher displacement with decreased ply thickness, indicates the damage initiation

inside the composite adherends. This result would meet the expectations based on previous studies on thin ply composites: a decrease in ply thickness postpones damage initiation to higher loads, while decreasing the damage tolerance of the composite until final failure [4-2, 4-3]. The second part of this statement correlates to the experimental AE-results. The amount of cumulative AE-energy after the point of damage initiation represents the last (Type IV) drop of the *Sentry function* and is significantly less pronounced with decreasing ply thickness. Finally, a comparison of the joint configurations can be made, by correlating the load at damage initiation ($\sigma_{\text{init,AE}}$) and load at final failure (σ_{LSS}). The term "damage resistance" can be proposed as

$$D = 1 - \frac{\sigma_{init,AE}}{\sigma_{LSS}} \quad (4\text{-}5)$$

The values of **Table 4-7** result in a damage resistance of 0.31 (± 0.08) for the THICK, 0.20 (± 0.04) for the MEDIUM, and 0.12 (± 0.06) for the THIN configuration. Consequently, a decrease in ply thickness from the THICK to the THIN configuration is related to 61% lower damage resistance inside the composite adherend.

4.6 CONCLUSION

This study aims to explore the effect of the ply thickness on the damage initiation and final failure of CFRP bonded SLJ. Three different ply thickness configurations of 200µm (THICK), 100µm (MEDIUM) and 50µm (THIN) were tested under quasi-static tensile loading. Tests were monitored using AE-techniques to follow the damage events. An FEA was performed to numerically simulate the experimental tests up to damage initiation. From the analysis of the results the following conclusions can be drawn:

- Decreasing the single ply thickness of laminated composite adherends increases the maximum load at final failure of the joint by 16% but postpones the event of damage initiation to a 47% higher load.
- The final fracture surface is dominated by failure inside the composite. A decrease in ply thickness from 200µm to 50µm leads, on average, to a decrease in fracture surface from 118% to 99% of initial overlap area.
- A non-linear finite element analysis up to damage initiation indicates no noticeable difference in maximum shear (τ_{xy}) or peel (σ_{yy}) stress inside the adhesive when varying the ply thickness of the composite adherends.
- Adhesive failure is indicated at around 30% of maximum load, always at the interface of the outermost adherend layer to the adhesive, independently from ply thickness.
- Based on Camanho's *3D-invariant based* failure criteria, composite failure is indicated at the same loads as adhesive failure, in case of the THICK configuration and increasing up to 50%, in case of the THIN configuration. The location of composite failure moves from the bond line interface towards the mid thickness of the composite

adherend with decreasing ply thickness, due to the fact, that the *3D-invariant based* criterion takes into account the in-situ effect of ply position and thickness.

- The use of thin plies in composite bonded joints leads to an enhancement of joint strength up to damage initiation but results in a more sudden damage progression till final failure.
- Defining damage resistance of the joint as 1 minus the ratio of average shear stress between damage onset and final failure, the decrease of ply thickness from 200µm to 50µm in this study leads to a decrease in damage resistance of about 61%.

REFERENCES

[4-1] J. Kupski, D. Zarouchas, S. Teixeira de Freitas: *Thin-plies in adhesively bonded carbon fiber reinforced polymers*. Composites Part B, vol. 181, 2020

[4-2] R. Amacher, J. Cugnoni, J. Botsis, L. Sorensen, W. Smith, C. Dransfeld: *Thin ply composites: Experimental characterization and modelingof size-effects.* Compos Sci Technol, vol.101, 121-132, 2014

[4-3] J. Cugnoni, R. Amacher, S. Kohler, J. Brunner, E. Kramer, C. Dransfeld, W. Smith, K. Scobbie, L. Sorensen, J. Botsis: *Towards aerospace grade thin-ply composites: Effect of ply thickness, fiber, matrix and interlayer toughening on strength and damage tolerance*. Composite Science & Technology, vol. 467-477, 2018

[4-4] ASTM-D3039M. *Standard Test Method for Tensile Properties of Polymer Matrix Composite Materials*. West Conshohocken, PA, USA: ASTM International, American Society for Testing and Materials; 2014

[4-5] ASTM-D3518M. *Standard Test Method for In-Plane Shear Response of Polymer Matrix Composite Materials by Tensile Test of a ±45° Laminate.* West Conshohocken, PA, USA: ASTM International, American Society for Testing and Materials; 2013

[4-6] ASTM-D6641M. *Standard Test Method for Compressive Properties of Polymer Matrix Composite Materials Using a Combined Loading Compression Test Fixture.* West Conshohocken, PA, USA: ASTM International, American Society for Testing and Materials; 2014

[4-7] Material datasheet: *Thinpreg™ 135*. NTPT, 2017

[4-8] P. Camanho, C. Dávila, S. Pinho, L. Iannucci, P. Robinson: *Prediction of in situ strengths and matrix cracking in composites under transverse tension and in-plane shear*. Composites Part A, vol. 37, pp. 165–176, 2006

[4-9] Material datasheet: *A75-T-2-0123-1-1*. Airbus Material-Handbook Structure, 2014

[4-10] S. Teixeira de Freitas, J. Sinke: *Failure analysis of adhesively-bonded metal-skin-to-composite-stiffener: Effect of temperature and cyclic loading.* Composite Structures, vol. 166, pp. 27-37, 2017

[4-11] Material datasheet: Scotch-Weld™ Structural Adhesive Film AF 163-2, 3M 2009.

[4-12] K. Kaw: *Mechanics of Composite Materials.* Boca Raton: Taylor & Francis, 2006.

[4-13] ASTM-D5868: *Standard Test Method for Lap Shear Adhesion for Fiber Reinforced Plastic (FRP) Bonding.* West Conshohocken, PA, USA: ASTM International, American Society for Testing and Materials; 2014

[4-14] S. Sihn, R. Kim, K. Kawabe, S. Tsai: *Experimental studies of thin-ply laminated composites.* Composite Science & Technology, vol. 67, pp. 165–176, 2007

[4-15] *Ultraviolet-Ozone Surface treatment.* Three Bond Technical News, 1987

[4-16] J. Poulis: *Small cylindrical adhesive bonds.* PhD thesis, Technical University Delft, The Netherlands, ISBN-90-370-0082-7, pp. 39-62, 1993

[4-17] S. Teixeira de Freitas, D. Zarouchas, J. Poulis: *The use of acoustic emission and composite peel tests to detect weak adhesion in composite structures.* Journal of Adhesion, vol. 94, pp. 743-766, 2018

[4-18] J. Kupski J, S. Teixeira de Freitas, D. Zarouchas, R. Benedictus R, P. Camanho: *Composite layup effect on the failure mechanism of single lap bonded joints.* Composite Structures, vol. 217, pp. 14-26, 2019

[4-19] M. Saeedifar, M. Fotouhi, M. Najafabadi, H. Toudeshky, G. Minak: *Prediction of quasi-static delamination onset and growth in laminated composites by acoustic emission.* Composites: Part B, vol. 85, pp. 113-122, 2016

[4-20] L. da Silva, T. Rodrigues, M. Figueiredo, M. de Moura, J. Chousal: *Effect of Adhesive Type and Thickness on the Lap Shear Strength.* Journal of Adhesion, vol. 82, pp. 1091-1115, 2007

[4-21] P. Camanho, A. Arteiro, A. Melro, G. Catalanotti, M. Vogler: *Three-dimensional invariant-based failure criteria for fibre-reinforced composites.* Int. Journal of Solids & Structures, vol. 55, pp. 92-107, 2015

5 GLOBAL TOPOLOGY CHANGE BY MEANS OF PLY DROPS IN LAMINATED ADHERENDS

This chapter is based on the journal article: J. Kupski, D. Zarouchas, S. Teixeira de Freitas, R. Benedictus: *On the influence of overlap topology on the tensile strength of composite bonded joints: Single overlap versus overlap stacking*. Journal of Adhesion and Adhesives [5-1].

5.1 INTRODUCTION

The previous **Chapter 3** and **Chapter 4** have demonstrated how the two laminate specific design parameters layup and ply thickness are able to enhance the final joint strength and the strength till damage initiation, respectively. However, compared to the reference SLJ design, the increase in joint strength in both cases never exceeded 50%. Aiming for higher values, a more sensitive parameter is needed. As proposed by Shang et al. [5-2] and described in **Chapter 2**, global design parameters, such as overlap length, bond line thickness or fillet design may have a more significant effect on the lap shear strength. Therefore, a change in global topology is expected to lead to further improvement. Compared to a scarf or wavy lap joint, a stepped joint represents a good balance between increase in joint strength and easiness of manufacture, in the context of laminated adherends. Beyond one step, literature shows that, the concept of multiple-stacked overlaps (= finger joints, FJ) through the adherend thickness is well studied as ply-interleaving technique for co-curing dissimilar materials. However, for a secondary bonding process it is so far limited to one stacking level, due to the complexity of the design and manufacturing. Beyond wind turbine and ship building applications with adherend thicknesses > 5mm, FJs have not been studied for secondary bonding of CFRP structures, probably because the thickness of the CFRP laminates in other applications, for example in a commercial *AIRBUS A350-900 XWB* fuselage panel, is often below 5mm [5-3]. Furthermore, the CFRP finger slots can hardly be milled, as common milling tools still suffer enormous deterioration from processing CFRP products [5-4]. These manufacturing issues have so far been hindering further investigation of FJ-topologies for CFRP aircraft fuselage panels.

The aim of this chapter is therefore to explore the manufacturability of these type of joints in thin (< 5mm) CFRP laminates for future application in commercial aircraft structures. The study further aims to investigate whether an increase of overlap length, stacked through the thickness of the laminate, provides increase in tensile joint strength when compared to an increase of overlap length along one bond line of the SLJ-design. The ply-interleaving technique demonstrated in previous work to increase joint strength and decrease the peak peel stress at the tips of the joint region compared to conventional overlap joints. The method was therefore chosen for this study and applied onto a secondary adhesive bonding process on monolithic CFRP adherends with aerospace-grade properties.

5.2 JOINT DESIGN

5.2.1 Topology configurations

Two types of joint topologies were tested: SLJs with two overlap lengths (OL) of 12.7mm and 25.4mm, and FJs with one and two stacked overlaps at a constant overlap length of 12.7mm, see **Figure 5-1**. Specimens were built according to *ASTM 5868-01* [5-5], with a constant width of 25.4mm.

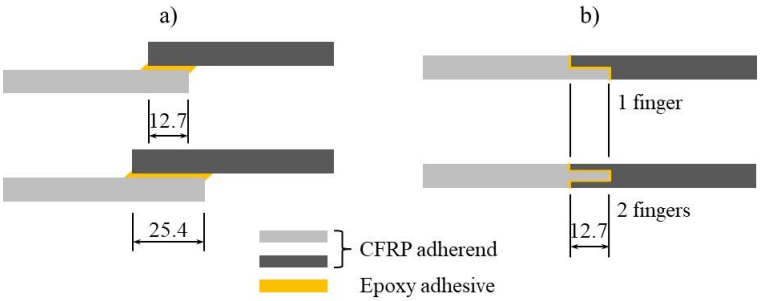

Figure 5-1: a) SLJ-, b) FJ-topology, dimensions in [mm]

5.2.2 Stacking sequence

The composite adherends of these four configurations were manufactured in two cross-ply layups $[(0/90)_s]_4$ and $[(90/0)_s]_4$. **Figure 5-2** is a schematic illustration of the stacking sequence nearby the bond line region, with SLJ-topologies in **Figure 5-2** a) and FJ-topologies in **Figure 5-2** b). The variation in stacking sequence of the adherend has a significant effect on the fracture scenario of composite overlap bonded joints [5-6]. According to previous work from the authors, a cross-ply stacking sequence of $[(90/0)_s]_4$ is expected to trigger the crack inside the composite adherends, whereas the $[(0/90)_s]_4$ with 0° adjacent to the bond line is expected to limit the damage inside the adhesive [5-6]. The composite adherends consisted of 16 UD-layers of 125µm single ply thickness. **Table 5-1** summarizes the total number of design configurations investigated throughout this study.

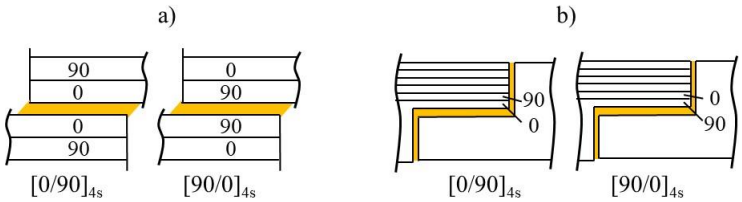

Figure 5-2: Composite layup around the bond line region for the SLJ- a) and FJ-design b) configuration

Design nomenclature	Adherend's layup	overlap length [mm]
SLJ-1-90/0	$[(90/0)_s]_4$	12.7
SLJ-1-0/90	$[(0/90)_s]_4$	12.7
SLJ-2-90/0	$[(90/0)_s]_4$	25.4
SLJ-2-0/90	$[(0/90)_s]_4$	25.4
FJ-1-90/0	$[(90/0)_s]_4$	12.7
FJ-1-0/90	$[(0/90)_s]_4$	12.7
FJ-2-90/0	$[(90/0)_s]_4$	12.7
FJ-2-0/90	$[(0/90)_s]_4$	12.7

Table 5-1: Total number of joint configurations, with nomenclature referring to overlap topology, overlap length and layup

5.2.3 Adherend bending stiffness

The adherend bending stiffness is one of the most significant parameters that influence the peel stresses inside the adhesive bond line [5-6]. Therefore, it is important to keep in mind that the two layup sequences $[(90/0)_s]_4$ and $[(0/90)_s]_4$ provide a slightly different adherend bending stiffness. Based on the classical laminate theory (CLT), the adherend longitudinal bending stiffness was determined as the flexural engineering constant of a laminate given by

$$E_x^f = \frac{12}{D_{11}^* t^3} \qquad (5\text{-}1)$$

for symmetric layups, with D^*_{11} being the first row/first column entry of the resulting inverse of the bending stiffness matrix, t being the overall laminate thickness and x corresponding to the direction along the joint length (longitudinal direction) [5-7]. Layup $[(0/90)_s]_4$ has a longitudinal bending stiffness of 78.95GPa whereas layup $[(90/0)_s]_4$ has 72.70GPa (8.6% lower).

5.2.4 Materials

The materials used for this study were unidirectional (UD) prepreg tapes from carbon fibres and epoxy resin for the composite adherends and an epoxy film adhesive for the bond line. The Prepreg tape was *Hexply® 6376C-HTS (12K)-5-35%* (*HEXCEL Composites Duxford, UK*), containing high tenacity *Tenax®-E HTS45* standard modulus fibres (*TOHO TENAX Europe GmbH*) and the *Hexply® 6376* thermoplastic-toughened epoxy matrix system. The adhesive was *Scotch-Weld™ AF 163-2K* in 293g/m^2 areal weight, including a knit supporting carrier, from *3M Netherlands B.V*. Relevant material parameters, extracted from material datasheet, as well as from previous studies with the chosen adhesive, are presented in **Table 5-2** and **Table 5-3**. **Figure 5-3** shows the considered stress-strain curve for the adhesive *AF163-2K*, taken from previous studies [5-8]. All values are valid at room temperature (23°C). Indices are given for

different coordinate directions with “1”, “2” and “3” standing for the direction along the fiber direction, transverse to the fibers and out-of-plane, respectively.

Longitudinal tensile modulus	E_{11}	142000MPa[a]
Transverse tensile modulus	$E_{22} = E_{33}$	9100MPa[a]
In-plane shear modulus	$G_{12} = G_{13}$	5200MPa[a]
Transverse shear modulus	$G_{23} = E_{33} / (2(1+\nu_{23}))$	3500MPa
In-plane Poisson’s ratio	$\nu_{12} = \nu_{13}$	0.27[b]
Transverse Poisson’s ratio	ν_{23}	0.30[b]

[a] TDS of *F6376 HEXCEL / AIRBUS* [5-9]

[b] adapted from *Hexply-8552/IM7*, Camanho et al. [5-10]

Table 5-2: Adherend material properties

Tensile modulus	E_{Adh}	2046MPa[a]
Poisson’s ratio	ν_{Adh}	0.34[b]

[a] Teixeira et al. [5-8]

[b] TDS of *Scotch-Weld™ AF 163-2K* 293g/m² [5-11]

Table 5-3: Adhesive material properties

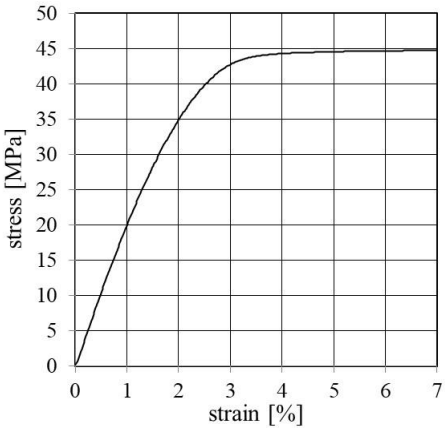

Figure 5-3: Stress-strain curve of *AF 163-2K* 293g/m² [5-8]

5.3 NUMERICAL ANALYSIS

In order to compare SLJ- to FJ-topologies in terms of stress fields surrounding the bond line, a finite element analysis (FEA) was performed with the commercial software *ABAQUS 2017*. A comparison of the stress levels at the bond line, both in shear (τ_{xy}) and peel (σ_{yy}), gives insight on the potential of the FJ-topology, and possible limitations, in comparison with SLJ, since the peak stresses arising at the bond line tips significantly influence the overall joint strength under tensile loading [5-12, 5-13].

5.3.1 Finite element model

Figure 5-4 illustrates the model, including dimensions and boundary conditions. Each composite adherend was modelled with 16 solid elements of type *C3D8* through the thickness, meaning one element per single UD-layer of 125µm. At the right end side, the nodes were fixed in the 3 DoF, while on the left side, solely longitudinal displacement was allowed. Load in x-direction was applied on the left hand-side of the model. This was considered the best choice for the further comparison with the experimental results.

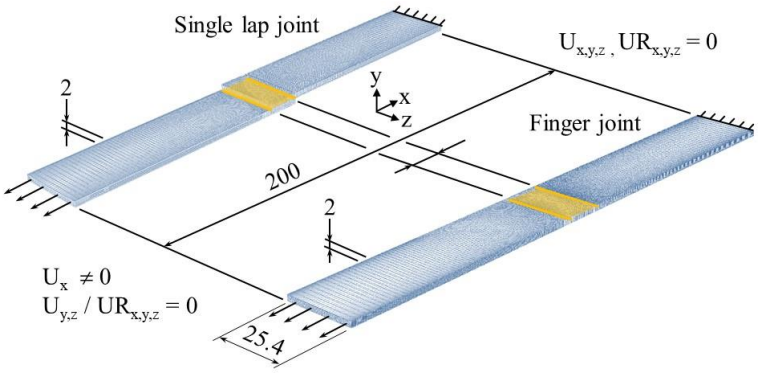

Figure 5-4: 3D FE-model, SLJ design (upper left) and FJ design (lower right) with boundary conditions, dimensions in [mm]

Figure 5-5 shows the mesh at the overlap for the different topologies. Some of the assumption taken in the model, namely in terms of local topology of the bond line, were based on the visual observation of the specimens further detailed in **section 5.4.1**. **Figure 5-5** a) shows the overlap area of the SLJ-1 topology with 12.7mm overlap length. The SLJ-2 topology was modelled accordingly. The spew fillet geometry was modelled as triangular fillet shape of 45°-slope, reaching half the height of the adherend. Taking into account previous experience from the authors [5-6], this shape was considered to be a good approximation to represent a real spew fillet. This was further confirmed in the experimental analysis, see **section 5.4.1**. **Figure 5-5** b) and **Figure 5-5** c) show the overlap region of the FJ-topologies. Rectangular adhesive pockets at the tips of the overlap were created as an approximation of what was observed in reality. In case of the SLJ-topologies, the bond line thickness was modelled with 150µm thickness, following results from previous work of the authors [5-14], whereas in case of the FJ-topologies, it was reduced to 50µm.

For the SLJ, the bond line thickness is modelled with 150µm thickness, following results from previous work of the authors [5-14]. For the FJs, and equivalent adhesive thickness of 150µm would mean that the two adjacent composite plies would either be removed or would become significantly thinner. As this is considered unrealitsic, a 50µm bond line thickness is chosen as a good balance that does not replace a significant amount of the adjacent composite plies and

would still be sufficient to guarantee adhesion between the adherends [5-6].

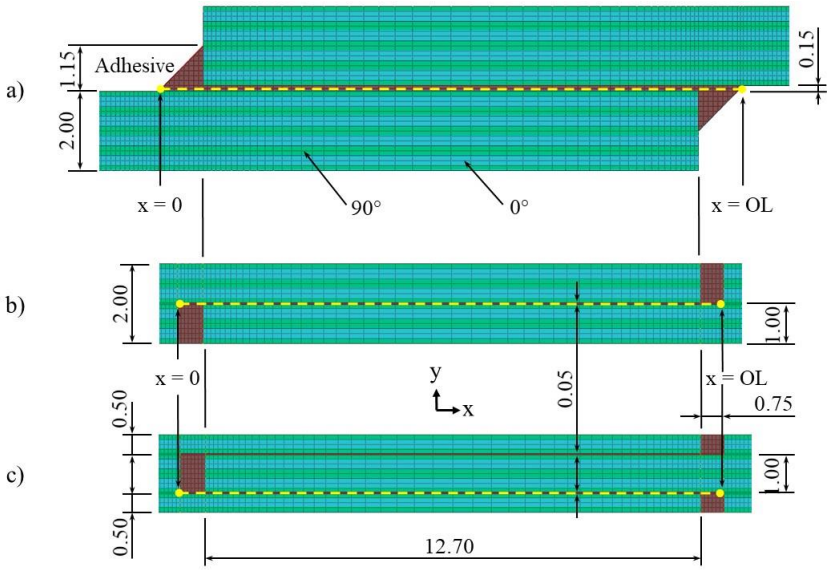

Figure 5-5: 3D FE-model, central joint region, a) for SLJ design with spew fillet, b) for FJ design with 1 overlap, c) for FJ design with 2 overlaps, with layup $[(90/0)_s]_4$ and dimensions in [mm]

In terms of mesh size, the length and width of one element in the overlap tip region was set to 100µm. The element width and length were progressively increased for the regions away from the overlap tip. This results in a maximum element width of 1mm and length of 0.5mm, at the mid-width and mid-length of the overlap, where stresses are lower. The element size towards the adherends free end was further increased for computational efficiency. In terms of thickness, in the adherend, the thickness of one element corresponds to one UD ply thickness, i.e. 125µm. The adhesive layer was modelled with 2 x 75µm through the thickness, in case of the SLJ-configurations and with 2 x 25µm in thickness for the FJ-configurations. The mesh size of 2 element through the thickness of the adhesive is pre-determined, as it represents the smallest practical size with respect to a maximum element aspect ratio of 1:5. This results in a total mesh size of 404,352 elements for topology FJ-1, 449280 elements for FJ-2, 429,184 elements for SLJ-1 and 524,032 elements for SLJ2. A mesh convergence study was performed in order to guarantee that the results are mesh independent. For the mesh size chosen, numerical results were obtained for two types of elements C3D8 (8 nodes, linear interpolation) and C3D20 (20 nodes, quadratic interpolation). A sufficient convergence could be established with element type C3D8. The numerical results were stable (less than 5% difference) between the two mesh types. It is thereby important to note that, the convergence study holds for peel stress along the overlap length of the different configurations. In this case, stresses inside the adhesive do not reach above its yield point so that stresses tie up with the strains. The composite is modelled as linear

elastic, based on the properties listed in **Table 5-3** [5-8, 5-11], while the adhesive is modelled following the stress-strain curve obtained from tensile dog-bone tests, as shown in **Figure 5-3**. The stress –strain curve includes both elastic and plastic behaviour of the adhesive material. Within this study, there are no plasticity model nor yield criteria used. The material is modelled as elastic-plastic, with 4 data points defining the stress-strain curve in the plastic regime, beginning at 25.3 MPa yield stress, and including isotropic hardening. At the pre-defined load of 1.5 kN most configurations show no plastic strain, except for one case, FJ-1-0/90, which reaches a stress peak for in-plane tensile stress above the yield point of the adhesive of 25.3 MPa. The load is applied in a single step taking into account non-linear geometry effects.

5.3.2 Parametric study

With the presented non-linear 3D finite element model, it is possible to explore FJ-topologies with a larger number of fingers. **Figure 5-6** shows the results of the parametric study of 4 topologies with increasing number of fingers: 1, 2, 3 and 7, using the layup $[(0/90)_s]_4$ as an example. The particular number of fingers is a consequence of the need for a balanced layup in each finger, containing at least 4 layers of 125µm UD-ply thickness. **Figure 5-6** presents the peel stress (σ_{yy}) distribution at the mid-thickness of the adhesiver along the overlap length, as this out-of-plane stress component plays the major role for damage initiation in the joint [5-12, 5-13]. The plot focusses on the first 2mm (in x-direction) from the left tip of the overlap. The FJ-1 topology has the highest peak peel stress of all configurations. With increasing number of fingers, the peak peel stress decreases, with a noticeable drop of 51%, from 7.62MPa to 3.72MPa between the topologies FJ-1 and FJ-2. The difference between the topologies with 2 (3.72MPa), 3 (3.23MPa) and 7 (2.61MPa) overlaps is less significant with an average of 16%. The load is chosen to 1.5kN in the parametric study.

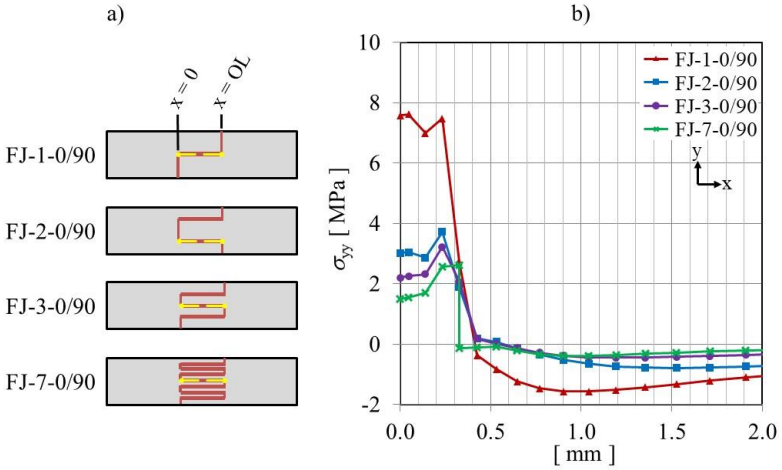

Figure 5-6: Peel stress distribution along bond line length on FJ-topologies with 1, 2, 3 and 7 stacked overlaps with layup $[(0/90)_s]_4$

The parametric study of **Figure 5-6** intends to demonstrate the potential in stress reduction for joint designs with more than 1 overlap. The peel stress for FJ-2, FJ-3 and FJ-7 are plotted for the finger closer in terms of thickness to the location of FJ-1. However, for the remaining fingers of FJ-2, FJ-3 and FJ-7, the peak peel stress values are within the same range and all with significantly lower values than FJ-1. As a result of the parametric study it can be stated, that at least two fingers are needed to significantly decrease the peak peel stress at the bond line tip. The FJ-2-topology benefits from avoiding the eccentricity and from symmetric stress distribution, while for the FJ-1-topology the beneficial effect of avoiding eccentricity is outperformed by the detrimental effect of stiffness reduction at the overlap region, when comparing with the SLJ configuration. For more than 2 fingers, ie, FJ-3 and FJ-7, there is less significant stress reduction.
The general trend of all plots in **Figure 5-6** follows the common "bathtub curve" for SLJs, with stress peaks (in shear, peel and tensile) at the tip of the overlap region. This would explain the general plateau of the peel stress beyond x=0.5mm. An explanation could be, that the plateau coincides with the adhesive butt between the two composite adherends. As the stiffness is reduced in the region, the load transfer would reduce, too. However, the length of one butt is set 0.75mm, while the significant drop in peel stress in **Figure 5-6** is around 0.3mm, which means around the center of the butt (in x-direction) The drop in peel stress would therefore be expected closer to one of the two interfaces in the plot path, at x = 0mm and x = 0.75mm. Apparently, the total available overlap area in the FJ-2-design is sufficient to avoid large stress peaks. A load transfer over more than 2 fingers would still increase the total overlap area and therefore result in further decrease of peak peel stress, but less significantly, in context with the given joint overlap length, width and adherend thickness. A similar observation is stated in literature [5-12], when comparing joint strength of SLJs with increasing overlap length: at a certain threshold, the joint strength does not increase further with the increase in overlap length.
Based on these results, it is decided to focus the study on the two topologies with 1 finger and 2 fingers. Although the FJ-2-topology shows a potential for decreasing the peak peel stresses, one should also take into account the level of complexity that multiple fingers require, in terms of manufacturing and surface preparation prior to the secondary bonding process.

5.3.3 Stress field at the bond line region

Figure 5-7 and **Figure 5-8** present the shear (τ_{xy}) and peel (σ_{yy}) stress distribution along the mid-thickness of the bond line length for both layup configurations $[(0/90)_s]_4$ and $[(90/0)_s]_4$ at a pre-defined load of 1.5kN. All plots are taken at mid-width position and cover half of the bond line length. In order to compare joint topologies of different overlap lengths, the x-axis is normalized to the full overlap length (OL). The paths along which the stresses are taken, are highlighted in **Figure 5-5** for all topologies. The stresses at the mid-adhesive are considered representative, as shear and peel stress do not vary significantly through the thickness of the adhesive, in comparison with the stress variation along the overlap.

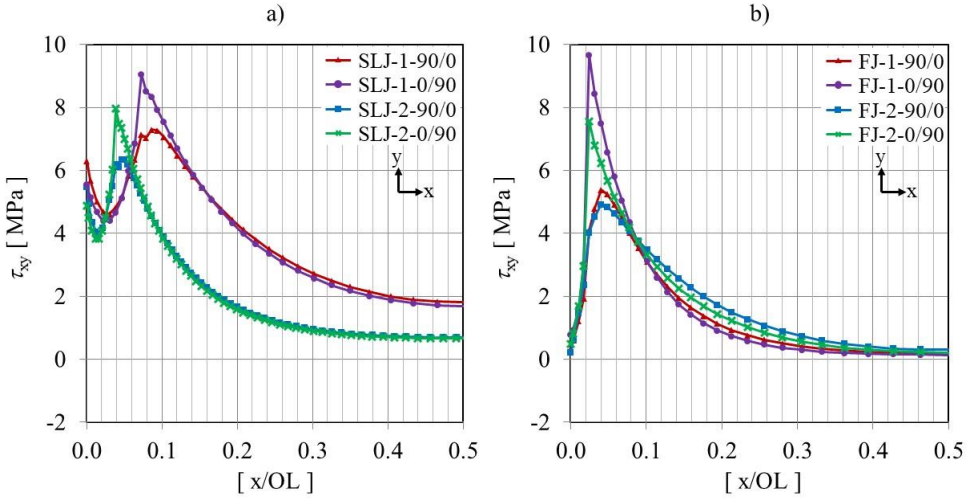

Figure 5-7: Shear stress (τ_{xy},) distribution inside the adhesive along 1/2 overlap length (OL), a) for SLJ-topologies, b) for FJ-topologies

The oscillatory behaviour of the shear stress in SLJs close to the bond line tips shown in **Figure 5-7** a) is a result of the spew fillet: the plotted stresses start just outside the actual overlap, at the end of the spew, where the lower tip of the triangle touches the lower adherend, see **Figure 5-5** a), x=0. Here is the first stress peak. The second stress peak occurs when the actual overlap starts, and the upper tip of the triangle touches the upper adherend. A shift of these peaks between the different SLJs results from the different overlap lengths. So, in fact all SLJ-configurations suffer a first stress peak at the lower end of the spew fillet and a second, higher stress peak, at the upper end of the spew fillet. In case of the finger joints, the spew fillet is replaced by a shorter resin pocket, see **Figure 5-5** b),c). No oscillatory behaviour appears and with constant overlap length for all FJ configurations, the peaks show up at the same location along the x-axis.

The layup 0/90 always results in higher peak shear stresses in the adhesive than 90/0. This is in accordance with previous work of the authors [5-6], who found that an interface ply angle of 0° results in the highest shear stresses in the adhesive bond line. As the ply angle increases, the stiffness of the ply interface decreases and the shear stress inside the adhesive decreases as a consequence. From SLJ 1 to SLJ 2 and from FJ-1 to FJ-2, the peak shear stresses decrease. So, a larger overlap area decreases the peak shear stress in the adhesive in all cases.

There is no overall trend of peak shear stresses in the adhesive when comparing the two different topologies with the same layup and bonded area (plots with the same colour in a) and b)). The peak shear stress decreases by 26% from SLJ-1-90/0 (7.29MPa) to FJ-1-90/0 (5.37MPa), and by 23% from SLJ-2-90/0 (6.35MPa) to FJ-2-90/0 (4.92MPa). But the peak shear stress increases by 7% from SLJ-1-0/90 (9.06MPa) to FJ-1-0/90 (9.67MPa), and decreases by just 5% from SLJ-2-0/90 (7.95MPa) to FJ-2 0/90 (7.54MPa).

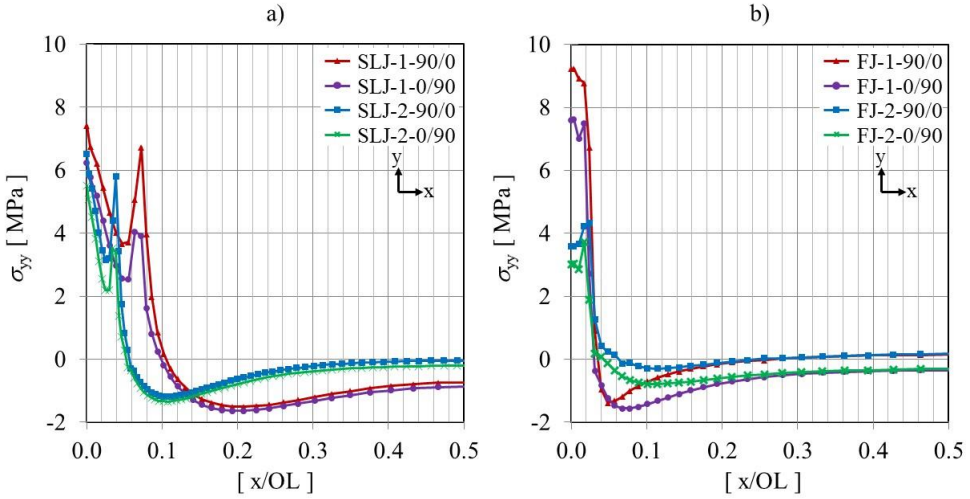

Figure 5-8: Peel stress (σ_{yy}) distribution inside the adhesive along 1/2 overlap length (OL), a) for SLJ-topologies, b) for FJ-topologies

In **Figure 5-8**, FJ-1 results in the highest peak peel stresses at the bond line tips. It is therefore the topology that will most likely promote early delamination in the composite adherends. FJ-2 results in the lowest peak peel stress at the bond line tips. It is consequently expected to be a promising topology to delay delamination in the composite adherend and increase the strength of the bonded joint. SLJ-1 and SLJ-2 result in similar peak peel stress at the bond line tips. These values lie between the FJ-1 and FJ-2. In case of the FJ-2 configurations, the peel and shear stress distribution in both overlaps are very similar.

The change from FJ to SLJ has two conflicting effects on the stress field at the overlap. On one hand, by elimating the eccentricity between the adherends from SLJ to FJ, the detrimental secondary bending moment at the overlap is eliminated. This leads to a smaller rotation of the joint and a decrease in peel stresses, at the bond line tip. On the other hand, the stiffness of the adherend at the overlap region is reduced from full adherend thickness in the SLJ- to half adherend thickness in the FJ-topology. This reduction in tensile and bending stiffness at the overlap area leads to higher local deformation causing an increase in peel stresses.

Therefore, for the FJ-1-topology the beneficial effect of avoiding eccentricity is outperformed by the detrimental effect of stiffness reduction, so that the peak peel stress is higher in this topology than in the SLJ-configurations. For the FJ-2-topology, the scenario changes significantly. In this case the FJ-2-topology outreaches the SLJ-topologies. The peak shear stress decreases by 23%, from SLJ-2-90/0 (6.35MPa) to FJ-2-90/0 (4.92MPa) and the peak peel stress by 33% from SLJ-2-90/0 (6.51MPa) to FJ-2-90/0 (4.34MPa). Furthermore, it is intereresting to note that in terms of layup, $[(0/90)_s]_4$ results in higher peak shear stress but lower peak peel stress when compared to $[(90/0)_s]_4$. This is in accordance with previous studies of the authors [5-6], which found that an interface ply of 0° in contact with the adhesive results in high shear but low peel stress - as a result of the increased bending stiffness of the 0/90 configuration -

inside the bond line, causing the joint to fail cohesively. To summarize, **Table 5-4** presents peak shear ($\tau_{xy,max}$) and peel ($\sigma_{yy,max}$) stress inside the adhesive, that are derived from the numerical 3D FE model along the bond line length, as well as the peel-to-shear ratio of those. The peel stress, as an out-of-plane stress, causes a mode-I crack opening mode, which requires the lowest amount of energy for a crack to propagate [5-13]. Therefore, it is of great interest to achieve a low peel-to-shear ratio.

	Peak shear stress	Peak peel stress	Peak mode ratio	Peak tensile stress in butt region
	$\tau_{xy,max}$ [MPa]	$\sigma_{yy,max}$ [MPa]	$\sigma_{yy,max}/\tau_{xy,max}$ [-]	$\sigma_{xx,max}$ [MPa]
SLJ-1-90/0	7.29	7.42	1.02	
SLJ-1-0/90	9.06	6.23	0.69	
SLJ-2-90/0	6.35	6.51	1.03	
SLJ-2-0/90	7.95	5.50	0.69	
FJ-1-90/0	5.37	9.45	1.76	24.3
FJ-1-0/90	9.67	7.77	0.80	28.1
FJ-2-90/0	4.92	4.34	0.88	10.0
FJ-2-0/90	7.54	3.72	0.49	10.4

Table 5-4: Peak shear ($\tau_{xy,max}$), peel ($\sigma_{yy,max}$), peel-to-shear ratio ($\sigma_{yy,max}/\tau_{xy,max}$) for all configurations and peak tensile ($\sigma_{xx,max}$) stresses in the butt region for FJ-configurations

In the FJ-configurations, the vertical butt joints are modelled with the same isotropic adhesive material properties as the flat overlaps, see **Figure 5-5** b),c). So, they represent a very ductile gap-filler, which is perfectly connected to the adjacent CFRP layers. However, at this location the adhesive suffers from in-plane tensile stresses, as in a butt joint, which could be critical for the failure initiation of the FJ-configurations. It is therefore important to have a closer look onto these in-plane tensile stresses at the butt joints.

Figure 5-9 shows the in-plane tensile stress at the butt joints for the FJ-topologies. The stresses are plotted at the interface between adhesive and adherend (in x-direction) where stresses are found to be highest, from bottom of the adherend till the center (in y-direction) and at mid-width (in z-direction). When comparing the values for τ_{xy} and σ_{yy} in **Figure 5-7** b) and **Figure 5-8** b) with σ_{xx} in **Figure 5-9** b), it is observed that for FJs the in-plane tensile stresses at the butt joints are the most critical rather than the peel stresses in the overlaps. For the FJ-1-configurations,

FJ-1-90/0 has 24.3MPa in σ_{xx}, compared to 5.37MPa in τ_{xy} and 9.45MPa in σ_{yy} and FJ-1-0/90 has 28.1MPa in σ_{xx}, compared to 9.67MPa in τ_{xy} and 7.77MPa in σ_{yy}. For the FJ-2-configurations, FJ-2-90/0 has 10.0MPa in σ_{xx}, compared to 4.92MPa in τ_{xy} and 4.34MPa in σ_{yy} and FJ-2-0/90 has 10.4MPa in σ_{xx}, compared to 7.54MPa in τ_{xy} and 3.72MPa in σ_{yy}. All numbers are summarized in **Table 5-4**.

Two more observations can be made from **Figure 5-9**: 1) The in-plane tensile stresses at the butt joints in FJ-1 configurations show an oscillatory behavior, which results from layup orientation: Higher tensile stresses inside the adhesive at the adhesive-adherend interface are aligned with the fiber-dominated stiffness of a 0°-ply and lower tensile stresses are aligned with the matrix-driven stiffness of a 90°-ply. This is a complementary finding to previous conclusions from the authors, stating that 0° as an interface ply in a SLJ-configuration results in the highest shear stresses inside the adhesive [5-6]. 2) It is interesting to note that the tensile stresses σ_{xx} at the mid adherend thickness converge to the same value for both configuration FJ-1 and FJ-2, around 10MPa. This could be related to what is found in the parametric study presented in **Figure 5-6** of previous **section 5.3.2**. At the mid adherend thickness, the tensile stress level inside the FJ-topologies may reach a plateau, independent from layup and number of overlaps.

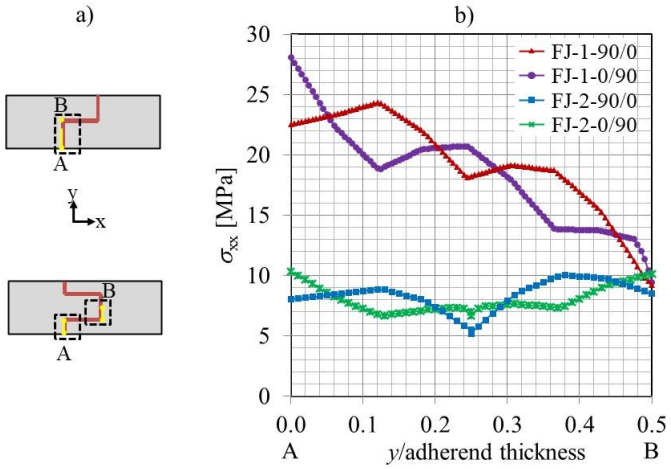

Figure 5-9: Longitudinal tensile stress distribution, plotted at the outside interface between adhesive butt joint and adherend, from bottom till center of the adherend

It is well known [5-12] that an increase of overlap length in a SLJ does not decrease peak stresses in peel and shear by the same amount, which is in agreement with the observations in **Figure 5-7** a) and **Figure 5-8** a) on the SLJ-configurations. This law of diminishing returns has to do with the load transfer in a SLJ and relates to the length of the overlap, but not the overlap area. So, with 2 bond lines in FJ-2, which is the same bond line length as in FJ-1, the shear stress is expected to cut in half. However, by looking at **Figure 5-9**, this is not the case. Assuming that any load transmitted across the butts is removed from the overlap region, the load in the FJ-1 transmitted by the butts is higher than in the FJ-2 configuration. Consequently, the overlap in the FJ-1 has to carry less remaining load than in the FJ-2. It can be stated that in practice the

butts will fail first, as the in-plane tensile stresses, seen in **Figure 5-9**, are higher than the peel and shear stresses. Therefore, the joint performance should be linked to the butt stresses instead of the overlap stresses, which is also in agreement with previous work on multi-stepped lap joints of Adams et al. [5-15], as reported in **section 2.2.4**. Taking into account this stress analysis, it is expected that the difference in lap shear strength follows the trend that is observed in the stress analysis, meaning that FJ-2 would outperform the SLJs in maximum load, while the topology with 1 finger (FJ-1) would reach lower maximum load than the SLJs. Those joint topologies with layup $[(0/90)_s]_4$ are expected to fail cohesively inside the adhesive, when compared to layup $[(90/0)_s]_4$, as the higher stiffness of the adjacent layer would trigger a crack to propagate inside the adhesive [5-6].

5.4 EXPERIMENTAL ANALYSIS

In the previous section, the stress analysis showed a potential for finger joint topologies, from 2 fingers onwards, to decrease peel stress at the tip of the bond line. Consequently, the question could be raised, if this observation is only valid for the linear-elastic region below the load where the damage initiates. How will the topology and the layup affect the damage resistance of the joint and the joint strength till final failure? An experimental campaign can help validate the linear-elastic model and can give more insights into the damage evolution inside the joint beyond damage initiation. Furthermore, since the finger joint topology is known to be fairly complex in terms of manufacturing, an experimental campaign can also prove or disprove its feasibility.

5.4.1 Specimen manufacturing

In order to create lap shear specimens according to *ASTM 5868-01*, adherends were laminated in a Prepreg hand layup process, with 15min of de-bulking at an under pressure lower than 100mbar. As recommended by the manufacturer of the chosen Prepreg system *Hexply® 6376C-HTS (12K)-5-35%*, the preform was debulked after every fourth layer, before curing inside the autoclave [5-9]. The laminates were placed between a base plate of 12mm thickness and a caul plate of 2mm thickness from aluminium. **Figure 5-10** illustrates the sequence for manufacturing the specimen. In order to minimize resin flow-out along the edges of the laminate, an aluminium barrier was added during the autoclave curing cycle.

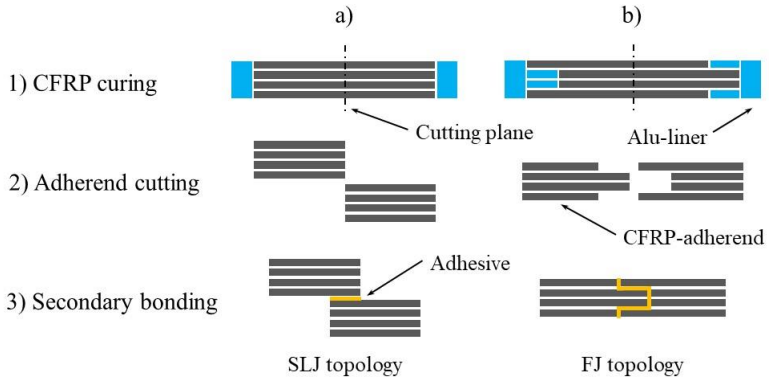

Figure 5-10: Manufacturing sequence for a SLJ-, a), and a FJ-topology with 2 fingers, b), with integrated aluminium liners (in blue)

Figure 5-11, below, shows a close-up of the aluminium liner, which was placed at the edge of the laminate during the layup process. The sheet mimics the thickness of 4 cured layers (4x 125µm = 500µm) and both its upper and lower side were carefully grinded to reach a repeatable surface roughness of 10µm (hand-held rotational grinding machine with grain size 80/180/240, 2min each with constant movement in 0/90°-direction). In addition to the liner, a Teflon coated release foil was added to the layup, in order to improve release ability. The thickness of the release foil of 50µm was taken into account for the creation of fingers. The autoclave curing process comprises a single dwell step at 177°C and 7bar gauge pressure, with 800mbar underpressure inside the vacuum bag for 120min time.

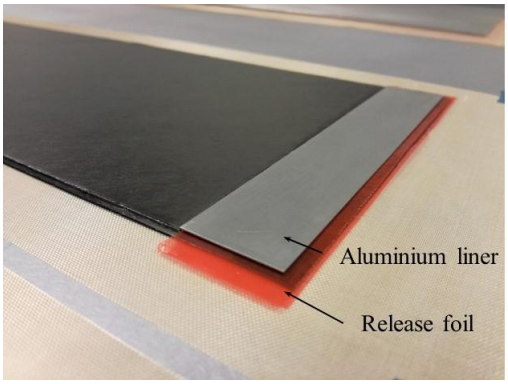

Figure 5-11: Laminating CFRP plate for FJ-2-90/0 (2 fingers with layup $[(90/0)_s]_4$) with integrated aluminium liners and release foil

Thereafter, a secondary adhesive bonding process was performed by laying the uncured film adhesive onto the cured adherends and arranging a vacuum setup around them. A surface treatment was applied to the CFRP surface which consists of the following procedure: (1)

degreasing the surface with Acetone, (2) manual grinding with *3M's Scotch Bride™*, (3) cleaning with Acetone, and (4) 7min UV/ozone treatment [5-16, 5-17]. Previous studies have shown that this surface treatment results in good wettability of the CFRP surfaces [5-18]. The secondary bonding process was performed in the autoclave at 2bar gauge pressure and 120°C curing temperature for 90min dwell time, while venting the vacuum bag to full atmosphere.
The assembly of the FJ-2 topologies needs special care, in order to avoid any disruption of the film adhesive. Spreading clamps were used to open the embracing adherend side lightly (right adherend in **Figure 5-1** b) at FJ-2). This was done with care, to prevent accidental crack initiation inside the joint by excessive spreading.

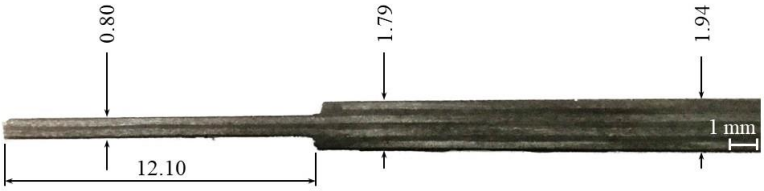

Figure 5-12: Variation in layup thickness at the overlap region of finger joint with 2 fingers (FJ-2-) and layup $[(90/0)_s]_4$ prior to bonding, under optical microscope with 1x magnification, dimensions in [mm]

After curing, adherends of the SLJ-designs had a consistent thickness of 2.0mm (+/- 0.1mm) of the CFRP laminate and 0.15mm (+/- 0.10mm) of the bond line. In case of the FJ-specimens, the average thickness of the laminate at the overlap region decreased at the joint region by 23% (from 2.15mm mm to 1.65mm) in the $[(90/0)_s]_4$ layup and by 15% (from 2.07mm to 1.75mm) in the $[(0/90)_s]_4$ layup. **Figure 5-12** illustrates the overlap region of the CFRP adherend of a FJ-2-90/0 design prior to bonding. There is a noticeable decrease in cured laminate thickness from the center of the adherend (right side) towards the interleaving fingers (left side). The laminate thickness of the finger with layup $[(90/0)_s]_4$ decreases to 0.8mm, instead of the expected nominal value of 1.0mm. This effect is caused by a significant amount of resin flow-out during the fabrication of the adherends. A zone of decreased laminate thickness is visible along all surrounding edges of the CFRP-plates. This flow-out zone has a width of 40mm, measured from the plate edge towards the center of the plate. Resin flow barriers were used to contain all resin at the edges. However, a decrease in total adhered thickness of 8%, from 1.94mm to 1.79mm, is observed in **Figure 5-12**. This resin flow-out would promote higher fiber volume content at the edge of the specimen, which consequently results in a change in material properties. **Figure 5-13** shows the same FJ-2-0/90-configuration as in the previous **Figure 5-12**, after the secondary bonding process. Fiber undulations developed in the vincinity of the finger dent. Steps between different plies are visible near the bond line region, giving shape to the right side of the adhesive pocket in **Figure 5-13** b). All thickness values were measured with a digital micrometer with an accuracy of 1μm, while the overlap length was measured with a digital caliper of accuracy 10μm.

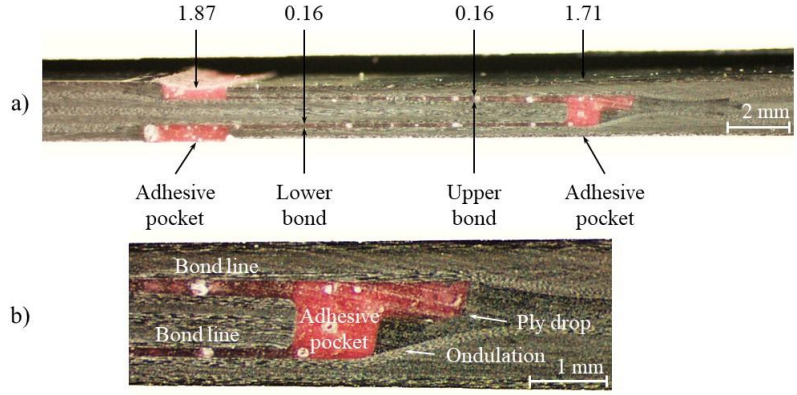

Figure 5-13: a) Overlap region of FJ-2-0/90 after bonding, dimensions in [mm] and b) zoom in of the right-hand side adhesive pocket

Figure 5-14 shows typical examples of specimens of the other topologies studied, the SLJ-1 in **Figure 5-14** a) and the FJ-1 in **Figure 5-14** b). Compared to the FJ-2-topologies presented above, the FJ-1 topologies exhibit less of the observed manufacturing flaws due to the lower complexity of the joint topology and the SLJ-topologies show no noticeable manufacturing flaws at all.

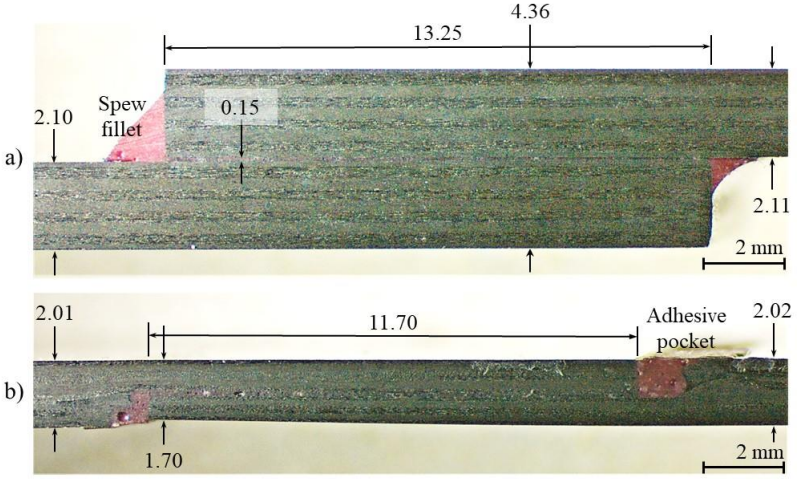

Figure 5-14: Overlap region of a) SLJ-1-90/0, and b) FJ-1-0/90, after bonding, dimensions in [mm]

A surface analysis using contact angle measurements was performed to the pre-treated CFRP surfaces to assess their wettability. The contact angle of a 4µl distilled water drop was measured, having a topology imprint from the aluminium base and caul plate with 10µm surface roughness, using the *Technex Cam200/Attension Theta V4.1.9.8* system. The combined surface treatment of Acetone degreasing and exposure to UV-light in an ozone-containing atmosphere reduces the

value of the contact angle by 78%, from 91° (± 3°), before treatment, to 20° (± 1°), after treatment, for the SLJ design configuration. Due to poor surface accessability in case of the FJ design configurations, the value of the contact angle reduced only 54%, from 76° (± 4°), before treatment, to 35° (± 5°), after treatment. Nevertheless, the contact angle values after pre-treatment are in accordance with literature and correspond to a sufficient wettability of the surface [5-18].

5.4.2 Experimental setup

Five specimens per design configuration were subjected to quasi-static tensile loading. The tests were performed under displacement control with a constant displacement rate of 1.3mm/min, according to the given test procedure [5-5]. The tests were performed on a *Zwick-Roell AllroundLine Z250 SW* testing machine with a load cell of 250kN.

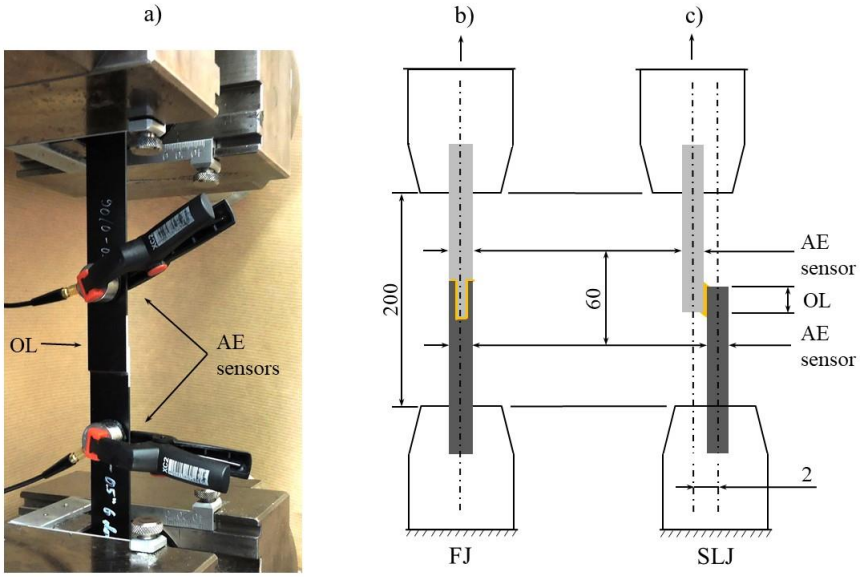

Figure 5-15: Experimental test setup (a), and schematic illustration for FJ- (b), and SLJ-joint topology with clamping offset (c) (dimensions in [mm])

Figure 5-15 shows a schematic illustration of the test set up. Specimens were clamped at the ends by two clamps at 250bar hydraulic pressure. The initial distance of the clamps was set to 200mm. For the SLJ-configurations, the clamps were set to a misalignment of 2mm to counterbalance the overlap offset. For the FJ-configurations no offset was needed. Beyond recording the load and displacement from the testing machine, an AE-system by *Vallen Systeme GmbH* was employed, consisting of two *VS900-M* sensors, to monitor the acoustic emission activity during the tests. The AE-system was connected to the load cell of the test frame in order to synchronize the AE-activity with the load measurements. The AE-sensors were attached onto

the same side of the specimen at ± 30mm from the overlap centre and connected to an *AEP4H 34dB* amplifier.

5.4.3 Load-displacement results

Figure 5-16 shows the representative load-displacement curves for each topology configuration. **Figure 5-16** a) shows the four configurations with SLJ-topologies, while **Figure 5-16** b) presents the configurations with the FJ-topologies. In **Figure 5-16** a), the SLJ2-0/90 reaches significantly higher ultimate load than the other three topologies. In **Figure 5-16** b), the FJ-2-90/0, unlike any other configuration, is able to carry load after the first load drop at 1.5mm displacement and reaches its ultimate load of 16.5kN at a displacement of 2.5mm. All plots show a similar initial slope and, except for the FJ-2-90/0 in **Figure 5-16** b), a sudden final failure. The FJ-2-90/0 presents a load drop and subsequent increase on the load-displacement response. This is representative of all 5 specimens tested of this configuration.

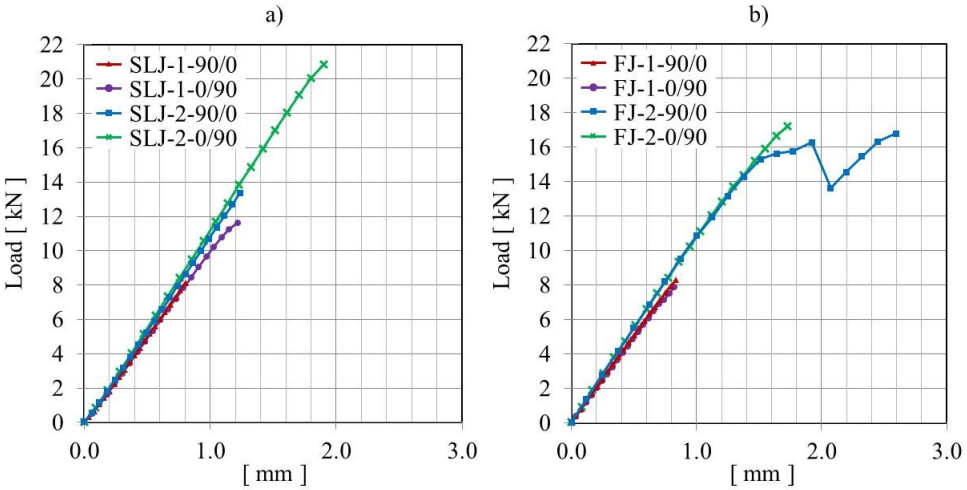

Figure 5-16: Load-displacement curves, a) with SLJ-topologies, b) with FJ-topologies

Table 5-5 presents the average maximum load and corresponding displacement for each configuration. In average, the maximum load ranges from 7.10kN for the SLJ-1 $[(90/0)_s]_4$ to 20.03kN for the SLJ-2 configuration with $[(0/90)_s]_4$ layup. The work in the load-displacement curves allows a comparison of average energy until failure for the different configurations, by determining the area under the load-displacement curves. The results are presented in **Table 5-5**, ranging from minimum 2.88 (±0.86) times 10^6J for the SLJ-1-90/0 to maximum 17.98 (± 1.66) times 10^6J for the SLJ-2-0/90 type.

It can be seen from the load-displacement curves of **Figure 5-16**, that the joint stiffness of different configurations is in close range. The SLJs in **Figure 5-16** a) show a 6% higher average joint stiffness of 10.7kN/mm compared to the FJs with 10.1kN/mm average joint stiffness in **Figure 5-16** b).

The last colum in **Table 5-5** presents the average load at damage initiation for each joint configuration. AE-technique is used to monitor the damage events during the experimental campaign. A sudden increase of AE-energy is chosen as indicator for damage initiation, as follows:

$$E^{AE}_{i} > 10^{-13}\text{J} \quad \text{AND} \quad E^{AE}_{i+1} \leq 10^{-8}\text{J} \quad (5\text{-}2),$$

with E^{AE} being the acoustic energy per hit (i). Damage initiation is believed to cause a significant increase in AE-energy. But it is not clear a priori, what would be the threshold in absolute numbers, as for each test-campaign the AE-signal depends from the Young's Modulus and density of the chosen materials in the specimen. Therefore, AE-data were evaluated in 3 steps:

1) Exclude any AE-activity in the first 10% of maximum load, due to clamping, specimen rectification or other machine setup noise at the beginning of the test.
2) Neglect AE-activity at the very end of the load displacement curves. Based on previous work, it is assumed, that damage initiation for this specific set of adherend/adhesive SLJ, is expected to happen below 90% of maximum load [5-6].
3) For the remaining data, find the largest increase in AE-energy, for both sensors. Comparing this largest increase factor in all specimens, find a common multiple over all cases.

In all cases, loads at damage initiation are well below final failure, at most 30% in case of FJ-2-90/0, minimum at 10% in case of the SLJ-2-0/90 and in average at 21% of the maximum load.

	Maximum load	Displacement at maximum load	Strain energy	Load at damage initiation
	F_{max} [kN]	d [mm]	W [10^6 J]	F_{init} [kN]
SLJ-1-90/0	7.10 (±0.73)	0.71 (±0.08)	2.88 (±0.86)	1.95 (±0.54)
SLJ-1-0/90	11.17 (±0.41)	1.18 (±0.08)	6.55 (±0.55)	2.25 (±0.12)
SLJ-2-90/0	12.57 (±0.62)	1.17 (±0.05)	7.50 (±0.67)	3.03 (±0.60)
SLJ-2-0/90	20.03 (±0.84)	1.79 (±0.11)	17.98 (±1.66)	2.08 (±0.41)
FJ-1-90/0	7.99 (±0.35)	0.82 (±0.02)	3.20 (±0.14)	1.20 (±0.07)
FJ-1-0/90	8.45 (±0.75)	0.89 (±0.11)	3.68 (±0.73)	1.56 (±0.36)
FJ-2-90/0	15.88 (±1.29)	2.48 (±0.39)	14.13 (±3.27)	4.78 (±0.41)
FJ-2-0/90	15.24 (±2.28)	1.49 (±0.25)	11.23 (±3.06)	2.82 (±0.83)

Table 5-5: Load at damage initiation [kN], maximum load [kN], displacement at maximum load [mm] and strain energy [10^6J]

For the parametric study, the mesh convergence and the stress analysis, a consistent design load of 1.524kN (30MPa surface traction x 2mm specimen height x 25.4mm specimen width) was

chosen. On the crosshead of the tensile machine, the maximum load was measured 7.099kN mean value over 5 specimens for the weakest configuration, SLJ-90/0 with 12.7mm overlap length. Comparing these two, the numerical design load can then be described as 1.524 / 7.099 = 21.47% of average maximum load of the weakest configuration. The load of damage initiation, indicated by Acoustic Emission technique in **Table 5-5**, is in all cases well below final failure, at most 30% in case of FJ-2-90/0, minimum at 10% in case of the SLJ-2-0/90 and in average at 21% of the maximum load. The numerical design load lies below the experimental damage initiation load in most configurations, except for one case, FJ-1-0/90, which was indicated with a very low damage initiation load at 1.2kN average. With design load of 1.5kN in the models, most configurations did not show any plastic strain, except for one case, FJ-1-0/90, which reached an in-plane tensile stress of 28.1MPa, which lies above the yield point of the adhesive of 25.3MPa, see **Figure 5-9**.

5.4.4 Fracture surfaces

Figure 5-17 shows the typical fracture surfaces for the four SLJ-topology configurations. The SLJ topologies SLJ-1-90/0 and SLJ-2-90/0 in **Figure 5-17** a) and c), show interlaminar failure inside the composite, between the first (90°) and second layer (0°) and no trace of cracks propagating throught the adhesive bond line. In the case of SLJ-2-90/0, the crack splits up at ca. 40% of overlap length and jumps perpendicular to the bond line thickness until reaching between the first (90°) and second (0°) layer of the opposite adherend again. The SLJ-1-0/90 configuration in **Figure 5-17** b) results in a mixed fracture surface with a crack partly propagating through the adhesive and partly along the first layer (0°) (intraply failure) adjacent to the bond line. For the SLJ-2-0/90 in **Figure 5-17** d) cohesive failure inside the adhesive is mostly observed. **Figure 5-18** shows the typical fracture surfaces for the FJ-topology. The first three configurations in **Figure 18** a) - c) show a failure pattern with interlaminar failure inside the composite. The crack is believed to initiate at the interface between first (90°) and second layer (0°) away from the bond line. This is however not the case for FJ-1-0/90 (b), where apparently fibre fracture of the first (0°) layer has occurred. In **Figure 5-18** d), crack paths are observed on both embracing fingers as a mix of interlaminar failure between the first (0°) and the second (90°) outside layer and intralaminar failure inside the most outside (0°) layer.
The failure pattern in **Figure 5-18** would be in good agreement with observations of Ahamed et al. [5-19], who investigated the ply-interleaving technique for joining dissimilar composite materials, using combined experimental, analytical and numerical methods. They stated that joint failure is caused by delamination at the location where plies terminate, as well as by transverse matrix cracking within off-axis plies. Overall, all configurations with layup $[(90/0)_s]_4$, exhibit final fracture surface inside the composite. FJ-topologies with layup $[(0/90)_s]_4$ fail inside the composite, while SLJ-designs of the same layup fail inside the adhesive.

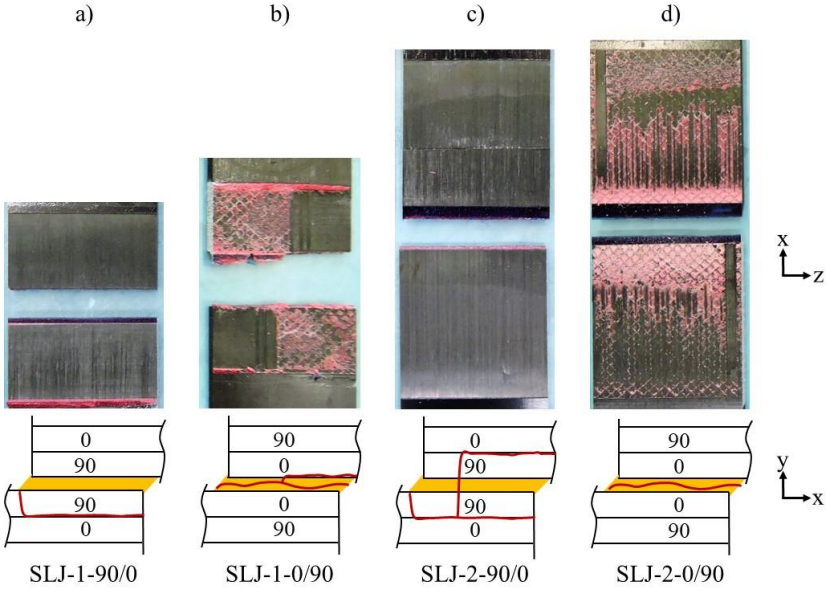

Figure 5-17: Final fracture surfaces of SLJ-topologies with layup $[(90/0)_s]_4$ (a and c) and layup $[(0/90)_s]_4$ (b and d)

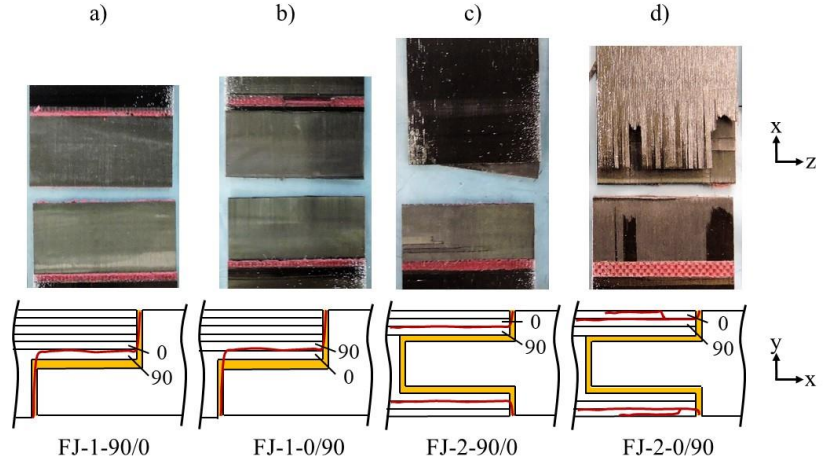

Figure 5-18: Final fracture surfaces of FJ-topologies with layup $[(90/0)_s]_4$ (a and c) and layup $[(0/90)_s]_4$ (b and d)

Post-mortem fracture surface analysis was performed using the *Keyence VR5000* wide-area 3D profiling system. This surface analysis indicates in which ply the failure inside the composite adherend occurs and, as a consequence, if it is intra- or interply failure. This information enables to draw the crack profiles, presented in **Figure 5-19** and **Figure 5-20**. **Figure 5-19** shows as an example the top adherend side of a typical SLJ-1 configuration in layup $[(0/90)_s]_4$. The final

fracture surface is presented as a 3D profile. A cross section profile along the length of the overlap is also shown below the 3D profile. Two height profiles throughout the overlap region give an idea where the crack travelled through the laminate. In the same way, **Figure 5-20** shows as an example the top adherend side of a typical FJ-1 configuration in layup $[(90/0)_s]_4$.

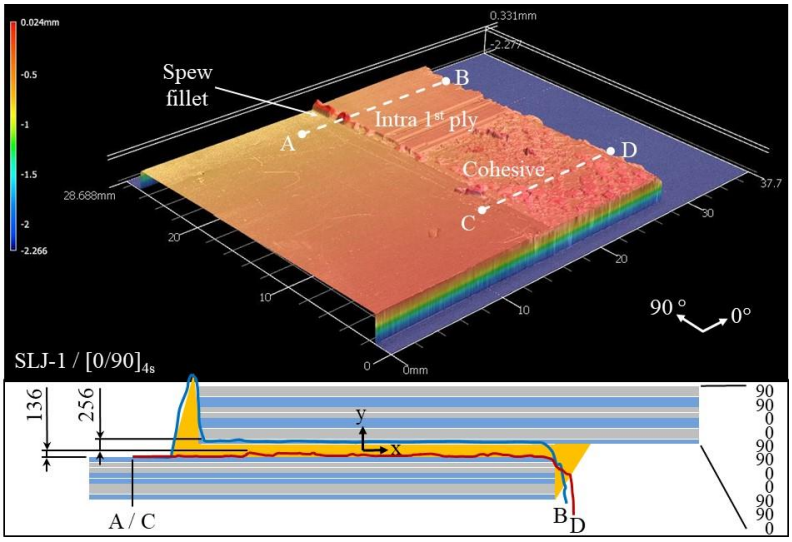

Figure 5-19: Final fracture surface of a typical SLJ-1 topology in layup $[(0/90)_s]_4$

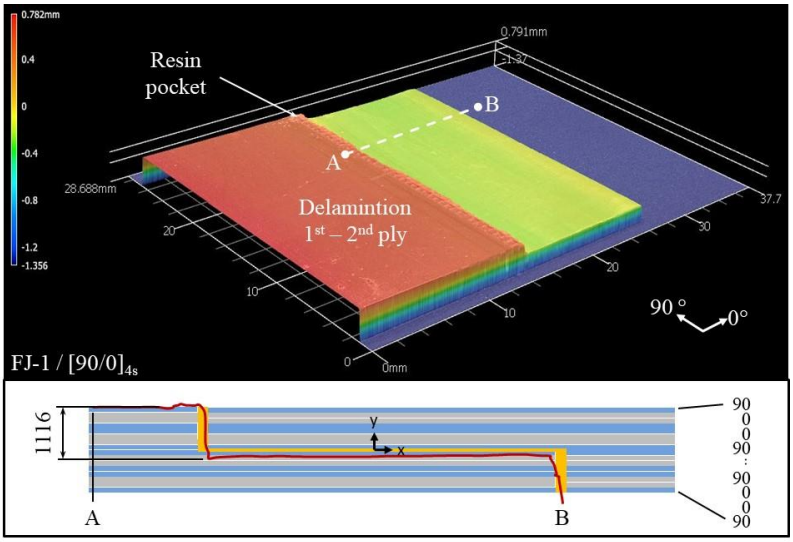

Figure 5-20: Final fracture surface of a typical FJ-1 topology in layup $[(90/0)_s]_4$

In **Figure 5-18**, the FJ-2-90/0 configuration presents a clean interply failure, together with a lower damage resistance, compared to the FJ-2-0/90, with a more complex crack path between first and second layers. At this point, there is not enough evidence to show whether the crack in

the FJ-2-0/90 developed from the inside, branching into several paths and thereby providing higher damage tolerance. It is therefore important to note that, the stress analysis in **section 5.3.3** can only link with damage initiation, not with final failure and subsequently final fracture surfaces.

5.5 DISCUSSION

5.5.1 Fracture surfaces: Competition between cohesive and composite failure

The topology which shows the largest cohesive fracture area is the SLJ-topology with $[(0/90)_s]_4$. This result is in agreement with previous observations of the authors [5-6]. An interface ply of 0° in contact with the adhesive results in high shear and low peel stresses on the bond line. This stress distribution favours fracture to occur cohesively inside the adhesive, correlating well with the stress analysis in **section 5.3.3**. For the SLJ-configuration with $[(90/0)_s]_4$ layup, with an interface ply angle of 90°, the peel stresses are high both in the adhesive and in the composite adherend. The peel strength of the adhesive is higher than the interlaminar strength of the composite [5-13]. This favours fracture to occur inside the composite, as observed in the final fracture surfaces of SLJ-configurations with $[(90/0)_s]_4$.
The failure pattern of the FJ-topologies does not follow the same trend as the SLJ-topologies. Independently from adherend stacking sequence, all final fracture surfaces reveal failure inside the composite, eventually in form of inter- and intraply matrix failure, meaning that a different failure mechanism has taken place. This different trend may be caused by the integrated topology: The FJ-topologies do not have a distinct overlap edge. It is believed, that the crack starts from the surface, at the resin pocket where the plies terminate, and then travels inside until it reaches the weakest 0/90 interface to propagate as delamination.
On the experimental side, it is difficult to identify only from the final fracture surfaces to which level adhesive is plastically deformed. On the numerical side, the load that has been chosen for the stress analysis is within 21% of average maximum load, for the weakest specimens in the study.

5.5.2 Damage initiation versus final failure

Figure 5-21 shows the maximum load and work, determined from the L-d curves. The values of work per configuration correlate well to the maximum load. The highest value for maximum load is achieved with configuration SLJ-2 of layup $[(0/90)_s]_4$ with average 20.03 ± 0.84kN. It is followed by the FJ-2 topologies, with FJ-2-90/0 (15.88 ± 1.29kN) and FJ-2-0/90 (15.24 ± 2.28kN). The lowest value is achieved by the SLJ-1 configuration with $[(90/0)_s]_4$ layup (7.10 ± 0.73kN), which is in the same range as the FJ-1 topologies, with FJ-1-90/0 (7.99 ± 0.35kN) and FJ-1-0/90 (8.45 ± 0.75kN).
Comparing SLJ-configurations, this result is expected, since a larger overlap length, in combination with a 0° outside layer, adjacent to the bond line lead to higher bending stiffness

and thus a reduction in peel stress at the bond line - see **section 5.3.3**. In case of the FJ-configurations, the values for maximum load at final failure are in accordance with the numerical stress analysis in **section 5.3.3**: the FJ-1-configurations provide a very low maximum load, while in the FJ-2-configurations the maximum load increases significantly.

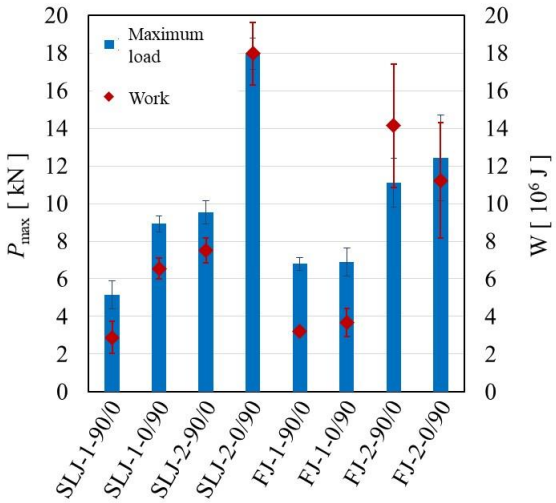

Figure 5-21: Maximum load [kN] versus strain energy [10^6 J] (± standard deviation)

In **Figure 5-22**, the load at damage initiation is compared to the maximum *Mises* stress inside the adhesive, for each configuration. **Figure 5-22** a) shows the load at damage initiation, which is experimentally derived via AE-monitoring - see **section 5.4.2**. Comparing the plots in **Figure 5-21** and **Figure 5-22** a), the trend for load at damage initiation does not correlate to the trend for maximum load: while FJ-2-90/0 shows the lowest peel and shear stress as well as highest load at damage initiation, it is outperformed by SLJ-2-0/90 in maximum load. It is believed that a cohesive failure inside the bond line of the SLJ-2-0/90 configuration would provide higher maximum load than a delamination failure inside the adherend of the FJ-2-90/0 configuration, where the crack could propagate more suddenly. Another explanation could be, that those manufacturing flaws, resin flow-out, layer undulation and ply drops, that are mainly observed inside the FJ-topologies, shown in **section 5.4.1**, could possibly influence the damage evolution inside the joint. However, these defects might as well have an influence on the damage initiation rather than on the damage propagation, or at least in the same extent.

Figure 5-22 b) shows the maximum *Mises* stress inside the adhesive, taken at a load of 1.5kN, below damage initiation. It is shown in **section 5.3.3**, that the peel stresses are not the most critical for finger joints. Therefore, *Mises* stresses give a better comparison between different topologies. Comparing **Figure 5-22** a) and b), the two FJ-configurations, FJ-1-90/0 and FJ-1-0/90, with the lowest damage initiation load are the ones with the highest maximum *Mises* stress. On the other side, the FJ-2-90/0 with the highest damage initiation load corresponds to the

lowest maximum *Mises* stress. The SLJ-configuration load at damage onset and *Mises* stresses are in between the FJ-1 and FJ-2. Among the SLJ-configurations, SLJ-2-90/0 has the hightest damage initiation load, corresponding to the lowest maximum *Mises* stress. However, as the values for different SLJ-configurations are in close range, the differences are less pronounced than in the FJs. Nevertheless, it can be concluded that the *Mises* stresses inside the adhesive is a good parameter to predict the damage onset on the joint, which indicates that the damage onset occurs inside the adhesive and not inside the composite.

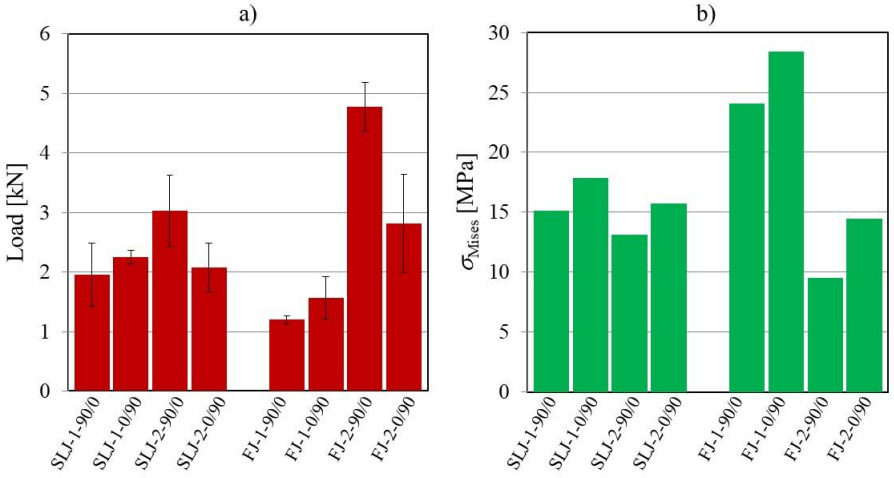

Figure 5-22: a) Load at damage initiation [kN] (± standard deviation) b) maximum *Mises* stress inside the adhesive [MPa]

It is important to note that, the adhesive thickness of the FE-model is based on a 50µm bond line thickness, whereas the experimentally measured bond line thickness was confirmed with 150µm for all specimens. This discrepancy may have an impact on the measured stress distribution in the FE-model. It is therefore expected that stresses in **Figure 5-23** b) would be lower with increased bond line thickness.

To further assess the location of damage initiation in the FJ- and SLJ-configurations, the *Mises* stress distribution is shown in **Figure 5-23** and **Figure 5-24**, respectively. Both figures show a 2D cross-section of the side of the overlap region, zoomed into the butt joint resin pocket of the FJs in **Figure 5-23** and into the triangular spew fillet of the SLJs in **Figure 5-24**, where the *Mises* stresses are found to be the highest. The stresses are taken at a load of 1.5kN, below damage initiation and do not change significantly along the width of the specimen.

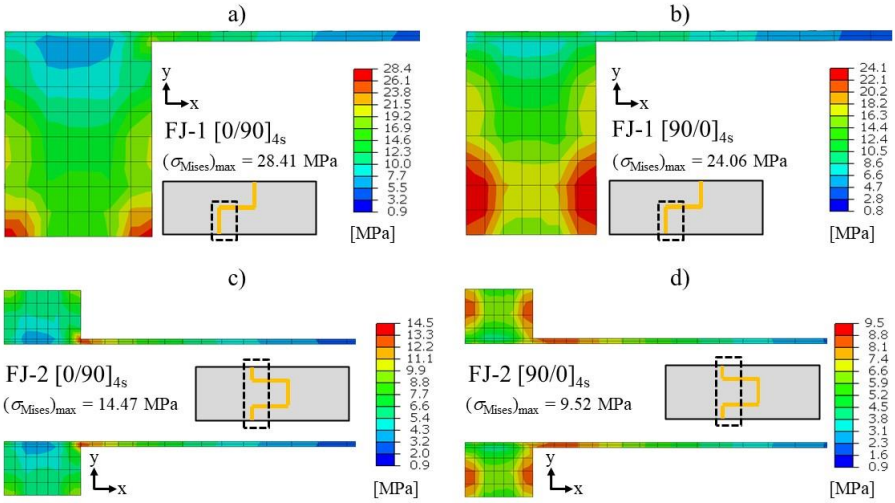

Figure 5-23: *Mises* stress distribution in all FJ-configurations at left tip of overlap area for 1.5 kN load

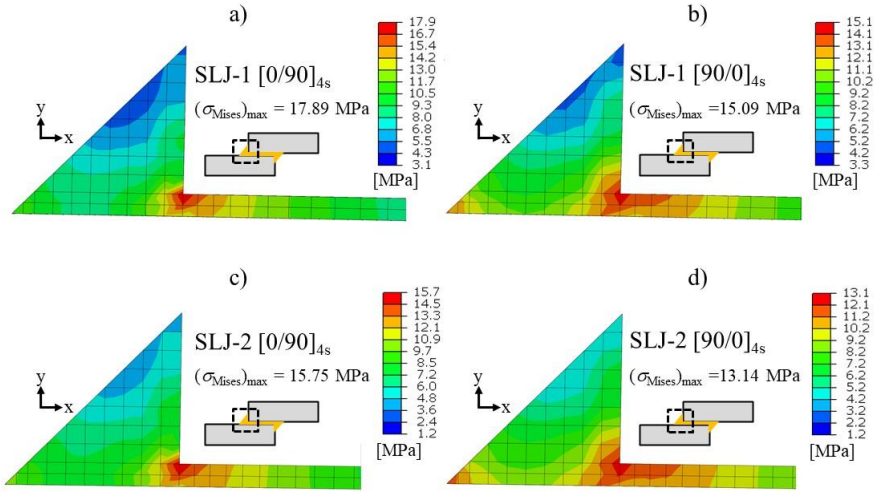

Figure 5-24: *Mises* stress distribution in all SLJ-configurations at left tip of overlap area for 1.5 kN load

The location of maximum *Mises* stress in all SLJ-configurations of **Figure 5-24** is always observed at the corner of the fillet in contact with the upper adherend corner. This suggests that a tapering of the adherend could also decrease the peak stresses [5-2]. For the FJ-configurations shown in **Figure 5-23**, the maximum *Mises* stresses occur inside the butt joined region. This maximum occurs in the alignement of the outer 0°-layer of the adherend and shows that, the *Mises* stresses in a butt joint configuration are higher in the alignement of a 0° layer than for a 90° layer. In fact, it is not the peel or shear, but the in-plane tensile stress component, which is, for the butt region in the FJ-configurations, the dominant stress component, relating to those

obeservations on **Figure 5-9** in **section 5.3.3**. This is an interesting and complementary finding to previous conclusions from the authors, stating that 0° as an interface ply in a SLJ-configuration results in the highest shear stresses in SLJ-configuration [5-6]. Based on the maximum *Mises* stress distribution, it is therefore possible, that in the experiments, the FJs failed first in the butt joint area. However, this assumption could not be confirmed by the location of damage initiation by AE-signals or from final fracture surfaces. It can be concluded that:

1) FJ-1-topologies exhibit the lowest damage onset, corresponding with highest peel stress in the overlap region, together with highest in-plane tensile stress in the butt region. The location of maximum *Mises* stress in **Figure 5-23** confirms this.
2) FJ-2-topologies, on the other hand, have the highest damage onset, corresponding with the lowest peel stresses in the overlap region and low tensile stresses in the butt region.
3) The SLJ-topologies are between FJ-1 and FJ-2 both in experimentally derived load for damage onset and in terms of peak peel stress in the numerical analysis of **section 5.3.3**. Unlike the FJ-configurations, for the SLJ-configurations, the highest *Mises* stresses are dominated by peel and shear stress components. The location of maximum *Mises* stress in **Figure 5-24** does again confirm this.

5.5.3 Damage resistance and weight efficiency

Another comparison of the different configurations can be made, by correlating the load at damage initiation (F_{init}) and the maximum load (F_{max}). The term *Damage resistance* can be proposed as

$$D = 1 - \frac{F_{init}}{F_{max}} \quad (5\text{-}3)$$

Yet another comparison of the different configurations can be made, by correlating the maximum load with the volume of the joint. Given weight equals volume times density, and given that the density of the CFRP-epoxy adhesive bonding area is approximately constant for all configurations, the volume of the joint overlap area V_{OL} can be described as the product of overlap length (*OL*) times overlap thickness (*OT*) times specimen width (*W*), and a *Joint weight efficiency* can be proposed as:

$$\Theta = \frac{F_{max}}{V_{OL}} \quad (5\text{-}4)$$

Due to the integrated geometry, the FJ-topology configurations consequently reach higher *Joint weight efficiency* than the SLJ-topologies. For applications, where the structural weight is a critical parameter, such as an aircraft fuselage, a weight efficient FJ-topology may be an alternative to the conventional SLJ-topology. In fact, the *Joint weight efficiency* of the FJ-topology could be further optimized, for example with a longer overlap length, than the 12.7mm of this study, as long as manufacturability is still feasible. **Table 5-6** describes the *Damage*

resistence and the *Joint weight efficiency* for all configurations. The values of **Table 5-6** result in a similar *Damage resistance* amongst all joint configurations, ranging from 0.70 (±0.04) for the FJ-2-90/0 up to 0.90 (±0.02) for the SLJ-1-0/90 type.

	Damage resistance	*Joint weight efficiency*
	$1-F_{init}/F_{max}$ [-]	$F_{max}/(OL*OT*W)$ [kN/mm^3]
SLJ-1-90/0	0.72 (±0.11)	5.57 (±0.69)
SLJ-1-0/90	0.80 (±0.01)	7.48 (±0.22)
SLJ-2-90/0	0.76 (±0.04)	4.39 (±0.28)
SLJ-2-0/90	0.90 (±0.02)	7.05 (±0.35)
FJ-1-90/0	0.85 (±0.00)	14.59 (±0.88)
FJ-1-0/90	0.81 (±0.04)	15.16 (±1.44)
FJ-2-90/0	0.70 (±0.04)	32.00 (±2.58)
FJ-2-0/90	0.81 (±0.06)	27.90 (±4.21)

Table 5-6: *Damage resistance* [-] and *Joint weight efficiency* [kN/mm^3] for all configurations

A final comparison can be given as guideline for designers: with both SLJ- and FJ-design expected to withstand the same design load, the FJ can effectively replace the SLJ, if weight efficiency is the main requirement. If a weight efficiency Θ, as ratio of maximum load F_{max} over joint overlap volume V_{OL}, see Eq. (5-4), is required above a value of 7.5, the FJ-design would be a better candidate than a SLJ-design. If the designer instead aims for a topology of absolute maximum joint strength, a FJ-design would not be the first choice.

5.6 CONCLUSION

This study aims to explore the effect of a multi-stacked finger joint topology in comparison with a conventional single overlap joint topology on the tensile strength of composite bonded joints. In total, 8 different topology configurations were studied under quasi-static tensile loading. A non-linear FE-analysis was performed to analyse the shear and peel stresses along the adhesive bond line. Experimental lap shear tests were performed and monitored using AE-technique to follow the damage events. The following conclusions can be drawn:

- A certain layup of the CFRP-adherend can steer the crack path. For a layup of $[(0/90)_s]_4$, the crack propagates cohesively along the bond line for SLJ- but inside the composite for FJ-topologies. With a stacking sequence of $[(90/0)_s]_4$, a crack can be triggered inside the composite for both SLJ- and FJ-topologies.

- For the FJ-1-topology the beneficial effect of avoiding eccentricity is outperformed by the detrimental effect of stiffness reduction at the overlap, such that the peak peel stresses are higher than in the SLJ-configurations. For the FJ-2-topology, the stress field changes significantly and in this case the FJ-2-topology outreaches the SLJ-topologies.
- In accordance with previous work, it was found that topologies with layup $[(0/90)_s]_4$ result in higher peak shear stress but lower peak peel stress inside the adhesive bond line when compared to layup $[(90/0)_s]_4$.
- The FJ-2-topology in layup $[(90/0)_s]_4$, which fractures inside the adherend, provides the lowest peak shear and peel stress and the highest load at damage initiation. It is however outperformed in maximum load by the SLJ-topology with layup $[(0/90)_s]_4$, which fractures cohesively inside the adhesive.
- Unlike in single overlap topologies, the most dominant stress component for damage initiation inside the FJ-design is the in-plane tensile stress, at the butt joint resin pockets, rather than peel stresses at the overlap region.
- Within this study, it was found that the von *Mises* stress inside the adhesive is a suitable parameter to correlate with the damage onset in bonded joints of different design configurations.
- Despite the common beliefe that finger joint topologies are not feasibly in terms of manufacturability, for CFRP-joints with adherend thickness below 5mm, this study proposes a simple laminating strategy for joint topologies without eccentricity but with one or two overlaps stacked through the thickness of the joint. However, manufacturing imperfection due to resin flow-out, layup undulations and ply drops inside the adherend laminates are identified in the FJ-topologies, when compared to the SLJ-topologies. Based on the discrepancy between the trends at damage initation and at maximum load, it is believed that damage evolution may be affected by those manufacturing imperfections, particularly in the case of the FJ-2-topologies.
- As design guideline, FJs can effectively replace SLJs, if weight efficiency is the main requirement. However, the SLJ design results in higher absolute maximum joint strength than the FJ-design.

REFERENCES

[5-1] J. Kupski, D. Zarouchas, S. Teixeira de Freitas, R. Benedictus: *On the influence of overlap topology on the tensile strength of composite bonded joints: Single overlap versus overlap stacking*. Int. Journal of Adhesion and Adhesives [under review]

[5-2] X. Shang, E. Marques, J. Machado, R. Carbas, D. Jiang, L. da Silva: *Review on techniques to improve the strength of adhesive joints with composite adherends*. Composites Part B, vol. 177, 2019

[5-3] I. Sen: *Design of A350 XWB Aircraft fuselage design study […].* MA thesis TU Delft, Faculty Aerospace Engineering, 2010

[5-4] E. Uhlmann, F. Sammler, S. Richarz, F. Heitmueller, M. Bilz: *Machining of Carbon Fibre Reinforced Plastics*. Procedia CIRP, vol. 24, pp. 19-24, 2014

[5-5] ASTM D5868 - 01: *Standard Test Method for Lap Shear Adhesion for Fiber Reinforced Plastic (FRP) Bonding*, 2014

[5-6] J. Kupski, S. Teixeira de Freitas, D. Zarouchas, R. Benedictus: *Layup variation Composite layup effect on the failure mechanism of single lap bonded joints.* Composite Structures, vol. 217, pp. 14-26, 2019

[5-7] K. Kaw: *Mechanics of Composite Materials*. Boca Raton: Taylor & Francis, 2006

[5-8] S. Teixeira de Freitas, D. Zarouchas, J.A. Poulis: *The use of acoustic emission and composite peel tests to detect weak adhesion in composite structures.* Journal of Adhesion, vol. 94, pp. 743-766, 2018

[5-9] Material datasheet: *A75-T-2-0123-1-1*. Airbus Material-Handbook Structure, 2014

[5-10] P. Camanho, A. Arteiro, A. Melro, G. Catalanotti, M. Vogler: *Three-dimensional invariant-based failure criteria for fibre-reinforced composites*. Int. Journal of Solids & Structures, vol. 55, pp. 92-107, 2015

[5-11] Material datasheet*: Scotch-Weld™ Structural Adhesive Film AF 163-2AF163-2k*. 3M, Multimedia database, 2009

[5-12] R. Adams: *Strength Predictions for Lap Joints, Especially with Composite Adherends. A Review*. J. Adhesion vol. 30, pp. 219-242, 1989

[5-13] S. Teixeira de Freitas, J. Sinke: *Failure analysis of adhesively-bonded skin-to-stiffener joints: Metal–metal vs. composite–metal*. Eng. Failure Analysis, vol. 56, pp. 2-13, 2015

[5-14] J. Kupski, D. Zarouchas, S. Teixeira de Freitas: *Thin-plies in adhesively bonded carbon fiber reinforced polymers.* Composites Part B, vol. 184, 2020

[5-15] R.D. Adams, J. Comyn, W.C. Wake: *Structural Adhesive Joints in Engineering*. Springer Science & Business Media, 1997

[5-16] *Ultraviolet-Ozone Surface treatment*. Three Bond Technical News, 1987

[5-17] J. Poulis: *Small cylindrical adhesive bonds*. PhD thesis, Technical University Delft, The Netherlands, ISBN-90370-0082-7, pp. 39-62, 1993

[5-18] S. Teixeira de Freitas, J. Sinke: *Adhesion Properties of Bonded Composite-to-Aluminium Joints Using Peel Tests*. Journal of Adhesion, vol. 90, pp. 511-525, 2014

[5-19] J. Ahamed, M. Joosten, P. Callus, S. John, C.H. Wang: *Ply-interleaving technique for joining hybrid carbon/glass fibre composite materials*. Composites Part A, vol. 84, pp. 134-146, 2016

6 CONCLUSIONS AND RECOMMENDATIONS

6.1 INTRODUCTION

The previous **Chapter 3** to **Chapter 5** investigated different laminate specific design parameters, which all contribute to an increase of strength in composite bonded joints. Bringing all of the findings together, this chapter aims to highlight the final conclusions of the PhD-thesis. In **section 6.2** the results and findings of each chapter are briefly summarized and put into context to each other to draw the *Lessons learned*. **Section 6.3** is a reflection on the moments along this Ph.D.-journey, where problems arose or limitations were reached, for example due to manufacturing tolerances or uncertainties within the test design. Based on the "Lessons learned" and the currently observed limitations, **section 6.3** suggests recommendations for further approaches, such as extending the non-linear FE-model with a Progressive Damage Analysis (PDA) or including interrupted X-ray scanning methods to experimentally verify early damage onset. Finally, in **section 6.4**, the reader will be taken away to further improve the tensile strength of CFRP-bonded joints with more disruptive ideas, to eventually reach their maximum potential.

6.2 LESSONS LEARNED

The work developed during this thesis shows that, the failure mode is highly influenced by the orientation of the interface lamina in contact with the adhesive, such that, a 0° interface ply causes failure within the bond line, while a 90° interface ply causes failure inside the composite adherend. The results of **Chapter 3** show that increasing the adherend bending stiffness postpones damage initiation but not final failure. Instead, the ultimate load is influenced by how the damage progresses inside the joint. Therefore, the adherend layup should be optimized for bending stiffness until first-ply failure. Beyond damage initiation, the stacking sequence influences tensile strength up to final failure, if it provides a complex crack paths inside the composite adherend and it can be concluded that a quasi-isotropic layup may not be the best choice in terms of tensile joint strength. Decreasing the ply thickness of laminated adherends, in **Chapter 4**, increases the maximum load and delays damage initiation of the joint, however the damage progression till final failure is more sudden. Finally, when comparing SLJ- with FJ-topologies in **Chapter 5**, different trends at damage initiation and at maximum load are believed to result from how the damage propagates inside the joint. A topology with 2 fingers and layup $[(90/0)_s]_4$, which fails entirely inside the adherend, provides the lowest peak shear and peel stress and the highest load at damage initiation. It is however outperformed in maximum load by a single lap joint topology with layup $[(0/90)_s]_4$, with mostly cohesive failure. Unlike in SLJs, the most dominant stress component for damage in FJs, is the in-plane tensile stress, at the butt joint region, rather than the peak peel or shear stress level at the overlap region.

When comparing the three methods in **Chapter 3** to **Chapter 5**, the question can be raised, how much the load at damage initiation or at final failure increases due to a change in each of the

parameters. From experimental AE-results, a change in layup increases the load at damage initiation by 35% from 2.5kN in case of $[45/90/-45/0]_{2s}$ to 3.4 kN in case of $[0/45/90/-45]_{2s}$. A 35% increase in damage resistance is achieved when comparing the two different layups $[0/45/90/-45]_{2s}$ and $[45/0/-45/0]_{2s}$ with similar bending stiffness. In comparison, a reduction of ply thickness provides up to 49% increase of load at damage initiation, from 11.0 kN in case of 200µm to 16.4kN in case of 50µm ply thickness. And finally, a FJ-topology with 2 fingers and layup $[(90/0)_s]_4$ indicates 58% higher load at damage initiation (4.78kN), compared to a SLJ-topology with the same bonding area and layup (3.03kN). The change in topology, as a global parameter, is apparently more effective than a change of laminate specific parameters, stacking sequence and ply thickness. This result would be in agreement with the work of Shang et al. [6-1], who compared different techniques to enhance joint efficiency by considering the increase on average lap shear strength and the manufacturing difficulty associated with each technique.
However, the numbers are in a close range and it is important to keep in mind that, in **Chapter 3**, the more brittle *EA9695* adhesive is used with a low bond line thickness of 50µm, and the test layout in **Chapter 4** is based on the *NTPT-HTS(12K)-5-35%* adherend prepreg with decreased longitudinal stiffness. As seen in numerous literature of **section 2.2**, adherend stiffness and bond line thickness are amongst the parameters that have the biggest influence on the overall joint strength in lap shear. A fair comparison would therefore require a study on the effect of different laminate parameters, with at least a fixed material set, if available.
In addition, the comparison of different techniques to improve joint strength imposes the idea of a combined approach: for instance, a 2-finger joint from interlayer-toughened prepreg material, with optimized fiber orientation and ply thickness in the bond line region, providing multiple techniques to enhance joint strength either towards damage initiation, or damage resistance, or maybe to both. As Boss et al. [6-2] stated, a combination of increasing bending stiffness through higher in-plane longitudinal modulus and geometrical grading by use of taper, for example, would provide an overall better joint strength. The idea of combining different design features in one joint stands however in contradiction to the need for simple and robust solutions that industry entails. Furthermore, it would be interesting to study whether different out-of-plane reinforcement techniques would impair each other. Certainly, all three design parameters, studied in **Chapter 3** to **Chapter 5**, influence the load at damage initiation but only the fiber angle seems to have a beneficial effect on the damage resistance of the joint.
The suggested term “damage resistance” is arguably simplified. It does not take into account, whether the damage is inside the adhesive or adherend. It is therefore only added in **Chapter 4** and **Chapter 5** as a last comment in the discussion, while the main part of the study is focussed on the stress analysis and the experimental tests. Lumping it into one value is supposed to visualize to the reader the gap between load at damage initiation and maximum load, see comment below. This was not done in the first study, in **Chapter 3**, where this gap is instead presented through **Figure 3-16**.

6.3 CURRENT LIMITATIONS

6.3.1 Spew fillet corner

As in all experimental tests, the specimens suffer from limited accuracy and manufacturing flaws. All SLJ-specimens had a spew fillet shape similar to a 45° triangle. In fact, the shape was in some cases convex, and in other cases rather concave. In all cases, the spew fillet reached at least up to half of the height of the adherend. Based on this, the fillet was modelled as triangular fillet shape of 45° slope reaching up half the height of the adherend as it is believed to be a good approximation for all specimens within this work. On the numerical side, the chosen 3D-model of a SLJ-topology suffered a similar limitation, as it accounts for stress singularities at the sharp corners of the fillet. In order to avoid these numerical artefacts, these sharp corners were so far excluded from the stress analysis and the plots along the bond line length, from which peel and shear stresses were taken, exclude the last few micrometres of the outermost element.

6.3.2 Ply block interfaces

Regarding the work on ply thickness, in **Chapter 4**, it is important to notice that, for the THICK and MEDIUM, the crack propagates preferably at the interface between two 45° plies, which can be considered as inter-laminar failure. This is no longer the case for the THIN (no ply blocks), where the crack path is along the 0/45-interface. The interface within a ply block is much less pronounced than the interface between plies of different orientation, due to nesting effects. Nevertheless, the crack path for THICK and MEDIUM seems to be affected by the interface of the ply blocks. Therefore, the fracture patterns could potentially be different if the different ply thicknesses were achieved by producing plain plies of different thicknesses instead of a ply block.

6.3.3 Manufacturing imperfections

Manufacturing imperfections due to resin flow-out, layup undulations and ply drops inside the adherend laminates were identified in **Chapter 5**, in the FJ-topologies, when compared to the SLJ-topologies. Based on the discrepancy between the trends at damage initiation and at maximum load, it is believed that damage evolution may be affected by those manufacturing imperfections, particularly in the case of the FJ-2-topologies.

6.3.4 Material input values

Two prepreg materials were used throughout the PhD-research: *Hexply® F6376C-HTS (12K)-5-35%* in 125g/m^2 and *NTPT Thinpreg™ 135* with *HS40/T800* carbon fibers in 67g/m^2. For the first material, used in **Chapter 3** and **Chapter 5** the transverse tensile strength, Y_T = 102MPa, is arguably high. It is based on the provided datasheet [6-3]. But since the adherend laminates

were fabricated with the original production prepreg inside the Airbus facility, it appeared as a valid and comprehensive source of information. To confirm this high value of transverse tensile strength, additional tensile tests in accordance with ASTM-D3039-14 were conducted. The presumably high proposed Y_T value, given by TDS, could thereby be experimentally validated. The detailed test results are presented in **APPENDIX G**. For the second material in **Chapter 4**, the input values were combined from different sources, as the provided material datasheet from *NorthTPT* [6-4] was incomplete. Tests were performed to receive X_T, Y_T, E_{11}^T, E_{22}^T, E_{33}^T, while G_{12}, G_{13} and S_{12}=S_{13} were taken from the provided datasheet. S_{23} and Y_C were taken from the first material *Hexply® F6376C-HTS (12K)-5-35%*. Poisson's ratios were in all chapters taken from the well-studied *Hexply® 8552-IM7* [6-5]. Although the origin of input values in **Chapter 4** may not be ideal, it is believed that there is no significant overshoot with the chosen values.

6.3.5 Damage progression

The proposed models in this work are limited to damage initiation and intra ply failure. They comprise linear-elastic material behaviour for the composite part, as well as linear-elastic / plastic behaviour for the adhesive and include the effect of non-linear geometry. Beyond that, there is no tool used to model a crack start or growth, damage progression or a delamination. Therefore, future work should aim for extending the model to further predict the damage resistance of one joint design over another.

On the experimental side, this work proposes the use of Acoustic Emission techniques to follow the damage events from initiation till final failure. The additional DIC-system in **Chapter 3** and **Chapter 4** did not capture any crack propagation visually. A next step could be the use of high-speed-cameras. Pre-trials indicated a minimum frame rate of 40,000 pictures per second to capture any crack propagation, even at displacement-controlled loading speed of 1.3mm/min. Depending on the available camera system, this would result in low-resolution pictures, which capture only the events visible on the outside surface. Another strategy is to take a look inside the material with micro-CT scanning methods, allowing to detect damage through the entire thickness of the material. Here the challenge lies in the complexity of the test setup, either restricting the specimen size to as much as a few millimetres in order to fit into a miniature tensile machine that can be integrated into existing micro-CT scanning systems. Or the quasi-static test would involve interruptions at a certain load, where the specimen is removed from the fixture to receive ex-situ CT-scanning.

6.4 UNVEILING THE FULL POTENTIAL OF LAMINATED ADHERENDS

Tailoring fiber direction, decreasing ply thickness or interleaving plies, as proposed in this work, are effective ways to improve the out-of-plane strength of a CFRP-laminate. A step further is the idea of hierarchical structured laminates. In the three presented studies in this thesis, the ply architecture is so far only tailored in-plane. But recent developments in fibre placement technology also allow the fibres to be aligned out-of-plane. Hereafter, a few of those are mentioned which are believed to be the most promising further approaches to improve joint

strength. Pascoe et al. [6-6] inserted interlocked thin ply reinforcement units between laminae and found that mode-I fracture toughness was increased by 78%, while mode II fracture toughness was not affected. An 11% reduction in delamination area was achieved, resulting in a 5% increase in CAI-strength. Minakuchi [6-7, 6-8] introduced continuous fibers in the adhesive layer, providing a fiber bridging effect and suppressing the crack propagation. Nonwoven PPS-veils were interleaved within CFRP-laminates by Ramirez et al. [6-9]. Results show that in modes I and II the interlaminar fracture toughness (IFT) increases with the areal density of the veil up to a plateau and at a given areal density. The mode-I IFT is greater for thin fibres than for thicker fibres. Haese et al. [6-10, 6-11] mimicked the crossed-lamellar microstructure of a sea-shell, to reproduce the biological toughening mechanisms, tunnel cracking, crack deflection and debonding, within a CFRP-laminate. Results demonstrate that this bio-inspired hierarchical structure can be loaded up to record large curvatures (in comparison with other CFRPs and hybrid CFRPs) while retaining its structural integrity and dissipating energy under stable conditions [6-10].

Other interesting design concepts for bonded joints are hierarchical structures inside the bonding interface. Budzik et al. [6-12, 6-13] created distinct bond line discontinuities, which have an effect on interfacial crack growth. Narducci et al. [6-14] developed a film-casting technique to deposit 13μm thin layers of polylactic acid (PLA) on the interface between carbon/epoxy prepreg plies to increase the interlaminar toughness. One of the latest trends in 3D composite design is the use of aligned carbon nanotubes, graphene layers or non-woven nano-veils in the interface between laminated plies. Kalfon-Cohen et al. [6-15, 6-16] realized a hierarchical architecture termed ‘nanostitching’ by aligning carbon nanotubes and using them as interlaminar reinforcement of thin ply unidirectional CFRP-prepregs. They found an increase in interlaminar fracture toughness and in-plane strengths. FE-predictions of damage progression highlighted the complementary nature of positive thin ply and nanostitching effects that are consistent with a 15% improvement in modes I and II interlaminar fracture toughness due to the aligned carbon nanotubes at the thin ply interfaces. More work was conducted on the development of nanofibrous interlayer toughening to increase mode-I fracture toughness, and therefore delamination resistance [6-17 – 6-27].

The extensive amount of recent work on micro- and nano-scaled hierarchical structures on laminated plies and on the bond line interface adumbrates the untouched potential that still lies in CFRP bonded joints. In any case, there are new joint designs yet to explore and the future holds stunning possibilities to pave the way for structural adhesive bonding.

REFERENCES

[6-1] X. Shang, E. Marques, J. Machado, R. Carbas, D. Jiang, L. da Silva: *Review on techniques to improve the strength of adhesive joints with composite adherends*. Composites Part B, vol. 177, 2019

[6-2] J. Boss, V. Ganesh, C. Lim: *Modulus grading versus geometrical grading of composite adherends in single-lap bonded joints.* Composite Structures, vol. 62, pp. 113-121, 2003

[6-3] Material datasheet: *A75-T-2-0123-1-1*. Airbus Material-Handbook Structure, 2014

[6-4] Material datasheet: *Thinpreg^{TM} 135*. NTPT, 2017

[6-5] P. Camanho, A. Arteiro, A. Melro, G. Catalanotti, M. Vogler: *Three-dimensional invariant-based failure criteria for fibre-reinforced composites*. Int. Journal of Solids & Structures, vol. 55, pp. 92-107, 2015

[6-6] J.-A. Pascoe, S. Pimenta, S. Pinho: *Interlocking thin-ply reinforcement concept for improved fracture toughness and damage tolerance.* Composites Science and Technology, vol. 181, pp. xx, 2019

[6-7] S. Minakuchi: *Fiber-Reinforcment-Based Crack Arrester For Composite Bonded Joints.* Proceedings of the 20th ICCM 2015, Copenhagen, 2015

[6-8] S. Minakucchi, N. Takeda: *Arresting Fatigue Crack in Composite Bonded Joints using Fiber-Reinforced Design Feature.* Proceedings of the 29th ICAF Symposium, Nagoya, 2017

[6-9] V. Ramirez, P. Hogg, W. Sampson: *The influence of the nonwoven veil architectures on interlaminar fracture toughness of interleaved composites.* Composites Science and Technology, vol. 110, pp. 103-110, 2015

[6-10] R. Haesae, S. Pinho: *A novel aluminium/CFRP hybrid composite with a bio-inspired cross-lamellar microstructure for preservation of structural integrity.* Composites Science and Technology, vol. 182, pp. xx, 2019

[6-11] R. Haesae, S. Pinho: *Failure mechanisms of biological crossed-lamellar microstructures applied to synthetic high-performance fibre-reinforced composites.* Journal of Mechanics and Physics of Solids, vol. 125, pp. 53-73, 2019

[6-12] M. Budzik, J. Jumel, M. Shanahan: *Impact of Interface Heterogeneity on Joint Fracture.* Journal of Adhesion, vol. 88, pp. 885-902, 2012

[6-13] S. Heide-Jørgensen, M. Budzik: *Effects of bondline discontinuity during growth of interface cracks including stability and kinetic considerations.* Journal of Mechanics and Physics of Solids, vol. 117, pp. 1-21, 2018

[6-14] F. Narducci, K. Lee, S. Pinho: *Interface micro-texturing for interlaminar toughness tailoring: a film-casting technique.* Composites Science and Technology, vol. 156, pp. 203–214, 2018.

[6-15] E. Kalfon-Cohen, R. Kopp, C. Furtado, X. Ni, A. Arteiro, G. Borstnar, M. Mavrogordato, I. Sinclair, S. Spearing, P. Camanho, B. Wardle: *Synergetic effects of thin plies and aligned carbon nanotubeinterlaminar reinforcement in composite laminates.* Composites Science and Technology, vol. 166, pp. 160-168, 2018

[6-16] X. Ni, C. Furtado, E. Kalfon-Cohen, Y. Zouh, G. Valdes, T. Hank, P. Camanho, B.

Wardle: *Static and fatigue interlaminar shear reinforcement in aligned carbon nanotube-reinforced hierarchical advanced composites.* Composites Part A: Applied Science and Manufacturing, vol. 120, pp. 106-120, 2019

[6-17] C. Chazot, A. John Hart: *Understanding and control of interactions between carbon nanotubes and polymers for manufacturing of high-performance composite materials.* Composites Science and Technology, vol. 183, 2019

[6-18] S. Garcia-Rodriguez, J. Costa, K. Rankin, R. Boardman, V. Singery, J. Mayugo: *Interleaving light veils to minimise the trade-off between mode-I interlaminar fracture toughness and in-plane properties.* Composites: Part A, vol. 128, 2020

[6-19] C. Pramanik, D. Nepal, M. Nathanson, J. Gissinger, A. Garley, R. Berry, A. Davijani, S. Kumar, H. Heinz: *Molecular engineering of interphases in polymer/carbon nanotube composites to reach the limits of mechanical performance.* Composites Science and Technology, vol. 166, pp. 86-94, 2018

[6-20] S. van der Heijden, L. Daelemans, T. Meireman, I. de Baere, H. Rahier, W. van Paepegem, K. de Clerck: *Interlaminar thoughening of resin transfer molded laminates by electrospun polycaprolactone structures: Effect of the interleave morphology.* Composites Science and Technolgoy, vol. 136, pp. 10-17, 2016

[6-21] E. Ozden-Yenigun, K. Bilge, E. Sunbuloglu, E. Bozdag, M. Papila: High strain rate response of nanofiber interlayered structural composites

[6-22] T. Brugo, R. Palazzetti: The effect of thickness of Nylon 6,6 nanofibrous mat on Modes I-II fracture mechanisms of UD and woven composites laminates. Composite Structures, vol. 154, pp. 172-178, 2016

[6-23] L. Daelemans, S. van der Heijden, I. de Baere, H. Rahier, W. van Paepegem, K. de Clerck: *Improved fatigue delamination behaviour of composite laminates with electrospun thermoplastic nanofibrous interleaves using the Central Cut-ply method.* Composites Part A, vol. 94, pp. 10-20, 2017

[6-24] T. Brugo, G. Minak, A. Zucchelli, H. Saghafi, M. Fotouhi: *An Investigation on the Fatigue based Delamination of Woven Carbon-epoxy Composite Laminates Reinforced with Polyamide Nanofibers.* Procedia Engineering, vol. 109, pp. 65-72, 2015

[6-25] T. Brugo, G. Minak, A. Zucchelli, X. Yan, J. Belcari, H. Saghafi, R. Palazzetti: *Study on Mode I fatigue behaviour of Nylon 6,6 nanoreinforced CFRP laminates.* Composite Structures, vol. 164, pp. 51-57, 2017

[6-26] L. Daelemans, S. van der Heijden, I. de Baere, H. Rahier, W. van Paepegem, K. de Clerck: *Nanofibre bridging as a toughening mechanism in carbon/epoxy composite laminates interleaved with electrospun polyamide nanofibrous veils.* Composites Science and Technology, vol. 117, pp. 244-256, 2015

[6-27] K. Bilge, Y. Yorulmaz, F. Javanshour, A. Uerkmez, B. Yilmaz, E. Simsek, M. Papila: *Synergistic role of in-situ crosslinkable electrospun nanofiber/epoxy nanocomposites interlayers for superior laminated composites.* Composites Science and Technology, vol. 151, pp. 310-316, 2017

APPENDIX

The following appendix contains the general expressions which were used to obtain failure analysis in **section 3.6.3** and **section 4.5.2**, as well as experimental test data for material characterization in addition to the provided TDS in **Chapter 3** till **Chapter 5**. For failure inside the adhesive, the *Mises* and *Drucker-Prager* criterion were selected. For failure inside the composite, criteria of *Hashin*, *Puck* and the *3D-invariant based* were chosen. The following convention is applied to all equations:

$\sigma_{xx}, \sigma_{yy}, \sigma_{zz}$	Normal components of the 3D stress tensor
$\tau_{xy}, \tau_{xz}, \tau_{yz}$	Shear components of the 3D stress tensor stresses
$\sigma_1, \sigma_2, \sigma_3$	Principal stresses
σ_{yt}	Adhesive tensile yield stress
x_t, x_c, y_t, y_c	Tensile/compressive strength of UD-ply, longitudinal and transverse
s_{xy}, s_{xz}, s_{yz}	Shear strength of UD-ply

APPENDIX A

For a general state of stress, the equivalent tensile or *Mises* stress, σ_V is used to predict yielding of materials under multiaxial loading conditions using results from simple uniaxial tensile tests, given:

$$f_{\text{Mises}} = \frac{\sigma_{yt}}{\sigma_V} \quad \text{(A-1)}$$

$$\sigma_V = \sqrt{\frac{1}{2}\left[\left(\sigma_{xx} - \sigma_{yy}\right)^2 + \left(\sigma_{yy} - \sigma_{zz}\right)^2 + (\sigma_{zz} - \sigma_{xx})^2 + 6\left(\tau_{xy}{}^2 + \tau_{yz}{}^2 + \tau_{zx}{}^2\right)\right]} \quad \text{(A-2)}$$

APPENDIX B

The quadratic *Drucker-Prager* yield criterion was used, following the approach of da Silva et al. [3-26 - 3-27], where the yield criterion can be expressed as

$$f_{\text{Drucker}} = aq^b - p - p_t \quad \text{(B-1)}$$

The terms that appear in (B-1) are defined as

$$a = \frac{1}{3(\beta-1)\sigma_{yt}} \quad \text{(B-2)}$$

$$q = \sqrt{\frac{1}{2}\left[(\sigma_1 - \sigma_2)^2 + (\sigma_2 - \sigma_3)^2 + (\sigma_3 - \sigma_1)^2\right]} \quad \text{(B-3)}$$

$$p = \frac{1}{3}(\sigma_1 + \sigma_2 + \sigma_3) \quad \text{(B-4)}$$

$$p_t = \frac{\beta \sigma_{yt}}{3(\beta - 1)} \quad \text{(B-5)}$$

with

b = 2 : Exponent parameter

β = 1.45 : Compressive yield stress over tensile yield stress

APPENDIX C

The *Hashin* failure criteria [3-21, 3-22]

Fiber failure in tension, if $\sigma_{xx} > 0$:

$$f_{ft} = \left(\frac{\sigma_{xx}}{x_t}\right)^2 + \frac{\tau_{xy}^2 + \tau_{xz}^2}{s_{xy}^2} \quad \text{(C-1)}$$

Fiber failure in compression, $\sigma_{xx} < 0$:

$$f_{fc} = \frac{\sigma_{xx}}{x_c} \quad \text{(C-2)}$$

Matrix failure in tension, if $\sigma_{yy} + \sigma_{zz} > 0$:

$$f_{mt} = \left(\frac{\sigma_{yy} + \sigma_{zz}}{y_t}\right)^2 + \frac{\tau_{yz}^2 - \sigma_{yy}\sigma_{zz}}{s_{yz}^2} + \frac{\tau_{xy}^2 + \tau_{xz}^2}{s_{xy}^2} \quad \text{(C-3)}$$

Matrix failure in compression, if $\sigma_{yy} + \sigma_{zz} < 0$:

$$f_{mc} = \frac{1}{|y_c|}\left(\left(\frac{y_c}{2\, s_{yz}}\right)^2 - 1\right)(\sigma_{yy} + \sigma_{zz}) + \frac{(\sigma_{yy} + \sigma_{zz})^2}{4 s_{yz}^2} + \frac{\tau_{yz}^2 - \sigma_{yy}\sigma_{zz}}{s_{yz}^2} + \frac{\tau_{xy}^2 + \tau_{xz}^2}{s_{xy}^2} \quad \text{(C-4)}$$

APPENDIX D

Failure analysis of FRP-laminates by means of physically based phenomenological models, by Puck and Schuermann [3-23 – 3-25].

Fiber failure in tension, if $\sigma_{xx} > 0$:

$$f_{ft} = \frac{\sigma_{xx}}{X_t} \quad \text{(D-1)}$$

Fiber failure in compression, $\sigma_{xx} < 0$:

$$f_{\mathrm{fc}} = \frac{\sigma_{11}}{X_{\mathrm{c}}} \quad \text{(D-2)}$$

Puck criterion for interfiber fracture caused by a 3D stress state:

In order to get physically reasonable results, it is necessary to respect some restrictions for the choice of the so-called inclination parameters [3-24]:

$$p_{\perp\parallel}^{(+)} = 0.275 \; ; \; p_{\perp\parallel}^{(-)} = 0.275 \; ; \; p_{\perp\perp}^{(+)} = 0.350 \; ; \; p_{\perp\perp}^{(-)} = 0.300$$

The 3D stress analysis provides the stress condition of a UD-layer related to its natural axes x;y;z The stresses $\sigma_{\mathrm{n}}(\theta)$, $\tau_{\mathrm{nt}}(\theta)$, $\tau_{\mathrm{nl}}(\theta)$ of an arbitrary sectional plane with an inclination angle θ, which can be inserted into the interfiber failure criteria, are calculated from

$$\sigma_{\mathrm{n}}(\theta) = \sigma_{\mathrm{yy}} \cos^2\theta + \sigma_{\mathrm{zz}} \sin^2\theta + 2\tau_{\mathrm{yz}} \sin\vartheta \cos\vartheta \quad \text{(D-3)}$$

$$\tau_{\mathrm{nt}}(\theta) = (\sigma_{\mathrm{zz}} - \sigma_{\mathrm{yy}}) \sin\vartheta \cos\vartheta + \tau_{\mathrm{yz}}(\cos^2\theta - \sin^2\theta) \quad \text{(D-4)}$$

$$\tau_{\mathrm{nl}}(\theta) = \tau_{\mathrm{zx}} \sin\vartheta + \tau_{\mathrm{yx}} \cos\vartheta \quad \text{(D-5)}$$

Matrix failure in tension, if $\sigma_{\mathrm{n}}(\theta) \geq 0$:

$$f_{\mathrm{mt}} = \sqrt{\left[\left(\frac{1}{R_{\perp}^{(+)\mathrm{A}}} - \frac{p_{\perp\psi}^{(+)}}{R_{\perp\psi}^{\mathrm{A}}}\right)\sigma_{\mathrm{n}}(\theta)\right]^2 + \left(\frac{\tau_{\mathrm{nt}}(\theta)}{R_{\perp\perp}^{\mathrm{A}}}\right)^2 + \left(\frac{\tau_{\mathrm{nl}}(\theta)}{R_{\perp\parallel}^{\mathrm{A}}}\right)^2} + \frac{p_{\perp\psi}^{(+)}}{R_{\perp\psi}^{\mathrm{A}}}\sigma_{\mathrm{n}}(\theta) \quad \text{(D-12)}$$

Matrix failure in compression, if $\sigma_{\mathrm{n}}(\vartheta) < 0$:

$$f_{\mathrm{mc}} = \sqrt{\left[\frac{p_{\perp\psi}^{(-)}}{R_{\perp\psi}^{\mathrm{A}}}\sigma_{\mathrm{n}}(\theta)\right]^2 + \left(\frac{\tau_{\mathrm{nt}}(\theta)}{R_{\perp\perp}^{\mathrm{A}}}\right)^2 + \left(\frac{\tau_{\mathrm{nl}}(\theta)}{R_{\perp\parallel}^{\mathrm{A}}}\right)^2} + \frac{p_{\perp\psi}^{(-)}}{R_{\perp\psi}^{\mathrm{A}}}\sigma_{\mathrm{n}}(\theta) \quad \text{(D-13)}$$

with

$$R_{\perp\perp}^{\mathrm{A}} = \frac{Y_{\mathrm{c}}}{2\left(1 + p_{\perp\perp}^{(-)}\right)} \quad \text{(D-6)}$$

$$R_{\perp}^{(+)\mathrm{A}} = Y_{\mathrm{T}} \; ; \; R_{\perp\parallel}^{\mathrm{A}} = S_{12} \; ; \; R_{\perp\perp}^{\mathrm{A}} = \frac{Y_{\mathrm{c}}}{2\left(1 + p_{\perp\perp}^{(-)}\right)} \quad \text{(D-7)}$$

$$\frac{p_{\perp\psi}^{(+)}}{R_{\perp\psi}^{\mathrm{A}}} = \frac{p_{\perp\perp}^{(+)}}{R_{\perp\perp}^{\mathrm{A}}}\cos^2\psi + \frac{p_{\perp\parallel}^{(+)}}{R_{\perp\parallel}^{\mathrm{A}}}\sin^2\psi \quad \text{(D-8)}$$

$$\frac{p_{\perp\psi}^{(-)}}{R_{\perp\psi}^{\mathrm{A}}} = \frac{p_{\perp\perp}^{(-)}}{R_{\perp\perp}^{\mathrm{A}}}\cos^2\psi + \frac{p_{\perp\parallel}^{(-)}}{R_{\perp\parallel}^{\mathrm{A}}}\sin^2\psi \quad \text{(D-9)}$$

$$\cos^2\psi = \frac{\tau_{\mathrm{nt}}{}^2}{\tau_{\mathrm{nt}}{}^2 + \tau_{\mathrm{nl}}{}^2} \quad \text{(D-10)}$$

$$\sin^2\psi = \frac{{\tau_{\mathrm{nl}}}^2}{{\tau_{\mathrm{nt}}}^2+{\tau_{\mathrm{nl}}}^2} \quad \text{(D-11)}$$

For a closed-from analytical solution, the assumption has to be made that:

$$\frac{p_{\perp\psi}^{(-)}}{R_{\perp\psi}} = \frac{p_{\perp\perp}^{(-)}}{R_{\perp\perp}^{\mathrm{A}}} = \frac{p_{\perp\parallel}^{(-)}}{R_{\perp\parallel}} = \text{const.}$$

APPENDIX E

Camanho's *3D-invariant based* failure criterion for composite UD-laminae [3-7]

In-situ expressions after Camanho et al. [3-28]

The general expression for the in-situ strengths are presented in this section. Note that

$$K_1 = \frac{K_{\mathrm{p}} G_{12}}{1+K_{\mathrm{p}}} \quad \text{(E-1)}$$

$$K_2 = S_{\mathrm{LP}}\left(1 - \frac{K_{\mathrm{p}}}{1+K_{\mathrm{p}}}\right) \quad \text{(E-2)}$$

For an inner ply:
the in-situ transverse tensile strength is the maximum between the transverse tensile strength of a thin embedded ply and a thick embedded ply, i.e.,

$$Y_{\mathrm{T}}^{\mathrm{is}} = \max\left(\sqrt{\frac{8G_{Ic}}{\mu t A_{22}^{o}}}, 1.12\sqrt{2}Y_{\mathrm{T}}^{\mathrm{UD}}\right) \quad \text{(E-3)}$$

The in-situ in-plane shear strength is the maximum between the in-plane shear strength of a thin embedded ply and a thick embedded ply, i.e., the maximum of

$$S_{\mathrm{L}}^{\mathrm{is}} = K_1\gamma_{12}^{\mathrm{is}} + K_2 \quad \text{(E-4)}$$

The in-situ transverse compressive strength $Y_{\mathrm{C}}^{\mathrm{is}}$ is given by

$$Y_{\mathrm{C}}^{\mathrm{is}} = \frac{S_{\mathrm{L}}^{\mathrm{is}} Y_{\mathrm{C}}^{\mathrm{UD}}}{S_{\mathrm{L}}^{\mathrm{UD}}} \quad \text{(E-5)}$$

For an outer ply:
The in-situ transverse tensile strength is the maximum between

$$Y_{\mathrm{T}}^{\mathrm{is}} = \max\left(1.78\sqrt{\frac{G_{\mathrm{Ic}}}{\mu t A_{22}^{o}}}, Y_{\mathrm{T}}^{\mathrm{UD}}\right) \quad \text{(E-6)}$$

The in-situ in-plane shear strength is the maximum between the in-plane shear strength of a UD ply and a thin outer ply, i.e.,

$$S_{\mathrm{L}}^{\mathrm{is}} = \max\left(S_{\mathrm{L}}^{\mathrm{UD}}, K_1\gamma_{12}^{\mathrm{is}} + K_2\right) \quad \text{(E-7)}$$

The in-situ transverse compressive strength $Y_{\mathrm{C}}^{\mathrm{is}}$ is given, same as for inner plies, by

$$Y_{\mathrm{C}}^{\mathrm{is}} = \frac{S_{\mathrm{L}}^{\mathrm{is}} Y_{\mathrm{C}}^{\mathrm{UD}}}{S_{\mathrm{L}}^{\mathrm{UD}}} \quad \text{(E-8)}$$

APPENDIX F

3D invariant-based failure criteria for fiber reinforced composites [3-7]

Matrix failure

$$I_1 = \frac{1}{4}\sigma_{\mathrm{yy}}{}^2 - \frac{1}{2}\sigma_{\mathrm{yy}}\sigma_{\mathrm{zz}} + \frac{1}{4}\sigma_{\mathrm{zz}}{}^2 + \tau_{\mathrm{yz}}{}^2 \quad \text{(F-1)}$$

$$I_2 = \tau_{\mathrm{xy}}{}^2 + \tau_{\mathrm{xz}}{}^2 \quad \text{(F-2)}$$

$$I_3 = \sigma_{\mathrm{yy}} + \sigma_{\mathrm{zz}} \quad \text{(F-3)}$$

Model parameters α_1, α_2

$$\alpha_1 = \frac{1}{S_{\mathrm{T}}{}^2} \quad \text{(F-4)}$$

$$\alpha_2 = \frac{1}{S_{\mathrm{L}}{}^2} \quad \text{(F-5)}$$

Matrix failure in tension ($I_3 > 0$)

$$\alpha_{32}^{\mathrm{t}} = \frac{1 - \frac{Y_{\mathrm{T}}}{2Y_{\mathrm{BT}}} - \alpha_1\frac{Y_{\mathrm{T}}{}^2}{4}}{Y_{\mathrm{T}}{}^2 - 2Y_{\mathrm{BT}}Y_{\mathrm{T}}} \quad \text{(F-6)}$$

$$\alpha_3^{\mathrm{t}} = \frac{1}{2Y_{\mathrm{BT}}} - 2\alpha_{32}^{\mathrm{t}}\mathrm{Y}_{\mathrm{BT}} \quad \text{(F-7)}$$

$$f_{\mathrm{mt}} = \alpha_1 I_1 + \alpha_2 I_2 + \alpha_3^{\mathrm{t}} I_3 + \alpha_{32}^{\mathrm{t}} I_3{}^2 \quad \text{(F-8)}$$

Matrix failure in compression ($I_3 \leq 0$)

$$\alpha_{32}^{\mathrm{c}} = \frac{1 - \frac{Y_{\mathrm{C}}}{2Y_{\mathrm{BC}}} - \alpha_1\frac{Y_{\mathrm{C}}{}^2}{4}}{Y_{\mathrm{C}}{}^2 - 2Y_{\mathrm{BC}}Y_{\mathrm{C}}} \quad \text{(F-9)}$$

$$\alpha_3^{\mathrm{c}} = \frac{1}{2Y_{\mathrm{BC}}} - 2\alpha_{32}^{\mathrm{c}}Y_{\mathrm{BC}} \quad \text{(F-10)}$$

$$f_{\mathrm{mc}} = \alpha_1 I_1 + \alpha_2 I_2 + \alpha_3^{\mathrm{c}} I_3 + \alpha_{32}^{\mathrm{c}} I_3{}^2 \quad \text{(F-11)}$$

Fiber failure in tension, if $\sigma_{xx} \geq 0$:

$$f_{ft} = \frac{\varepsilon_{xx}}{\varepsilon_1^T} \quad \text{(F-12)}$$

Fiber failure in compression, if $\sigma_{xx} < 0$:

Angle of the kinking plane (ψ)

If $\tau_{xy} = \tau_{xz} = 0$

$$\psi = \frac{1}{2}\tan^{-1}\left(\frac{2\tau_{yz}}{\sigma_{yy}-\sigma_{zz}}\right) \quad \text{(F-13)}$$

Else:

$$\psi = \frac{\tau_{xz}}{\tau_{xy}} \quad \text{(F-14)}$$

Misalignment angle at failure when a pure longitudinal compression is applied (φ_c)

$$\varphi_c = \frac{1}{2}\tan^{-1}\left\{\frac{4\sqrt{\alpha_1-4\alpha_2+\alpha_2{}^2 X_c{}^2+(\alpha_3^c)^2+2\alpha_2\alpha_3^c X_c+4\alpha_{32}^c}+(\alpha_1+4\alpha_{32}^c)X_c+4\alpha_3^c}{(\alpha_1-4\alpha_2+4\alpha_{32}^c)X_c{}^2}\right\} \quad \text{(F-15)}$$

Initial misalignment angle (φ_0)

Linear shear and small angles

$$\varphi_0 = \varphi_c\left(1+\frac{|X_c|}{G_{12}}\right)^{-1} \quad \text{(F16)}$$

Non-linear shear

$$F(\varphi_0) = \varphi_c - \varphi_0 - \left|\frac{X_c \sin 2\varphi_0}{2G_{12}} + \beta\frac{X_c{}^3 \sin^3 2\varphi_0}{8}\right| \quad \text{(F-17)}$$

$$\frac{dF}{d\varphi_0} = -1 - \left|\frac{X_c \cos 2\varphi_0}{G_{12}} + \beta\frac{3}{4}X_c{}^3 \sin^2 2\varphi_0 \cos 2\varphi_0\right| \quad \text{(F-18)}$$

Solving recursive funtion

$$\varphi_0{}^{i+1} = \varphi_0{}^{i} - \frac{F(\varphi_0{}^{i})}{\frac{\mathrm{d}F}{\mathrm{d}\varphi_0}\Big|_{\varphi_0=\varphi_0{}^{i}}} \quad \text{(F-19)}$$

Shear stress in the misalignment frame $\sigma_{12}^{(\mathrm{R})}(\varphi_0, \psi)$

$$\sigma_{12}^{(\mathrm{R})}(\varphi_0, \psi) = \frac{1}{2}\left[-\sigma_{\mathrm{xx}} + \sigma_{\mathrm{yy}}\cos^2\psi + \sigma_{\mathrm{zz}}\sin^2\psi + \tau_{\mathrm{yz}}\sin 2\psi\right]\sin 2\varphi_0 + \\ + \frac{1}{2}\left(\tau_{\mathrm{xy}}\cos\psi + \tau_{\mathrm{xz}}\sin\psi\right)\cos 2\varphi_0 \quad \text{(F-20)}$$

Kinking angle (φ)

$$\varphi = \mathrm{sgn}\left\{\sigma_{12}^{(\mathrm{R})}(\varphi_0, \psi)\right\}\left\{\varphi_0 + \left|\frac{\sigma_{12}^{(\mathrm{R})}(\varphi_0,\psi)}{G_{12}} + \beta\left[\sigma_{12}^{(\mathrm{R})}(\varphi_0, \psi)\right]^3\right|\right\} \quad \text{(F-21)}$$

Preferred direction (a)

$$a = \begin{bmatrix} \cos\varphi \\ \cos\psi\sin\varphi \\ \sin\psi\sin\varphi \end{bmatrix} \quad \text{(F-22)}$$

Structural tensor (A)

$$A = a \otimes a \quad \text{(F-23)}$$

Reaction stress tensor (σ^r)

$$\sigma^r = \frac{1}{2}(tr\sigma - a\sigma a)1 - \frac{1}{2}(tr\sigma - 3a\sigma a)\mathrm{A} \quad \text{(F-24)}$$

Plasticity inducing stress tensor (σ^p)

$$\sigma^p = \sigma - \sigma^r \quad \text{(F-25)}$$

Invariants

$$I_1 = \frac{1}{2}tr(\sigma^p)^2 - a(\sigma^p)^2 a \quad \text{(F-26)}$$

$$I_2 = a(\sigma^p)^2 a \quad \text{(F-27)}$$

$$I_3 = tr\sigma - a\sigma a \quad \text{(F-28)}$$

Fiber failure in compression, if $I_3 > 0$ (Matrix in tension):

$$f_{\mathrm{fc}} = \alpha_1 I_1 + \alpha_2 I_2 + \alpha_3^{\mathrm{t}} I_3 + \alpha_{32}^{\mathrm{t}} {I_3}^2 \quad \text{(F-29)}$$

Fiber failure in compression, if $I_3 \leq 0$ (Matrix in compression):

$$f_{fc} = \alpha_1 I_1 + \alpha_2 I_2 + \alpha_3^c I_3 + \alpha_{32}^c {I_3}^2 \quad \text{(F-30)}$$

APPENDIX G

Experimental material characterization tests to determine Y_T, in addition to the provided TDS of *Hexply® F6376C-HTS (12K)-5-35%*, *HEXCEL / AIRBUS* [3-6], in **Chapter 3**:

specimen	L_0 [mm]	ΔL at F_{max} [mm]	F_{max} [mm]	Y_T [MPa]
spec-1	125.15	2.10	4971.10	97.37
spec-2	125.16	2.47	5486.80	110.56
spec-3	125.20	2.78	6279.10	117.59
spec-4	125.19	2.58	5678.50	107.27
spec-5	125.19	2.22	5072.20	94.72
spec-6	125.20	2.35	5313.70	100.38
spec-7	125.22	2.33	5341.60	100.91
spec-8	125.23	2.22	5135.50	97.48
spec-9	125.23	2.33	5397.50	102.16
spec-10	125.17	2.49	5438.30	112.03
Mean	**125.19**	**2.39**	**5411.43**	**104.05**
Standard deviation	0.03	0.19	350.76	7.08

Table A-1: Experimental results of transverse tensile test, ASTM-D3039-14 [4-4]

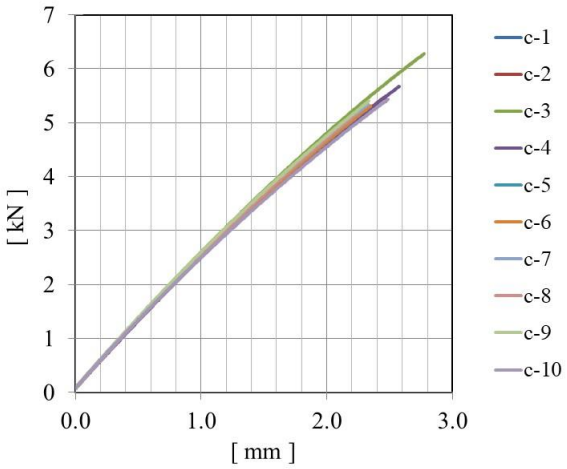

Figure A-1: Corresponding load-displacement curves for transverse tensile test

Experimental material characterization tests to determine X_T, X_C, Y_T, E_{11}^T, $E_{22}^T = E_{33}^T$, in addition to the provided TDS of *NTPT Thinpreg™ 135* with *HS40/T800* at 67g/m^2 [4-7], in **Chapter 4**:

specimen	L_0 [mm]	ΔL at F_{max} [mm]	E_{11}^T [GPa]	X_T [MPa]
spec-1	140.02	3.79	95.21	2312.01
spec-2	135.04	3.81	86.12	2153.98
spec-3	135.05	3.62	85.63	2033.81
spec-4	135.05	4.10	85.24	2234.19
spec-5	135.05	3.92	80.44	2086.98
spec-6	135.06	3.91	85.23	2178.37
spec-7	135.03	3.92	84.23	2182.53
spec-8	135.04	4.19	82.98	2259.53
Mean	**135.67**	**3.91**	**85.63**	**2180.18**
Standard deviation	1.64	0.17	4.00	84.70

Table A-2: In-plane longitudinal tensile modulus and strength, ASTM-D3039-14 [4-4]

specimen	L_0 [mm]	ΔL at F_{max} [mm]	E_{22}^T [GPa]	Y_T [MPa]
spec-1	125.24	1.26	8.94	87.00
spec-2	125.08	1.28	9.03	88.39
spec-3	125.11	1.10	8.99	76.96
spec-4	125.11	1.03	8.96	72.88
spec-5	125.09	0.93	9.10	67.30
spec-6	125.08	1.32	9.36	93.99
Mean	**125.12**	**1.15**	**9.06**	**81.09**
Standard deviation	0.05	0.12	0.12	8.13

Table A-3: Transverse tensile modulus and strength, ASTM-D3039-14 [4-4]

specimen	L_0 [mm]	ΔL at F_{max} [mm]	X_C [MPa]
spec-1	140.00	0.83	743.55
spec-2	140.00	0.91	984.83
spec-3	140.00	0.82	1138.20
spec-4	140.00	0.79	951.82
spec-5	140.00	1.10	1284.71
spec-6	140.00	0.82	1179.06
spec-7	140.00	1.22	1148.07

spec-8	140.00	1.21	1253.85
Mean	**140.00**	**0.96**	**1085.51**
Standard deviation	0.00	0.17	168.97

Table A-4: In-plane longitudinal compressive strength, ASTM-D6641-14 [4-6]

APPENDIX H

Sensitivity analysis on variation of β-value in **section 3.6.3**. Relative difference of load in [%] for β = 1.45 ±15%.

	β =1.23	β =1.45	β =1.67
QI-45	5.55	5.13	4.58
QI-90	6.24	5.53	4.86
QI-0	4.90	4.79	4.56
stiff-45	6.82	6.02	5.32

Table A-5: Damage initiation load inside the adhesive, with Drucker-Prager criterion, values in [kN]

	β =1.23	β =1.45	β =1.67
QI-45	8.1	0.0	-10.8
QI-90	12.8	0.0	-12.1
QI-0	2.3	0.0	-4.9
stiff-45	13.2	0.0	-11.6
Average	**9.1**	**0.0**	**-9.9**

Table A-6: Relative difference of load in [%] for β = 1.45 ±15%

LIST OF PUBLICATIONS

Conference papers and published abstracts

J. Kupski, S. Teixeira de Freitas, D. Zarouchas, R. Benedictus: *Layup Effect on the Performance of Adhesively Bonded Composite Joints*. Proceedings of AB2017, Porto, 2017

J. Kupski, S. Teixeira de Freitas, D. Zarouchas, R. Benedictus: *Composite layup effect on the failure mechanism of single lap bonded joints*. Proceedings of SAMPE BeNeLux Chapter, Spier, 2018

J. Kupski, S. Teixeira de Freitas, D. Zarouchas, R. Benedictus: *On the influence of overlap topology on tensile strength of composite bonded joints: A multi-stacking design*. Proceedings of ECCM18, Athens, 2018

J. Kupski, S. Teixeira de Freitas, D. Zarouchas, R. Benedictus: *Thin-ply composites on adhesively bonded joints*. Proceedings of AB2019, Porto, 2019

Journal papers

J. Kupski, S. Teixeira de Freitas, D. Zarouchas, P. Camanho, R. Benedictus: *Composite layup effect on the failure mechanism of single lap bonded joints.* Journal of Composite Structures, vol. 217, pp. 14-26, 2019

J. Kupski, D. Zarouchas, S. Teixeira de Freitas: *Thin-plies in adhesively bonded carbon fiber reinforced polymers*. Composites Part B, vol. 181, 2020

J. Kupski, D. Zarouchas, S. Teixeira de Freitas, R. Benedictus: *On the influence of overlap topology on the tensile strength of composite bonded joints: Single overlap versus overlap stacking*. Int. Journal of Adhesion and Adhesives, vol. 103, 2020

X. Li, J. Kupski, S. Teixeira de Freitas, R. Benedictus, D. Zarouchas: *Unfolding the Early Fatigue Damage for CFRP Cross-Ply Laminates.* Int. Journal of Fatigue, vol. 140, 2020

E. Tsiangou, J. Kupski, S. Teixeira de Freitas, I. Villegas: *Welded joints: On the sensitivity of ultrasonic welding of epoxy- and polyetheretherketone (PEEK)-based composites to the duration of the vibration phase.* Composite Part A [under review]

S. Teixeira de Freitas, J. Kupski: *Design of adhesively bonded joints with laminated CFRP adherends: Review, challenges and new opportunities for aerospace structures*. Journal of Composite Structures [under review]

ACKNOWLEDGEMENTS

I would like to express my sincere gratitude to everyone who supported me through the last couple of years in Delft. Starting off with Rinze Benedictus, the promoter of my PhD project, and Gemma van der Windt, the department's secretary, who let me go my way with no restrictions at all. I am deeply grateful for having my supervisors Sofia Teixeira de Freitas, who never seems to get tired of revising any version of my texts, and Dimitrios Zarouchas who brought to me a different image of a modern scientist, working on world class fundamental research, with the mind-set of a teenager. Sincere thanks also go to the technicians of D-ASML, namely Berthil Grashof, Misja Huizinga, Kees Paalvast, Ed Roessen, Victor Horbowic and Fred Bosch, for very professional and yet fun times in the lab. A special thanks goes to Gertjan Mulder for any kind of emergency help at literally any time.

Next, I am much obliged to my brave office mates Megan, Xi, Agnes, Aydin and Bram who had to endure tons of smelly sports cloth around my desk, overfilled waste bins and regular non-PhD-related guests in the evenings. My dear colleagues and Delftian friends Timo, Romina, Nicos, Chirag, Jesse, Eirini and Nicolas: Although we were all different in our research, background and daily life, it felt like a little family for me.

A huge thank to Dick, Roos and Shamangi, my fitness trainers from TU Delft-X, for about 330,000 reps of launches, dead lifts and push ups. From day one, I participated in your classes. The sport played an important role for my personal balance and for staying healthy and sharp. I also thank Lander, Julius, Max and Aydin, my after-hour partners in crime, as well as the rest of the AerGo-team, for lots of fun, and for constantly challenging me in how to motivate, manage and lead.

I thank my parents for supporting me along the way, especially my father for the patience of listening to several dozen hours of high-speed, dead-boring monologues. Finally, a big hug to Tutu, the strongest team player I have ever met, for supporting and listening to me, no matter what.

CURRICULUM VITAE

Julian Alexander Kupski, born 8th November 1985 in Werther, Germany

08/1996 – 06/2005	Ratsgymnasium Bielefeld Grammar School
06/2005 – 03/2006	Military service Armored infantryman
10/2006 – 12/2011	RWTH Aachen University, Diplom-Ingenieur Mechanical Engineering, Diploma Concept and implementation of a robotic end-effector for handling textile semi-finished products along the automated preforming process
09/2010 – 02/2011	ETH Zuerich, ERASMUS-programme Mechanical Engineering, specializing in Advanced Structures and Aerospace Engineering
02/2012 – 01/2016	CTC GmbH Stade / Airbus Operations GmbH R&D Engineer and Project Manager Manufacturing prototypes and demonstrators in the field of NCF-preforming, infusion, CFRP tooling and foam sandwich technologies.
02/2016 – 02/2020	Delft University of Technology, Faculty of Aerospace Engineering, PhD researcher on Structural Integrity & Composites: Laminate design of composite bonded joints
10/2017 – 12/2017	Faculdade de Engenharia da Universidade do Porto Visiting researcher on FEA and 3D-invariant based failure analysis of UD-laminae with ABAQUS/FORTRAN user-subroutines
3/2020 – 10/2020	Co-founder of LUMAN Aerospace Developing a solar-electric high-altitude drone, to replace satellites for communication and surveillance missions
Since 11/2020	Application development engineer at V-Carbon GmbH Solvolysis of CFRP waste for re-use in UD-prepreg for primary structural components